

---

THE MESOSCALE ORGANIZATION OF HUMAN  
CONNECTOME SHAPES IGNITION IN CORTICAL  
ACTIVITY

---

Tesis entregada a

**LA UNIVERSIDAD DE VALPARAÍSO**

En Cumplimiento Parcial de los requisitos para optar al grado de

**Doctor en Ciencias con mención en Neurociencia**

**Facultad de Ciencias**

**Por**

**Samy Nicolás Castro Novoa**

**24 Abril, 2020**

**Dirigida por: Dr. Patricio Rodrigo Orio Alvarez**

**Co-Dirigida por: Dr. Wael El-Deredy**

**FACULTAD DE CIENCIAS**

**UNIVERSIDAD DE VALPARAÍSO**



---

INFORME DE APROBACION  
TESIS DE DOCTORADO

---

**Se informa a la Facultad de Ciencias que la Tesis de Doctorado presentada por:**

**SAMY NICOLÁS CASTRO NOVOA**

**Ha sido aprobada por la comisión de Evaluación de la tesis como requisito para optar al grado de Doctor en Ciencias con mención en Neurociencia, en el examen de Defensa de Tesis rendido el día 24 del mes Abril de 2020.**

**Director de Tesis:**

Dr. Patricio Orio

-----

**Co-Director de Tesis:**

Dr. Wael El-Deredy

-----

**Comisión de Evaluación:**

Dr. Adrián Palacios

-----

Dr. Pierre Guiraud

-----

Dr. Diego Cosmelli

-----



*“Cuando un espacio se divide en dos, nace un universo: se define una unidad. La descripción, la investigación y la manipulación de unidades están en la base de toda indagación científica”*

*H. Maturana y F. Varela, Abril 1973*

*“A mi familia, amigos y amores que siempre estuvieron ahí.  
En mi cabeza”*



El trabajo de tesis llevó a la publicación de los siguientes trabajos:

- Cortical Ignition dynamics is tightly linked to the core organisation of the human connectome. **Samy Castro**, Wael El-Deredy, Demian Battaglia, and Patricio Orio. *PLoS Computational Biology*, July 31, 2020, **16**(7): e1007686, DOI: 10.1371/journal.pcbi.1007686.
- Commentary: Amplification and Suppression of Distinct Brainwide Activity Patterns by Catecholamines. Vicente Medel, Joaquín Valdés, **Samy Castro**, Tomás Ossandón, and Gonzalo Boncompte. *Frontiers in Behavioral Neuroscience*, September 18, 2019, **13**: 127, DOI: 10.3389/fnbeh.2019.00217.
- Chaos versus noise as drivers of multistability in neural networks. Patricio Orio, Marilyn Gatica, Rubén Herzog, Jean Paul Maidana, **Samy Castro**, and Kesheng Xu. *Chaos: an interdisciplinary journal of nonlinear science*, October 28, 2018, **28**(10): 106321, DOI: 10.1063/1.5043447.
- Synchronization transition in neuronal networks composed of chaotic or non-chaotic oscillators. Kesheng Xu, Jean Paul Maidana, **Samy Castro** and Patricio Orio. *Scientific Reports*, May 30, 2018, **8**, 8370, DOI: 10.1038/s41598-018-26730-9.



---

## ACKNOWLEDGEMENTS

---

Por el respaldo entregado para la realización de esta tesis, se agradece a:

- A CONICYT por beca doctorado nacional, gastos operacionales y extensión de beca (folio 21140603).
- Doctorado en ciencias con mención en neurociencia de la Universidad de Valparaíso (DNUV) por viajes a congresos y extensión de financiamiento para finalización de la tesis (Octubre 2018 - Marzo 2019).
- Al centro avanzado de ingeniería eléctrica y electrónica (AC3E) por financiamiento viaje Alemania-Inglaterra (2015) y extensión financiamiento para finalización de la tesis (Octubre 2018 - Marzo 2019).
- Al centro interdisciplinario de neurociencias de Valparaíso (CINV) por extensión de financiamiento para finalización de la tesis (Abril 2019 - Agosto 2019).
- Al NLHPC por los recursos computacionales facilitados del super computador LEFTRARU.
- A LASCON (2016), LACONEU (2017, 2019) , Dr. Demian Battaglia (por datos y modelo utilizado en la tesis) y Dr. Nelson Trujillo-Barreto (Discusión proyecto de tesis).

---

## INDEX

---

1. <b>Resumen</b>	-----	xv
2. <b>Abstract</b>	-----	xix
3. <b>Introduction</b>	-----	1
3.1. Spontaneous fluctuation and ignition in cortical activity	-----	1
3.1.1. Fluctuations in cortical activity: Ignition	-----	2
3.1.2. Global neuronal workspace theory	-----	5
3.1.3. Hierarchical information processing	-----	6
3.2. The structural organization of the human connectome	-----	7
3.2.1. The connectome: a neural map of the human cortex	-----	8
3.2.2. Network analysis of the structural organization	-----	10
3.3. Ignition in the whole-brain model of cortical activity	-----	12
4. <b>Hypothesis</b>	-----	17
5. <b>Goals</b>	-----	19
6. <b>Materials and methods</b>	-----	21
6.1. Cortical connectome dataset	-----	21
6.1.1. Cortico-cortical connections of the human connectome	-----	25
6.1.2. Structural connectivity matrix	-----	26
6.2. Network analysis	-----	27
6.2.1. Local organization	-----	27
6.2.2. Mesoscale organization	-----	28

6.2.3.	Global organization	-----	29
6.2.4.	Network toolbox	-----	31
6.3.	Structural surrogate models	-----	32
6.3.1.	Unweighted surrogate connectome (uSCs) models	-----	32
6.3.2.	Weighted surrogate connectome (wSCs) models	-----	34
6.4.	The whole-brain mean-field model of cortical activity	-----	35
6.4.1.	Mean-field model (MFM) of cortical activity	-----	35
6.4.2.	Computer simulations and fixed-point analysis	-----	37
6.4.3.	Ignition in the whole-brain model: Bifurcation points and bistable range		37
6.5.	Node ignition analysis	-----	39
6.5.1.	Thresholding of node activity	-----	39
6.5.2.	Relationship between ignition and network organization	-----	39
6.6.	The pruning of connectome's connections based on the network organization		40
7.	<b>Results chapter 1 - Optimizing the detection of cortical ignition in the whole-brain mean-field model</b>	-----	43
7.1.	The ignition in the cortical activity of the isolated MFM: Phase portrait and steady-state		43
7.2.	The ignition in the cortical activity of the whole-brain MFM: Human connectome adds diversity in the steady-state and generates network ignition	-----	45
7.2.1.	Detection of the network steady-state is optimized by the time of simulation and time step	-----	47
7.2.2.	Detection of the network steady-state is optimized by the initial conditions and is spanned by the coupling gain of the MFM	-----	49
8.	<b>Results chapter 2 - The specific core-shell organization of human connectome supports ignition in cortical activity</b>	-----	55

8.1. Cortical ignition and the network organization in the human connectome	---	55
8.1.1. Human connectome: modeling of ignition and network analysis	---	55
8.1.2. Ignition in cortical activity is structurally organized	-----	59
8.2. Ignition in cortical activity is tightly linked to the weighted core-shell organization in the human connectome	-----	64
8.2.1. The ignition is triggered in the weighted core of the human connectome		64
8.2.2. The ignition recruitment is organized by the weighted core of the human connectome	-----	74
8.3. Ignition in neural activity of other organisms is related to the weighted core organization	-----	83
8.3.1. Organism's connectomes: modeling of ignition and network analysis		84
8.3.2. The ignition is triggered in the weighted core in other organisms	----	86
8.3.3. The ignition recruitment is related to the structural organization in other organisms	-----	87
<b>9. Results chapter 3 - Brain network under attack: pruning of the core connections of the human connectome disrupts the bistability range of ignition in cortical activity</b>	-----	97
9.1. Pruning of the densely connected nodes	-----	99
9.2. Random pruning	-----	100
9.3. Pruning of the sparsely connected nodes	-----	101
<b>10. Discussion</b>	-----	105
<b>11. Appendix</b>	-----	123
11.1. Controls for the human dataset of Hagmann	-----	123
11.2. The script of the dynamic simulation of the mean-field model	-----	133
<b>12. Bibliography</b>	-----	137



---

## TABLE LIST

---

- Table 1.** Abbreviations of cortical regions from parcellation Desikan-Killiany atlas.
- Table 2.** The parameters of the mean-field model implemented by Hansen et al., 2015, based on Deco et al., 2013.
- Table 3.** The time simulation parameters to reach the steady-state in MFM used in the work of Deco (2013) and Hansen (2015).
- Table 4.** The identity of the ignited cortical regions at bifurcation G..
- Table 5.** The dynamic and structural data of the human and surrogate ensembles.
- Table 6.** The explained variance of the Spearman rank correlation between ignition and structural measures for *Human* and uSCs.
- Table 7.** The explained variance of the Spearman rank correlation between ignition and structural measures for *Human* and wSCs.
- Table 8.** The dynamic and structural data of the other organisms connectomes.
- Table 9.** The core and the ignited nodes at the G. in the other organisms.
- Table 10.** The explained variance of the Spearman rank correlation between ignition and structural measures for other organisms connectomes.
- Table 11.** The explained variance of the Spearman rank correlation between ignition and structural measures for Human connectomes.

---

## FIGURE LIST

---

### Materials and Methods

- Figure 1.** The human connectome datasets.
- Figure 2.** The structural connectomes of other organisms.
- Figure 3.** The scheme of unweighted and weighted structural connectivity.
- Figure 4.** Diagram of the k-core *decomposition* algorithm.
- Figure 5.** The Human<sub>hw</sub> connectome.
- Figure 6.** The DPR<sub>hw</sub> connectome.
- Figure 7.** The SW<sub>hw</sub> connectome.
- Figure 8.** The weighted surrogate connectomes conserve the weight distribution of the Human.

### Results chapter 1 - Optimizing the detection of cortical ignition in the whole-brain mean-field model

- Figure 9.** Phase portrait and time-series of an isolated cortical region using the mean-field model.
- Figure 10.** The human connectome and its collective dynamics.
- Figure 11.** Optimizing the time of simulations.
- Figure 12.** Optimizing time step for simulations.
- Figure 13.** Previous works had shown a range of ignition through the coupling gain of the whole-brain model.
- Figure 14.** The ignition in the whole-brain model was optimized in two ranges of initial conditions across the coupling gain parameter.

### Results chapter 2 - The specific core-shell organization of human connectome supports ignition in cortical activity

- Figure 15.** The ignition in the whole-brain mean-field model of cortical activity wired by the human connectome.
- Figure 16.** Network analysis of different levels of the structural organization.
- Figure 17.** The cortical regions ignite through the coupling gain and its structural organization.
- Figure 18.** Ignition in cortical activity is influenced by the core-shell organization of the human connectome.
- Figure 19.** Ignition scheme for core-shell organization of the human connectome.
- Figure 20.** The human cortical connectome requires a lower coupling gain to display ignition than unweighted surrogate models.
- Figure 21.** The ignited nodes and the unweighted network analysis.

- Figure 22.** The ignited cortical regions are loosely related to the unweighted core or degree of the human connectome at the ignition point  $G$ .
- Figure 23.** The ignition in the human connectome was not related to the unweighted core-shell organization or degree.
- Figure 24.** The human cortical connectome requires a lower coupling gain to display ignition than weighted surrogate models.
- Figure 25.** The ignited nodes and the weighted network analysis.
- Figure 26.** Ignited cortical regions match perfectly the weighted core of the human connectome at the ignition point  $G$ .
- Figure 27.** The ignition in the human connectome is related to the weight of inputs more than outputs of the local organization.
- Figure 28.** The ignition in the human connectome is tightly related to the core-shell organization.
- Figure 29.** The bistability range of ignition is preserved in related organisms.
- Figure 30.** The ignition,  $s_{max}$  and strength levels for each node in the fruit fly (*Drosophila melanogaster*) dataset.
- Figure 31.** The ignition,  $s_{max}$  and strength levels for each node in the mouse (*Mus musculus*) dataset.
- Figure 32.** The ignition,  $s_{max}$  and strength levels for each node in the rat (*Rattus norvegicus*) dataset.
- Figure 33.** The ignition,  $s_{max}$  and strength levels for each node in the macaque (*Macaca mulatta*) dataset.

Results chapter 3 - Brain network under attack: pruning of the core connections of the human connectome disrupts the bistability range of ignition in cortical activity

- Figure 34.** The pruning procedure.
- Figure 35.** Effect of selective pruning of the human connectome in the ignition threshold for the bistability range.

## Discussion

- Figure 36.** The intrinsic ignition framework.

## Appendix

- Figure 37.** The ignition,  $s$ -core, and strength levels for each cortical region in the Schirner dataset.
- Figure 38.** The ignition,  $s$ -core, and strength levels for each region in the Wirsich dataset.
- Figure 39.** The ignition,  $s$ -core, and strength levels for each cortical region in the Deco76 dataset.
- Figure 40.** The ignition,  $s$ -core, and strength levels for each region in the Deco90 dataset.
- Figure 41.** The ignition,  $s$ -core, and, strength levels for each region in the Deco116 dataset.
- Figure 42.** The ignition recruitment comparative between  $s$ -core and strength of each node in all the human connectomes.

---

LIST OF SYMBOLS, ABBREVIATIONS AND NAMING

---

<b>FC</b>	Functional connectivity	<b>DKA</b>	Desikan-Killiany atlas
<b>fMRI</b>	Functional magnetic resonance imaging	<b>AAL</b>	Automated anatomical labeling
<b>ECoG</b>	Electrocorticography	<b>DMN</b>	Default mode network
<b>EEG</b>	Electroencephalogram	<b>PCC</b>	Posterior cingulate cortex
<b>MEG</b>	Magnetoencephalogram	<b>mPFC</b>	Medial prefrontal cortex
<b>LFP</b>	Local field potential	<b>AG</b>	Angular gyrus
<b>dIPFC</b>	Dorsolateral prefrontal cortex	<b>SMN</b>	Somatomotor network
<b>MUA</b>	Multi-unit activity	<b>SMA</b>	Supplementary motor area
<b>GNWT</b>	Global neuronal workspace theory	<b>CS</b>	Central sulcus
$N_i$	Number of ignited nodes	<b>VIS</b>	Visual network
$\pm$	Standard deviation	<b>FPN</b>	Frontoparietal network
<b>MRI</b>	Magnetic resonance imaging	<b>IFG</b>	Inferior frontal gyrus
<b>RSN</b>	Resting-state networks	<b>MFM</b>	Mean-field model
<b>DSI</b>	Diffusion spectrum imaging	<b>NMDA</b>	N-Methyl-d-aspartate
$\rho_r$	Explained variance of Spearman rank correlation	<b>SER</b>	Susceptible-excited-refractory model

<b>SC</b>	Structural connectivity	<b>cpl<sub>random*</sub></b>	cpl from a random equivalent network
<b>CoCoMac</b>	Collation of connectivity data for the macaque	<b>cc<sub>i</sub></b>	Clustering coefficient of node $i$
<b>C<sub>i</sub></b>	Structural connectivity matrix	<b>cc</b>	Average cc of the network
<b>A<sub>i</sub></b>	Adjacency matrix	<b>cc<sub>random*</sub></b>	cc from a random equivalent network
<b>w<sub>i</sub></b>	Weighted matrix	$\lambda$	Normalized cpl
<b>k<sub>i</sub></b>	Degree of node $i$	$\gamma$	Normalized cc
<b>s<sub>i</sub></b>	Strength of node $i$	<b>uSCs</b>	Unweighted surrogate connectomes
<b>s<sub>i</sub></b>	In-strength of node $i$	<b>wSCs</b>	Weighted surrogate connectomes
<b>s<sub>i</sub></b>	Out-strength of node $i$	<b>Human<sub>i</sub></b>	Surrogate that preserves the connectivity pattern
<b>k<sub>n</sub></b>	Max degree of a given core	<b>DPR<sub>i</sub></b>	Degree-Preserving Random ensemble
<b>k<sub>n</sub>core</b>	Core with the largest k <sub>n</sub>	<b>SW<sub>i</sub></b>	Small-World network model
<b>s<sub>n</sub></b>	Max strength of a given core	<b>Human<sub>n</sub></b>	Surrogate that preserves the weight distribution
<b>in-s<sub>n</sub></b>	Max in-strength of a given core	<b>DPR<sub>n</sub></b>	Degree and Weight-Preserving Random ensemble
<b>out-s<sub>n</sub></b>	Max out-strength of a given core	<b>SW<sub>n</sub></b>	Small-World network model preserving the weight distribution
<b>s<sub>n</sub>core</b>	Weighted core with the largest s <sub>n</sub>	<b>ICs</b>	Initial conditions of variable $S$
<b>in-s<sub>n</sub>core</b>	Weighted core with the largest in-s <sub>n</sub>	<b>Low ICs</b>	$0 \leq S_i \leq 0.1$
<b>out-s<sub>n</sub>core</b>	Weighted core with the largest out-s <sub>n</sub>	<b>High ICs</b>	$0.3 \leq S_i \leq 1$
<b>N</b>	Nodes	<b>G</b>	Ignition point
<b><math>\sigma</math></b>	Small-world index	<b>G</b>	Flaring point
<b>cpl</b>	Characteristic path length	<b>R<sub>n</sub></b>	Maximum mean firing rate of the network
<b>F<sub>i</sub></b>	The fraction of ignited nodes	<b>G</b>	Coupling gain parameter

---

## LIST OF EQUATIONS

---

- Equation 1.** The connectivity matrix.  
**Equation 2.** The degree of a node.  
**Equation 3.** The strength of a node.  
**Equation 4.** The in-strength and out-strength of a node.  
**Equation 5.** The normalized characteristic path length.  
**Equation 6.** The clustering coefficient a node.  
**Equation 7.** The average clustering coefficient of a network.  
**Equation 8.** The normalized clustering coefficient.  
**Equation 9.** The small-world index.  
**Equation 10.** The mean-field model.



La cognición humana depende en las fluctuaciones de la actividad cortical para realizar tareas o entrar en la percepción consciente. Las fluctuaciones también ocurren espontáneamente, lo que está influido por condicionantes fisiológicas y anatómicas. Un tipo de fluctuación es la ignición, en la cual la actividad cortical realiza rápidas transiciones desde un régimen de baja a uno de alta tasa de disparo. La ignición ha sido estudiada sistemáticamente en conductas relacionadas a tareas tales como la memoria de trabajo o el acceso a la percepción consciente, así como también en el paradigma de estado de reposo. La conectividad estructural subyacente (i.e., el mapa anatómico de conexiones excitatorias de corto y largo alcance) ha sido propuesta como uno de los factores clave para entender en parte las fluctuaciones de la actividad cortical. Sin embargo, aún no se comprende cómo la ignición de la actividad cortical está relacionada a la estructura subyacente. Esta tesis explora cómo la organización estructural del córtex humano es un factor en la “*ignitabilidad*” (i.e. la posibilidad de realizar ignición) de las regiones corticales en el paradigma de estado de reposo. Utilizando un enfoque de simulación de cerebro completo con modelo de campo medio, abordé dos preguntas: ¿la ignición de la actividad cortical está influenciada por la organización estructural del conectoma humano? Más aún, si este es el caso, ¿a qué nivel de la organización de la red (i.e., organización *local* o *mesoescala*; red *sin peso* o *con peso*) ocurre esta relación?

**En el capítulo 1**, muestro cómo en el modelo de campo medio embebido en la conectividad del córtex humano genera ignición a nivel de red. Esto fue estudiado tangencialmente en los trabajos de Deco en 2013 y de Hansen en 2015. Sin embargo, los parámetros que ellos utilizan no se encuentran optimizados para el estudio de la ignición en la red. He extendido su trabajo, optimizando el paso de integración y el tiempo de simulación. Asimismo, he definido un rango específico de las condiciones iniciales para el estudio de la ignición de la red en el modelo de

cerebro completo. El resultado principal del capítulo es la maximización del rango de ignición en el parámetro de acoplamiento de la excitabilidad global  $G$ . Esto se logra con la optimización de las condiciones iniciales en dos rangos específicos.

**En el capítulo 2**, muestro cómo la actividad cortical es influenciada por la estructura, tanto a nivel local como de mesoescala. He validado los resultados obtenidos para el conectoma humano usando modelos subrogados que preservan ya sea su patrón de conectividad, distribución de grado, relación integración/segregación, o su distribución de pesos en las conexiones (i.e. sus pesos sin un orden específico). Todos los modelos subrogados presentan un rango de biestabilidad. Sin embargo, la ignición en el conectoma humano presenta rasgos excepcionales relativos a su organización en núcleo. Primero, éste proporciona un umbral excepcionalmente bajo de excitabilidad global  $G$  para la ignición de la red. El núcleo con conexiones de mayor fuerza contiene al mismo tiempo las regiones en ignición cuando ésta se gatilla en el menor valor del parámetro  $G$ , llamado  $G_c$ , en el conectoma humano. En contraste, los modelos subrogados presentan ignición fuera de dicho núcleo y a valores más altos del parámetro  $G$ . Segundo, la secuencia de ignición de las áreas, asociada al parámetro  $G$ , se explica por la organización en núcleo y capas del conectoma humano. Esta relación no es replicada por los conectomas subrogados, confirmando la excepcionalidad de la relación entre la ignición de la actividad neural del córtex humano y su organización en núcleo y capas. Por lo tanto, la secuencia de ignición está organizada de manera específica en núcleo-periferia dado por los pesos de las conexiones en el conectoma humano.

Finalmente, se estudió la relación entre ignición y organización estructural como un principio arraigado en la evolución, más que una singularidad del conectoma humano. Usando los conectomas disponibles de organismos relativos, macaco (*Macaca mulatta*), rata (*Rattus norvegicus*), ratón (*Mus musculus*), y mosca de la fruta (*Drosophila melanogaster*), el modelo

evidenció que la ignición está explicada por la organización local y mesoescala de los diversos conectomas.

**En el capítulo 3**, utilice un enfoque diferente para confirmar cómo la organización estructural sostiene la ignición de las regiones corticales en estado de reposo. Para aquello, se cortó selectivamente las conexiones del núcleo o de las regiones altamente conectadas. Luego se analizó los cambios en los puntos de ignición  $G$  y colapso  $G_+$  de la ignitabilidad cortical. La selección se basó en el criterio de grado, fuerza, y descomposición de  $k$ -núcleo o  $s$ -núcleo. El corte selectivo del núcleo, como también de las regiones altamente conectadas, aumenta los valores (o umbrales) para los puntos de  $G$  y  $G_+$ . Por lo tanto, la ignitabilidad de cada región cortical y de la red está influenciada por la organización estructural.

En conclusión, esta forma específica de organización en núcleo y capas da cuenta de un principio estructural de la ignición neural. Este da un marco de trabajo para el estudio de la influencia estructural en este tipo de fluctuaciones de la actividad cortical. Más aún, las regiones altamente conectadas y que forman núcleos son fundamentales para dar forma y sostener el estado de ignición en la red del conectoma humano.



Human cognition relies on fluctuations of cortical activity to perform tasks or realize conscious perception. The fluctuations also occur spontaneously, influenced by physiological and anatomical constraints. One type of fluctuation is the “ignition,” in which the cortical activity realizes fast transitions from a low to a high firing rate regime. Ignition has been studied systematically in task-related behaviors such as working memory or conscious perception access, as well as in the resting-state paradigm. The underlying structural connectivity (i.e., the anatomical map of short- and long-range excitatory connections) has been proposed as one of the key factors to understand fluctuations in cortical activity. However, it is not well understood how the ignition in cortical activity is related to the underlying structure. This thesis investigates how the human cortex’s structural organization is a factor in the “*ignitability*” (i.e., the possibility of realizing ignition) of the cortical regions in the resting-state paradigm. Using a whole-brain mean-field model approach, I address two questions: does the human connectome’s structural organization influence ignition in cortical activity? Moreover, if it were the case, at which level of the network organization (i.e., *local* or *mesoscale* organization, or global; *unweighted* or *weighted* network), does this relationship occur?

**Chapter 1** shows how a mean-field model embedded in human cortex connectivity generates ignition at the network level. It was studied tangentially in the works of Deco in 2013 and Hansen in 2015. However, the parameters that they used are not optimized to study the network ignition. I extend their work, optimizing the time step and the time of simulation parameter. Also, I define a specific range of the initial conditions for the study of network ignition in the whole-brain model. The main result of this chapter is the maximization of the ignition range in the parameter of global coupling excitability  $G$ . It is achieved with the optimization of the initial conditions in two specific ranges.

**Chapter 2** shows how cortical activity is influenced by the structure at the local or mesoscale level. I validated the human connectome results using surrogate models that preserve either its connectivity pattern, degree distribution, integration/segregation ratio, or weight distribution of the connections (i.e., its weights without a specific order). All the surrogate models have ignition in a bistable range. However, the ignition in the human connectome has exceptional features related to the core organization. First, it has a low excitability threshold for the network ignition. The core with the strongest connections includes, at the same time, the ignited regions when it is triggered at the lowest value of the coupling gain  $G$ , called  $G_c$ , in the human connectome. In contrast, the surrogate models present ignition outside of the mentioned core and with higher values of the parameter  $G$ . Second, the ignition sequence of the areas associated with the parameter  $G$  is explained by the weighted core-shell organization of the human connectome. This relationship is not replicated by the surrogate connectomes, confirming the exceptionality of the relationship between the ignition of the cortex's neural activity and its organization in core and shells. Therefore, the ignition sequence is organized by a specific weighed core-shell arrangement in the human connectome.

Finally, I study the relationship between ignition and structural organization as a neural principle rooted in evolution, rather than a human connectome uniqueness. Using the available connectomes of related organisms, macaque (*Macaca mulatta*), rat (*Rattus norvegicus*), mouse (*Mus musculus*), and fruit fly (*Drosophila melanogaster*), the model reveals that ignition is explained by the local and mesoscale organization of the different connectomes.

**Chapter 3** uses a different approach to confirm how the structural organization sustains the ignition in cortical regions in the resting state. For that, I pruned selectively the connections of the core or the highly connected nodes. Then, I analyzed the changes in the ignition  $G_c$  and collapse  $G_+$  points of the cortical ignitability. The selection was based on the degree, strength,  $k$ -core, or  $s$ -core criteria. The selective pruning of the core, as well as the highly connected

regions, increases the values (or thresholds) for the  $G_-$  and  $G_+$  points. Therefore, the ignitability of each cortical region and the network is influenced by the structural organization. In conclusion, this specific core-shell organization seems to be a structural principle of neural ignition. It gives a framework to study the structural influence in this type of cortical activity fluctuations. Moreover, the highly connected and core regions are fundamental to shape and sustain the human connectome's network ignition state.



## 1. Spontaneous fluctuations and ignition in cortical activity

Human (*Homo sapiens*) cognition relies on the coordinated recruitment of distributed brain-wide networks, which are flexibly reconfigured depending on external context and internal brain state (Bressler and Menon, 2010). Even at rest, the functional connectivity (FC) between brain regions is restless, switching between a multiplicity of meta-stable configurations (Fox and Raichle, 2007; de Pasquale *et al.*, 2010), which are reminiscent of cognitive networks evoked during specific tasks (Cole *et al.*, 2014; Kieliba *et al.*, 2019). Such dynamic FC has been considered to stem from the complex collective dynamics of brain networks (Deco, Jirsa and McIntosh, 2013). In particular, based on theoretical neuroscience insights (Battaglia *et al.*, 2012; Kirst, Timme and Battaglia, 2016), one expects that a repertoire of multi-stable brain dynamical states, called “dynome” (Kopell *et al.*, 2014), generates the observed repertoire of FC configurations, the “chronnectome” (Calhoun *et al.*, 2014). Then, understanding how the fluctuations in the neural dynamics arise is key to lay the neurobiological foundations for human cognition (Varela *et al.*, 2001; Buzsáki, 2006; Lynall *et al.*, 2010; Sporns, 2016). Technical advances in imaging have provided insights into brain activity and structure *in-vivo* (Cabral *et al.*, 2017; Papegaaij *et al.*, 2017; Battista *et al.*, 2018). The brain activity fluctuates at slow timescale, as observed in resting-state functional magnetic resonance imaging (fMRI) studies (Hutchison *et al.*, 2013; Hansen *et al.*, 2015; Deco *et al.*, 2017). On the other hand, the

fast timescale fluctuations can be measured with electrocorticography (ECoG) (Golan *et al.*, 2016), electroencephalogram (EEG) (Del Cul, Baillet and Dehaene, 2007), and magnetoencephalogram (MEG) (Moutard, Dehaene and Malach, 2015; Baria, Maniscalco and He, 2017). Nevertheless, the factors that give rise to these fluctuations of brain activity remain to be elucidated, and their functional relevance is highly debated (Messé *et al.*, 2014; Moutard, Dehaene and Malach, 2015; Deco and Kringelbach, 2017). Some relevant insights are, for instance, that the fluctuations depend on local cortical features such as time delays (Deco and Jirsa, 2012; Messé *et al.*, 2015), the excitatory and inhibitory balance within a brain region (Freyer *et al.*, 2012; Messé *et al.*, 2015; Joglekar *et al.*, 2018), and the organization of their structural connectivity (SC) (Messé *et al.*, 2014, 2015; Joglekar *et al.*, 2018; Lynn and Bassett, 2019). In this thesis, I will explore how the structural organization of the human cortex is involved in the fluctuations of brain activity.

### 1.1. Fluctuations in cortical activity: Ignition

A cortical region activity switches between a low firing rate activity regime and a second “ignited” state where the firing rate is substantially higher. This is often associated with a functional role in working memory or input integration (Wang, 2002; Wong and Wang, 2006; Messé *et al.*, 2015; Moutard, Dehaene and Malach, 2015; Deco and Kringelbach, 2017; Joglekar *et al.*, 2018; van Vugt *et al.*, 2018). The configurations of ignited cortical regions in time would shape the fluctuations in cortical activity.

Ignition has been described in different spatio-temporal domains. At the single neuron domain, ignition is observed in the up and down states of the membrane potential in recordings of the slow-wave sleep stage (Destexhe, 2007). Operationally, up and down states refer to

neurons that have two preferred subthreshold membrane potentials that depend on the inputs of the neighborhood (Wilson, 2008). At the domain of neural circuits, the ignition has been observed in local field potential (LFP) (Navarro-Lobato and Genzel, 2019) and two-photon calcium imaging (Cossart, Aronov and Yuste, 2003), where transient increases in the neural population activity -ignition- have been linked to domains of cognition as working memory and attention (Cossart, Aronov and Yuste, 2003; Holcman and Tsodyks, 2006). Finally, ignition has also been reported in macroscopic studies of fMRI (Finn *et al.*, 2019), EEG (Moutard, Dehaene and Malach, 2015), and MEG (de Pasquale *et al.*, 2010, 2018), where the signal of a given brain region exceeds a threshold value defined by a distinct reference signal. At this macroscopic domain, ignition is linked to visual conscious perception (Noy *et al.*, 2015; van Vugt *et al.*, 2018) and working memory performance (Wong and Wang, 2006). Moreover, ignition has been described not only in humans but also in macaque (*Macaca mulatta*) (van Vugt *et al.*, 2018) and dogs (*Canis familiaris*) (Aulet *et al.*, 2019). Thus, ignition is a phenomenon that plays a role in cognitive and behavioral functions and has been observed at different spatial, temporal, and evolutive domains of brain activity.

Given the cortical structural connectivity, if a region gets into an ignited state (either by spontaneous fluctuations or afferent inputs), its activity could propagate to directly connected regions, possibly inducing them to ignite as well, building together an ignition network (de Pasquale *et al.*, 2018). The propagation of ignition in a system has been studied in the context of epidemic disease (Kitsak *et al.*, 2010; Rock *et al.*, 2014) as well as in cortical dynamics (Hütt, Kaiser and Hilgetag, 2014; Mišić *et al.*, 2015). There is growing experimental (Moutard, Dehaene and Malach, 2015) and modeling (Holcman and Tsodyks, 2006; Wong and Wang, 2006; Joglekar *et al.*, 2018) evidence stressing how cortical ignition is non-linear, with regions only able to get ignited if the inputs they receive -external, but also, notably, recurrent- rise above a

threshold. Whether this threshold is crossed or not depends on structural factors such as the number of neighboring regions and the strength of incoming connections and also on the activity of the neighboring regions, which are, in turn, influenced by the collective network state (Deco and Kringelbach, 2017). Thus, it is not straightforward to disentangle the relative contributions of the cortical structure and dynamics in determining the ignitability of different regions, either at the early or later stages of the ignition cascade (van Vugt *et al.*, 2018).

In 2015, Moutard and colleagues proposed a mechanism to merge the explanation of task-related and spontaneously induced ignition. In their words, “Considering (...) the ignition dynamics that is apparent during the active mode in response to sensory stimulation or task and the resting-state dynamics that emerges in the absence of any stimulus or task, it thus appears that both can be explained by the same mechanism: reverberatory network dominated by excitatory connections.” (Moutard, Dehaene and Malach, 2015).

For example, from a modeling perspective, Wong and Wang proposed a biophysically plausible model of cortical activity that, once recurrent connections are implemented, captures the ignition’s relevant slow timescale features during a visual task (Wong and Wang, 2006). On the experimental side, van Vugt and colleagues studied the access to visual conscious perception in macaques (van Vugt *et al.*, 2018). They recorded visual cortices involved in sensory processing (V1 and V4), as well as the dorsolateral prefrontal cortex (dlPFC), a region involved in perceptual decisions and integrative functions. They showed that even when sensory cortices are in an ignited state during stimuli presentation, if dlPFC is not, the macaque will not be visually aware. Beyond task-related paradigms, ignition has also been observed in the resting-state of human and non-human subjects (Deco and Kringelbach, 2017). Ignition in resting-state, contrary to task-related, has been observed as slow firing rate modulations of cortical activity on ECoG (He *et al.*, 2008; Nir *et al.*, 2008), EEG (Schurger *et al.*, 2015), and

fMRI (Nir *et al.*, 2006; Barttfeld *et al.*, 2015). Together, this suggests that the recurrent connections are the substrate where the ignition can propagate (either activated by stimuli or spontaneously). At the cognitive domain, the ignition of specific networks could be the substrate of conscious awareness. Moutard and colleagues framed this hypothesis into the explanatory framework called global neuronal workspace theory (GNWT).

## 1.2. Global neuronal workspace theory

The global workspace theory, proposed by Baars in the 88', defines a network for conscious work. In the network, the activity patterns of the central nodes define the broadcasting of task-related signals to the conscious perception. This is called the access to the global workspace (Baars, July 30th, 1993). Peripheral nodes compete and collaborate in a structured fashion to broadcast their activity to central nodes of the global workspace. In principle, the global workspace theory is a psychological framework based on cognitive explanations rather than neurobiological ones. More recently, the global workspace theory has received more biological grounds.

From a biological perspective, the mammalian brain could implement such a global workspace architecture, where peripheral nodes have been related to the sensory cortices and global workspace to more integrative regions (Connor and Shanahan, 2007). Thus, in the GNWT framework proposed by Dehaene, Changeaux, and colleagues, the central idea is "... in this model, sensory stimuli mobilize excitatory neurons with long-range cortico-cortical axons, leading to the genesis of a global activity pattern among workspace neurons (...) The GNWT model predicts that conscious presence is a non-linear function of stimulus salience; i.e., a gradual increase in stimulus visibility should be accompanied by a sudden transition of the neuronal workspace into a corresponding activity pattern" (Dehaene, Sergent and Changeux,

2003; Seth, 2007). Then, the interplay between central and peripheral nodes and how their activities are propagated in the network is key to understand the global activity pattern in the brain.

To investigate this interplay between network nodes, Wallace and colleagues developed network-theoretic modeling of the GNWT framework in which “the ignition of a global workspace corresponds to the formation of a ‘giant component’ (of regions) whereby previously disconnected sub-networks coalesce into a single network encompassing the majority of modules. The emergence of giant components in dynamic networks can be considered as a phase transition” (Wallace, April 14th, 2005; Seth, 2007). Adding those definitions to what Moutard proposed as ignition, i.e., “*reverberatory network dominated by excitatory connections*,” it is possible to understand what the GNWT describes as the “*sudden transition of the neuronal workspace*”: peripheral nodes become transiently ignited, and their activity is integrated into the global workspace, building up this giant component. Together, these results suggest a fundamental role of network ignition on the conscious perception in the GNWT framework (Moutard, Dehaene and Malach, 2015; van Vugt *et al.*, 2018).

### 1.3. Hierarchical information processing

An alternative explanation for the ignition of cortical activity is the hierarchical information processing of the cortical activity. In this framework, each cortical region belongs to a hierarchical module, optimizing the propagation of cortical activity (Deco and Kringelbach, 2017). They argue that brain regions follow a graded non-uniform hierarchy in the intrinsic ignition capabilities. In this sense, high hierarchy regions are ignited in almost all the ignition events, whereas low hierarchy regions seldom display ignition. Using human resting-state and deep sleep fMRI data and a validated methodology, they uncover a hierarchical structure of

cortical ignition, i.e., how much each region participates in the collective ignition and, consequently, in the information propagation on the brain (Deco and Kringelbach, 2017).

GNWT and hierarchical information processing are frameworks that bind the ignition events of cortical activity with resting-state (slow fluctuations) and task-related (fast fluctuations) paradigms. Besides the influence of local dynamics on the fluctuations in cortical activity, the underlying structural connectivity is postulated as a critical factor underlying the ignition (Honey *et al.*, 2007, 2009; Rubinov and Sporns, 2010; Messé *et al.*, 2014; Lynn and Bassett, 2019). The next section will cover the backgrounds of network analysis necessary to characterize the particular human connectome's organization that may be shaping cortical ignition.

## 2. The structural organization of the human connectome

Although anatomical connections are crucial for the fluctuations of cortical activity, how the organization of those connections influences the dynamics are a highly debated topic (Lynn and Bassett, 2019). Network neuroscience tools are typically used to study the organization of the human connectome (Rubinov and Sporns, 2010). In the words of Lynn and Bassett, "Network neuroscience -an approach to understand the brain by recording, analyzing, and modeling the interactions between its component parts- is founded upon the idea that the brain comprises a complex web of distinct neural element" (Lynn and Bassett, 2019). The neural elements range from neurons to large-scale cortical regions, and the complex web is implemented from synapses to long-range tracts.

In this framework, a brain network is composed of nodes (or neural regions) connected by edges. The edges represent connections, being either binary or real-valued. The binary case only captures the connectivity pattern (unweighted network), while the real-valued adds a relative strength to the connections between cortical regions (weighted network). Also, a connection is

directed if the edges between the two regions are present only in one direction but not in the other. Moreover, the edges between the two reciprocally connected regions can be asymmetric if the weight of the connections differs. With these definitions, the brain network can be characterized to unveil its structural organization and, hopefully, its role in cortical activity dynamics.

## 2.1. The connectome: a neural map of the human cortex

The connectome, coined by Sporns, Tononi, and Kotter, describes the map of the structural wiring of the cortex (Sporns, Tononi and Kötter, 2005) and has been used to study how the connectivity pattern is related to the cortical activity (Alstott *et al.*, 2009; Rubinov and Sporns, 2010; Fornito, Zalesky and Bullmore, 2016). The structural connectivity ranges from synapses to neural circuits (Chiang *et al.*, 2011; Shih *et al.*, 2015) and long-range connections of whole-brain anatomy (Hagmann *et al.*, 2008). The first attempts to reconstruct the brain's network were *ex-vivo*, in which the connections between neural regions are revealed by histology and tracers injected to the neural regions (for a detailed review, see Fornito *et al.*, 2016, chapter 2). Recently, the development of magnetic resonance imaging (MRI) has allowed the *in-vivo* reconstruction of the structural connectome. There are many pipelines to reconstruct the neural map from the raw MRI data. These pipelines typically comprise on the one side, the detection and reconstruction of the connections and on the other side, the parcellation of cortical regions based on the standard cortical atlas (Tzourio-Mazoyer *et al.*, 2002; Fischl *et al.*, 2004; Hagmann *et al.*, 2008; Rolls, Joliot and Tzourio-Mazoyer, 2015). The atlas can use the cortical network's structural features as the gyrus and sulcus of the brain, as in the case of the Desikan-Killiany atlas (DKA) (Desikan *et al.*, 2006). They can also use functional data as the atlas based on the resting-state networks (RSN) of the brain (Salehi *et al.*, 2020).

To reconstruct the connections between cortical regions, one of the most used methods is the diffusion spectrum imaging (DSI), which uses the fact that the myelinated tracts constrain the diffusion of the water in the brain (Fischl *et al.*, 2004; Desikan *et al.*, 2006). The parcellation assigns the reconstructed connections to cortical regions, which are defined by a given atlas. One of the main limitations of the DSI analysis is that it lacks a priori information about the direction of the neural tracts (Seguin, Razi and Zalesky, 2019).

As aforementioned, the recurrent connections have been proposed as a key factor in the ignition of cortical activity (Moutard, Dehaene and Malach, 2015; van Vugt *et al.*, 2018; Wong and Wang, 2006; Joglekar *et al.*, 2018). The human connectome defined by Hagmann & colleagues has only recurrent connections because it is not possible to determine the direction of the tracts using DSI analysis (Hagmann *et al.*, 2008). Thus, it has a symmetrical connectivity pattern. For example, in 2018, Joglekar and colleagues used a model-based approach to show how the recurrent connections influence the communication of the ignited activity across the macaque cortex (Joglekar *et al.*, 2018). Moreover, Theodoni and colleagues demonstrated that the recurrent connections are the most abundant type of link in the marmoset monkey, showing that recurrent connections come along evolution (Theodoni *et al.*, 2020).

Further, the human connectome from MRI studies is asymmetric in the weight of the connections. This feature is a consequence of the normalization of the connection weight of two regions by their respective volume in a selected parcellation; the volume of the cortical regions may be highly heterogeneous in some parcellations, as the DKA (Hagmann *et al.*, 2008). One issue with that is, the bigger the volume of a cortical area, the more likely it is to catch a connection in the tractography. For this reason, Hagmann's standard normalization procedure penalizes the regions with higher volumes and benefits those with a small volume. Nevertheless, if this asymmetry in the weighted pattern of the brain network is relevant to the cortical activity is far from being understood (Alstott *et al.*, 2014). Indeed, in a network sense, there is a long

debate about how to normalize the connectivity weights and their effective relevance in cortical activity (Betzal *et al.*, 2019).

## 2.2. Network analysis of the structural organization

Brain network analysis studies the network organization of the brain at different domains. The domains range from local, in which only matters to know how many (or how strong) are the interactions between two regions, to global, in which the system capabilities, as the segregative and integrative capacities, are measured as a whole (Lynn and Bassett, 2019). Between those domains, there is a buoyant field that studies the interactions of the mesoscale domain of the cortical network (Hagmann *et al.*, 2008; Harriger, van den Heuvel and Sporns, 2012; Gollo *et al.*, 2015; Messé *et al.*, 2015; Betzel, Medaglia and Bassett, 2018). Network analysis is used to unveil the SC's organizational principles that collectively shape cortical dynamics (Fornito, Zalesky and Bullmore, 2016).

The connectivity of each node defines its central influence on the local domain of the organization. It could be measured as the number of connections of each node in the unweighted network analysis or the sum of each node's weights in the weighted analysis (de Pasquale *et al.*, 2018). The nodes with the highest number of connections (or the strongest connections) are defined as hubs because they are thought of as the most prominent in the fast neural communication through the cortical web (Lynn and Bassett, 2019). Human recordings of resting-state fMRI evidence the functional role of hub nodes present in the default mode network (DMN). In the DMN, the hub nodes comprise regions such as the posterior cingulate cortex (PCC), medial prefrontal cortex (mPFC), and angular gyrus (AG) (Buckner *et al.*, 2009; Cole, Pathak and Schneider, 2010; Tomasi and Volkow, 2010; Zuo *et al.*, 2012; de Pasquale *et al.*, 2013). Moreover, hubs nodes have also been reported in the somatomotor network (SMN)

(supplementary motor area (SMA) and central sulcus (CS) regions), in the visual network (VIS) and frontoparietal network (FPN) (inferior frontal gyrus (IFG) and insula regions) (Tomasi and Volkow, 2011; Zuo et al., 2012). Then, slow macroscopic fluctuations -such as the activity of the resting state networks- are sustained by structural hubs.

The analysis of global organization considers the network as a whole. For example, it can be analyzed in terms of the segregative and integrative capacities of the system. Segregative capacities allow specialized responses of cortical regions, whereas integrative capacities allow the enaction of fast responses to the environmental challenges. In 1998, Watts and Strogatz proposed a strategy to study the integration/segregation ratio of a network, coining the term small-world (Watts and Strogatz, 1998). Conceptually, the small-worldness of a network is derived from the ratio between the characteristic path length of the network (i.e., the average of the smallest path between two cortical regions of all the system) and the clustering coefficient (i.e., the extent in which cortical regions of the neighborhood are preferentially connected between them) (Humphries and Gurney, 2008). Experimentally, the small world architecture has been found in structural connectivity from MRI data (Hagmann et al., 2008; Vaessen et al., 2010) and tract-tracing methods (Hilgetag and Kaiser, 2004), as well as in FC from MEG (Stam, 2004; Valencia et al., 2008), fMRI (Salvador et al., 2005; Achard et al., 2006) and EEG (Smit et al., 2008) recordings (Bassett and Bullmore, 2017). Then, macroscopic fluctuations -such as the functional connectivity recordings- are sustained by the small-world architecture.

Several studies describe the presence of *cores*, a mesoscale domain of organization, in the network dynamics (for a detailed review, see de Pasquale *et al.*, 2018). The core corresponds to several nodes densely interconnected between them. The density of the interconnection of a core is defined by a threshold on the number of connections (or strength of connections) between those nodes, defining a core-shell organization (Hagmann *et al.*, 2008; Kitsak *et al.*, 2010). This

core-shell organization characterizes layers of nodes that share the same level of interconnectivity between them. Altogether, the core-shell organization represents the gradient of interconnectivity strengths on the network. The network's core arrangement has been observed in the analysis of the structural connectome (Hagmann *et al.*, 2008; Swanson, Hahn and Sporns, 2017; Betzel, Medaglia and Bassett, 2018). However, how the ignition is related to the mesoscale organization is not well understood.

Despite the lack of studies relating to ignition with mesoscale organization, simple modeling examples showed its role on activity propagation on a network. Kitsak and colleagues showed a tight link between the level of propagation and the mesoscale organization layers. In fact, the best spreaders of activity in social-related networks correspond with the core nodes and not with the most highly connected nodes (Kitsak *et al.*, 2010). Moreover, the group of Misisic showed that the core regions facilitate the inter-module propagation of cortical activity (Misisic *et al.*, 2015). Thus, the core-shell organization could be central to understand how the network structure facilitates the ignition in cortical activity, a main player in cognition.

### 3. Ignition in the whole-brain model of cortical activity

Here, I search for the structural organization features that influence the ignition in cortical activity. For this, I correlated the specific structural organization of the human connectome with the ignition in cortical activity. The ignition was implemented using the deterministic whole-brain mean-field model (MFM) for cortical activity. The MFM is a reduction of cortical activity to its slowest temporal components, represented by the NMDA channels. The slow temporal components are frequently associated with resting-state low-frequency features of RSN (Deco *et al.*, 2013; Hansen *et al.*, 2015). The local dynamics of each cortical region in the whole-brain MFM differed only in the integrated currents from the neighboring regions.

Previous studies using the cortex-like dynamics of the MFM wired by the human connectome have shown that several characteristics of the simulated data match with empirical data as high correlation with the FC (~0.47) and resemble the fluctuations of cortical states (Hagmann *et al.*, 2008; Deco *et al.*, 2013; Hansen *et al.*, 2015). Remarkably, several studies about mean-field computational models of the resting state -which were not intended to explore cortical ignition directly- also have consistently reported that the best fit between simulated and empirical FC is found in a critical range of global coupling where switching between ignited and not-ignited network states are possible (Deco *et al.*, 2013; Hansen *et al.*, 2015).

Indeed, Deco *et al.* 2013 showed a range of global coupling gain,  $G$ , in which the deterministic collective dynamics seat in at least two states, bounded by bifurcations at  $G_-$  and  $G_+$ . I used the connectome-based model of the human to explain how its connectivity pattern exerts influence over the collective cortical activity in the bifurcations. Moreover, Hansen *et al.* 2015 showed that the ignited regions showed a strong relationship with the core-shell arrangement over the range of bifurcations. Thus, the goal is to evaluate how the heterogeneous patterns of structural organization of the cortex influence cortical ignition. How structural properties sustain and shape these dynamic attractors in the bifurcations  $G_-$  and  $G_+$  has not been elucidated yet.

The structural asymmetry of the inputs gives rise to different ignition patterns, and its relation to the specific organization of the human connectome is the main topic of this work. Furthermore, the network's domain, either local, mesoscale, or global, best captures these relationships. **In chapter 1**, I optimize the model for network ignition using the human connectome. **In chapter 2**, the ignition is evaluated in terms of network organization. The human cortex organization is compared against surrogate models. It assesses if topological and/or weighted properties of the human connectome -such as connectivity pattern, randomness,

complexity, or weighted backbone- are enough for bistable network dynamics. I found a specific and robust correspondence between the ignition pattern and the human connectome's core-shell organization. Then, the result is extended to the related organisms exploring the evolutionary roots for the ignition's organizing principle. **Chapter 3** briefly probes that ignition depends on the connections of the local and mesoscale domain. This is evaluated by pruning connections of the human connectome, based on their organizational identity given by the previous chapter's network analysis. I suggest that if core regions are pruned, the bifurcation's stability will be lost while pruning non-core regions have a negligible impact on bifurcation stability. Finally, in the **discussion**, I analyze my results under the light of the current and related literature, stressing the relevance of the mesoscale organization on brain dynamics, and more importantly, on the structural determinants of human cognition.





---

## Hypothesis

---

The core-shell organization of the human connectome is the most relevant structural determinant that explains the ignition pattern on a deterministic model of bistable cortical dynamics.



---

## Goals

---

1. To implement deterministic cortical network simulations in which the ignition of the network is optimized to the broadest possible bistable range. The optimization would be realized over time of simulation, time step, and initial conditions.
2. To investigate the relationship between the ignition of a mean-field model and the structural organization of the human connectome, using network analysis and surrogate models of structural features.
3. To study the relationship between the ignition of a mean-field model and the structural organization in connectomes of other organisms, to search principles of the neural activity in the structural organization.
4. To test the effect of selectively pruning connections on the network ignition, based on the network analysis of the mesoscale and local organization. Pruning is done based on unweighted and weighted network features.



## 1. Cortical connectome datasets

I used the structural connectivity SC of the human cortex connectome described in the study of Hagmann et al., 2008, which came from MRI data, and it was processed with DSI. The human SC was parcellated with the DKA (Fischl et al. 2004; Desikan et al. 2006), which contains 66 cortical regions (Table 1). The Hagmann dataset is an average of five right-handed male subjects (mean age =  $29.4 \pm 3.4$ ) (Hagmann et al. 2008), which present 1.148 cortico-cortical connections (network's density  $\sim 27\%$ ) (Figure 1A).

I used another five human connectome datasets. One based on the same DKA called the Schirner dataset, which is an average of 50 subjects, 31 females (mean age =  $41.55 \pm 18.44$ ), with 66 nodes and 4.290 connections (network's density  $\sim 98\%$ , Figure 1B) (Schirner et al. 2015). The other four are based on the AAL atlas (Tzourio-Mazoyer et al. 2002; Rolls et al. 2015). The first is the Whirsich dataset, which is an average of 11 subjects, all male (mean age =  $34 \pm 4$ ), with 96 nodes and 8.866 connections (network's density  $\sim 97\%$ , Figure 1C) (Wirsih et al. 2018). The other three connectomes came from the Deco dataset and were the average over 16 subjects (5 women, mean age =  $24.8 \pm 2.5$ ). The Deco dataset used is divided into 76 cortical regions and 2.076 connections ( $\sim 36\%$  network's density, Figure 1D). Also, this dataset contains the cortical + the subcortical regions with 90 nodes and 3.162 connections ( $\sim 39\%$  network's density Figure

1E). Finally, this dataset also adds the cerebellum regions to sum 116 regions and 4.056 connections (~30% network's density, Figure 1F) (Deco et al. 2018).

Additionally, I describe four additional non-human connectome datasets, which I analyzed using the same methods as human SC. Whereas the human connectome data were reconstructed *in-vivo* from diffusion-weighted images, the procedures used to reconstruct the non-human data were more varied, ranging from retrograde tract-tracing to meta-analysis (Betzel et al. 2018).

**Fruit fly.** I analyzed a network reconstructed from 12.995 projection neurons in the female fruit fly brain (Chiang et al. 2011; Shih et al. 2015). Neurons were aggregated among  $N = 50$  local processing units, which represent network nodes. The resulting network is directed and weighted, with 2.049 connections (network's density ~83%) (Figure 2A).

**Mouse.** I also analyzed a mouse connectome reconstructed from tract-tracing experiments made publicly available by the Allen Brain Institute (Oh et al. 2014). Tracers were tracked from a series of injection sites to ipsi- and contra-lateral brain regions. The mouse brain was parcellated into  $N = 112$  regions (56 per hemisphere) and edge weights defined as the volume-normalized number of connections between regions (Rubinov et al. 2015). The resulted network has 6.542 connections (network's density ~52%). Due to the directed nature of the tract-tracing experiments, the resulting network was asymmetric (Figure 2B).

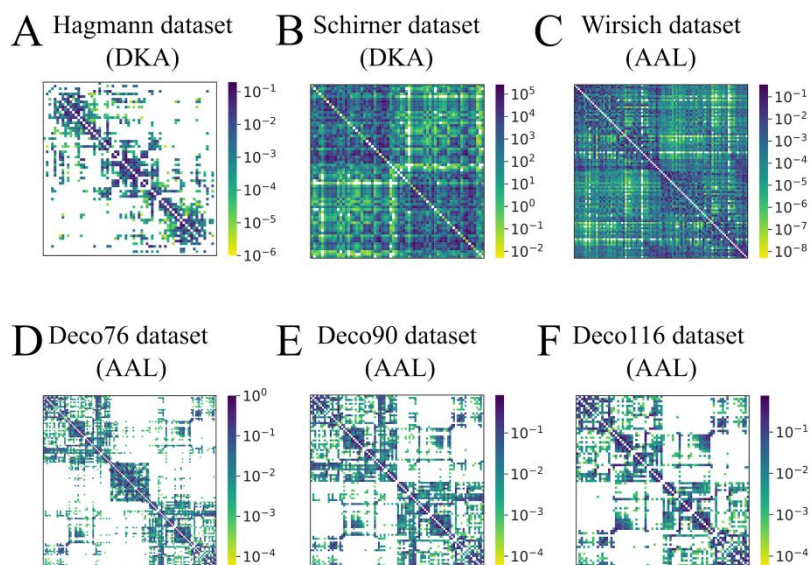


**Figure 1. The human connectome datasets.** The (A) Hagmann and (B) Schirner datasets were parcellated using the DKA. (C) The Wirsich dataset was parcellated using the AAL atlas. (D-F) The Deco dataset was also parcellated with AAL, in which (D) contains only cortical regions (76), (E) contains cortical + subcortical regions (90), and (F) contains cortical + subcortical + cerebellum regions (116). All the connectomes normalize their connections to maintain the same overall strength of the Hagmann’s dataset, 15.3 (see methods for details).

**Rat.** I also analyzed a rat cortical network (Bota et al. 2015). This network was constructed by collating reports on rat tract-tracing experiments (Bota et al. 2005), extracting information from those reports regarding the existence of connections (resulting in >16.000 connections), and based on the consistency and quality of those results, assigning a single weight to an existing inter-regional connection. The result is a directed network of  $N = 156$  cortical regions and 6.805 connections (network’s density  $\sim 28\%$ ) (Figure 2C).

**Macaque.** Finally, I include the macaque cortical connectome, defined by the CoCoMac group (Collation of Connectivity Data for the Macaque) (Bakker et al. 2012), which is a compilation of several tracer studies and includes only the right hemisphere. The CoCoMac contains 212 cortical regions and 4.090 directed and unweighted connections (network’s density  $\sim 9.1\%$ ) (Figure 2D).

**Table 1. Abbreviations of cortical regions from parcellation Desikan-Killiany atlas (Desikan et al., 2006).** The brain order is the same as in Deco & Jirsa 2012. Table extracted from Hansen et al., 2015.

<b>Abbreviation</b>	<b>Cortical Region</b>
ENT	Entorhinal cortex
PARH	Parahippocampal cortex
TP	Temporal pole
FP	Frontal pole
FUS	Fusiform gyrus
TT	Transverse temporal cortex
LOCC	Lateral occipital cortex
SP	Superior parietal cortex
IT	Inferior temporal cortex
IP	Inferior temporal cortex
SMAR	Supramarginal gyrus
BSTS	Bank of the superior temporal sulcus
MT	Middle temporal cortex
ST	Superior temporal cortex
PSTC	Postcentral gyrus
PREC	Precentral gyrus
CMF	Caudal middle frontal cortex
POPE	Pars opercularis
PTRI	Pars triangularis
RMF	Rostral middle frontal cortex
PORB	Pars orbitalis
LOF	Lateral orbitofrontal cortex
CAC	Caudal anterior cingulate cortex
RAC	Rostral anterior cingulate cortex
SF	Superior frontal cortex
MOF	Medial orbitofrontal cortex
LING	Lingual gyrus
PCAL	Pericalcarine cortex
CUN	Cuneus
PARC	Paracentral lobule
ISTC	Isthmus of the cingulate cortex
PCUN	Precuneus
PC	Posterior cingulate cortex

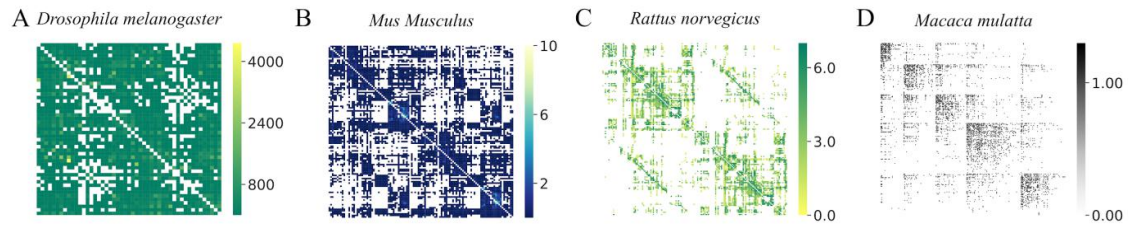


**Figure 2. The structural connectomes of other organisms.** (A) The connectome of fruit fly (*Drosophila melanogaster*), (B) mouse (*Mus musculus*), (C) rat (*Rattus norvegicus*), and (D) macaque (*Macaca mulatta*).

All the connectomes used here, human and non-human ones, are adjusted to preserve the same overall strength of the human dataset of Hagmann et al., 2008 (see below).

### 1.1. Cortico-cortical connections of the human connectome

The *diffusion* MRI was used to reconstruct the connections of the human cortex (Tzourio-Mazoyer et al. 2002; Hagmann et al. 2008; Desikan et al. 2006), and it measures the diffusion anisotropy of water across the brain. The result of the DSI analysis is the *diffusion map*, a 3-dimensional vector matrix that contains the myelinated connections of the brain (Hagmann et al. 2008). Only the vectors of the diffusion map that match with the white matter are used because there is where the myelinated tracts exist. *Tractography* uses those reconstructed connections to make the match between cortical regions defined by standard atlas (i.e., DKA or AAL) (Tzourio-Mazoyer et al. 2002; Fischl et al. 2004; Hagmann et al. 2007; Rolls et al. 2015). The result is the SC matrix (Figure 1), a representation of the neural map. There are different parcellation criteria; ones are based mainly on the structural (i.e., myelinated tracts or cytoarchitecture), and others in functional (i.e., as the resting state networks) data. For example, the DKA is a structural parcellation that uses the gyrus and sulcus to define 66 cortical regions (Fischl et al. 2004; Desikan et al. 2006). In the Hagmann connectome, a connection between cortical regions  $i$  and  $j$  was defined after applying a normalization to the raw number of fibers

that connect them. The weight of each connection was normalized by the number of tracts and relative volume among two connected cortical regions (details in Hagmann et al., 2008).

## 1.2. Structural connectivity matrix

The structural connectivity matrix, represented by the  $C_{ij}$  matrix, shows the pair-wise connection between cortical regions of the connectome, in which columns show the inputs and rows the outputs of each area (Figure 3). Each entry of the matrix is a pair-wise excitatory connection. For example, in Figure 3A, the entry  $C_{21}$  is a connection from node 1 to 2. The  $C_{ij}$  can be decomposed in the **adjacency matrix** ( $A_{ij}$ ) (or connectivity pattern) (Figure 3A, bottom) and the **weighted matrix** ( $w_{ij}$ ) (or weighted connectivity) (Figure 3B, bottom), which is shown in equation 1:

$$C_{ij} = w_{ij} A_{ij}$$

Equation 1

The the adjacency matrix  $A_{ij}$ , correspond to the binarized values of connectivity in the network:

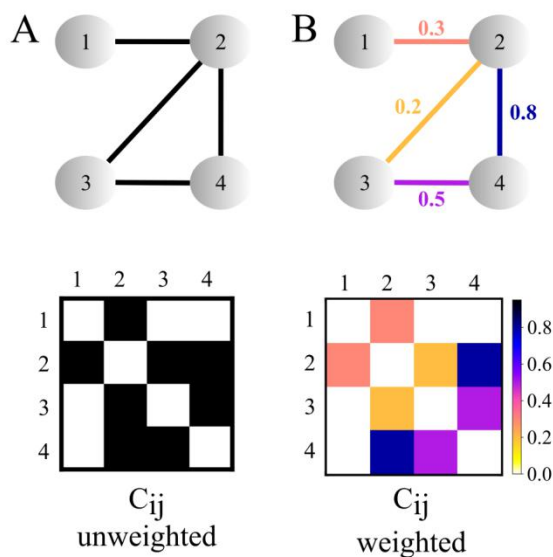


**Figure 3. The scheme of unweighted and weighted structural connectivity.** (A) Top, network nodes are represented in circles, in which in the middle is showing their number of connections. Bottom, matrix representation of the network, the entries indicate the presence (*black*) or absence (*white*) of a pair-wise link between the nodes. Rows correspond to the afferences and in columns the efferences of each node. (B) Top, in this case, the connections are weighted. Bottom, the weighted matrix representation, in which the color bar reflects the values of the pair-wise links. In the connectome field, those values tend to represent the pondered weight of the myelinated tracts, the number of tracts that connect two circuits, or even the number of synapsis between two neurons.

The  $A_{ij}$  allows disentangling from the weighted variability on the connectome (Figure 3A). The  $w_{ij}$  matrix contains the weight diversity of each network, as is shown in Figure 3B. Note that the use of  $w_{ij}$  or  $C_{ij}$  is equivalent (Fornito et al. 2016).

## 2. Network analysis

### 2.1. Local organization

To measure the local organization on a network, I used the degree  $k_i$  for unweighted, and strength  $s_i$  for weighted networks.  $k_i$  is the number of connections in the node  $i$  from other  $j = 1 \dots N-1$  nodes (Figure 3A). The degree is defined as (Fornito et al. 2016):

$$k_i = \sum_{i \neq j} A_{ij}$$

Equation 2

Whereas the  $s_i$  is the sum of the weighted connections in a node  $i$  from  $j = 1 \dots N-1$  nodes of the network (Lynall et al. 2010; Rubinov and Sporns 2010) (Figure 3B). In an weighted network, the strength is defined as:

$$s_i = \sum_{i \neq j} w_{ij}$$

Equation 3

The strength of a node can be decomposed as the sum of its in-strength,  $s_{i-in}$  (i.e., the sum of inputs connections), and out-strength,  $s_{i-out}$  (i.e., the sum of outputs connections).

$$s_i = s_{i-in} + s_{i-out}$$

Equation 4

## 2.2. Mesoscale organization

A network can contain subsets of nodes that are more strongly inter-linked between them than on average. I identify this mesoscale organization of a network using a core decomposition which reveals its core-periphery organization. Focusing first on unweighted graphs, we define as  $k$ -core a subgraph –i.e. a subset of nodes and the links interconnecting them– in which all the member nodes have at least  $k$  neighbours within the subgraph (Hagmann et al. 2008; Kitsak et al. 2010; Betzel et al. 2018). The larger  $k$  is, the more difficult is to identify subgraphs that satisfy the  $k$ -core criteria, resulting in increasingly tighter cores (Figure 4). Any node member of a  $k$ -core will also belong to any  $k'$ -core with  $k' < k$ , resulting in an “onion-like” nesting of progressively denser cores, up to a maximum value  $k_{max}$  such that no  $k$ -core exists for any  $k > k_{max}$ . The largest value for  $k_{max}$  defines the core of the network, called  $k_{max}$ -core defines (see Results 2, Figure 21C right) (Alvarez-hamelin et al. 2006; Kitsak et al. 2010; Harriger et al. 2012).

These definitions of cores and shells can be naturally generalized from unweighted to weighted networks by replacing the notion of node degree (discrete number of outgoing and ingoing connections) with the notion of node strength (sum of the continuous weights of outgoing and ingoing connections). Hence, an  $s$ -core is a subgraph such that all its nodes are connected between them with a strength larger or equal than  $s$ . There is a  $s_{max}$ -core, such that  $s$ -cores with  $s > s_{max}$  do not exist anymore. In addition, one can define a smooth  $s$ -shell as a set of nodes belonging to  $s'$ -cores with  $s < s' < s + \Delta s$  but not to the inner  $s$ -core (where  $\Delta s$  sets a precision at which continuous  $s$  values are quantized). After a quick exploration among the connectomes, I set the analysis of  $s$  in a range between 0 and 0.8 with steps of  $\Delta s = 0.001$ .

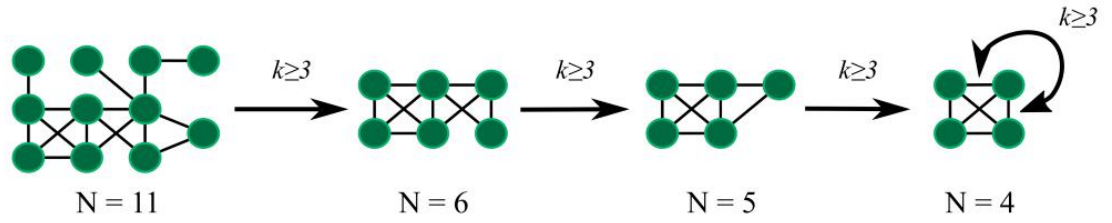


**Figure 4. Diagram of the  $k$ -core decomposition algorithm.** The  $k$ -core decomposition is used to extract the unweighted core nodes in the networks. In each step, the nodes ( $N$ ) that have a degree  $< k_i$  are removed in successive steps until the sub-set remains constant. The four core nodes are interconnected with at least  $k_i=3$ . In the case of weighted networks, the  $s$ -core decomposition extracts the core nodes based on their strength ( $\geq s_i$ ).

Also, I defined the  $s_{max}$  of the inputs and the outputs of the network. This was made by evaluating either the in- $s_{max}$  and out- $s_{max}$  of the network for the inputs and outputs, respectively. Similarly, cores are defined as in- $s_{max}$ -core in the case of inputs and the out- $s_{max}$ -core in the case of the outputs.

### 2.3. Global organization

To measure the global organization of a network, I used the small-world index,  $\sigma$ . This metric measures the ratio between integration and segregation of a network, i.e., a ratio of the normalized characteristic path length and the normalized clustering coefficient of the network (Humphries and Gurney 2008; Humphries et al. 2006).

**The characteristic path length.** The path length is the topological distance between two nodes in the network. The characteristic path length (cpl) is the mean shortest path between all the nodes of a network. The cpl is measured using the fact that if  $(A_{ij})^n = 1$ , there exists a path between  $i$  and  $j$  nodes of length  $n$  (Fornito et al. 2016, pp-214). Thus, the shortest path between  $i$  and  $j$  is the minimal value of the exponent  $n$  such that  $(A_{ij})^n$  is different from zero. The cpl of a network was normalized using a  $cpl_{random}$  from a random equivalent network (Humphries et al.

2006), which was constructed using the Maslov & Sneppen algorithm over the analyzed network (Maslov and Sneppen 2002) (described in detail in the next section). The normalized characteristic path length  $\lambda$  is the ratio:

$$\lambda = \frac{\text{cpl}}{\text{cpl}_{\text{random}}}$$

Equation 5

**The clustering coefficient.** The clustering coefficient (cc) is measured as the triangles of nodes formed when a node  $i$  is connected to any neighbors  $k$  and  $j$ . If the node  $k$  and  $j$  are also connected, the triangle is **closed**. If the  $k$  and  $j$  are unconnected, the triangle is **open** (Fornito et al. 2016). The cc of a node  $i$  is measured as:

$$cc_i = \frac{2t_i}{k_i(k_i - 1)}$$

Equation 6

Where  $k_i$  is the degree of the node  $i$ , and  $t_i$  is the number of *closed triangles* attached to node  $i$ . To calculate the clustering coefficient of the network, I averaged their local clustering values:

$$cc = \frac{1}{N} \sum_{i=1}^N cc_i$$

Equation 7

As in the case of cpl, I normalized the clustering coefficient ( $\gamma$ ) with the  $cc_{\text{random}}$ , built using the method described above (Maslov and Sneppen 2002). The equation is:

$$\gamma = \frac{CC}{CC_{\text{random}}}$$

Equation 8

**The small-worldness ( $\sigma$ ) metric.** The small-worldness of a network ( $\sigma$ ) is a ratio of the normalized clustering coefficient ( $\gamma$ ) and the normalized characteristic path length, ( $\lambda$ ) of the network:

$$\sigma = \frac{\gamma}{\lambda}$$

Equation 9

A network has the small-world property when  $\sigma > 1$  (Humphries et al. 2006; Humphries and Gurney 2008), maintaining at the same time a high clustering coefficient and a short characteristic path length. Thus, it is a description at the global level. I found that of the human connectome was  $\sigma = 1.63, \pm 4.3 \times 10^{-3}$ , its  $\lambda$  was  $1.07, \pm 5.4 \times 10^{-4}$ , and its  $\gamma$  was  $1.74, \pm 4.6 \times 10^{-3}$ . Figure 7A shows an example of the  $SW_{\text{hw}}$  network, which has a similar small-worldness value of the human connectome. Figure 7B shows the small-worldness of the Human,  $Human_{\text{hw}}$ ,  $DPR_{\text{hw}}$ , and  $SW_{\text{hw}}$ . The  $SW_{\text{hw}}$  networks have more similar small-worldness values with Human than  $DPR_{\text{hw}}$ . Thus, the human connectome presents the small-world feature, and the  $SW_{\text{hw}}$  networks are suited to study it (Hagmann et al. 2008).

## 2.4. Network toolbox

Network analyses and structural models used in this thesis were carried out using the Python modules *bctpy* (<https://github.com/aestrivex/bctpy>) and *brainconn* (<https://github.com/tsalo/brainconn>), both python implementations of the publicly available Brain Connectivity Toolbox (Rubinov and Sporns 2010).

### 3. Structural surrogate models

To make valid comparisons with the human connectome, I used structural models that split topological and weighted network properties (Opsahl et al. 2008; Alstott et al. 2014). Also, all the connectomes used, either human or other organisms, were adjusted to maintain the overall strength (15.3) of the human dataset of Hagmann and colleagues.

#### 3.1. Unweighted surrogate connectome (uSCs) models

Unweighted surrogate connectomes (uSCs) models have a uniform weight in their connections equal to the mean of human connection weight,  $1,332 \times 10^{-2}$ . I made three types of uSCs:  $\text{Human}_{\text{hw}}$ , that preserves the backbone of human connectome without its weight distribution (Figure 5); Degree-Preserving Random ( $\text{DPR}_{\text{hw}}$ ) ensemble that maintain the degree distribution of human connectome, but disrupt its high order relationships (Maslov and Sneppen 2002; Rubinov and Sporns 2010; Gollo et al. 2015; Fornito et al. 2016) (Figure 6); and Small-World ( $\text{SW}_{\text{hw}}$ ) networks that preserve the ratio between segregative and integrative capacities (Humphries and Gurney 2008; Humphries et al. 2006; Watts and Strogatz 1998)

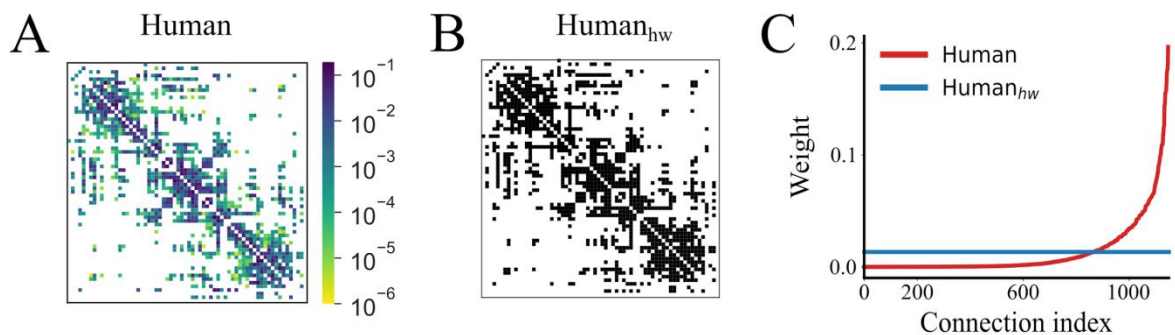


**Figure 5. The  $\text{Human}_{\text{hw}}$  connectome. (A-B)** The structural connectivity matrix of (A) Human and (B)  $\text{Human}_{\text{hw}}$  (with homogeneous weights in its connections). (C) Sorted connection weights of Human (red) and  $\text{Human}_{\text{hw}}$  (blue) connectomes. Note the heterogeneity of values in the Human. Both connectomes have 1.148 connections, and 15.3 of overall strength.

(Figure 7). The specific degree distributions and node relationships are discarded in the  $SW_{hw}$  ensemble. Thus, the uSCs evaluate the connectivity pattern, degree distribution, and small-world organization of the human connectome.

I built 100  $DPR_{hw}$  networks with the Maslov and Sneppen algorithm (Maslov and Sneppen 2002), and Figure 6B shows how it works. First, it chooses two pairs of connected nodes that simultaneously are disconnected, and then the algorithm makes two new connections between the unconnected pairs. In this way, the network changes its connectivity pattern, whereas each node conserves its number of connections. The  $DPR_{hw}$  maintain the number of nodes, edges, and the degree distribution of the human connectome (Figure 6C) (Telesford et al. 2011; Rubinov and Sporns 2010; Gollo et al. 2015; Fornito et al. 2016). I used the function *makerandCIJdegreesfixed* from bctpy, setting the parameter from the in-degree and out-degree of the human connectome.

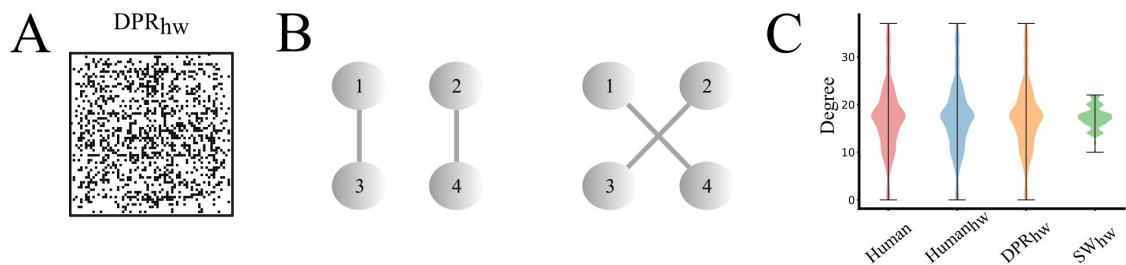


**Figure 6. The  $DPR_{hw}$  connectome.** (A) One representative example of the Degree-Preserving Random ( $DPR_{hw}$ ) structural connectivity matrix with homogeneous weights. (B) An illustrative example of the Maslov & Sneppen algorithm, adapted from Fornito et al., 2016. The algorithm was applied one hundred times to the Human to build the  $DPR_{hw}$  connectomes. (C) Degree distribution of Human,  $Human_{hw}$ ,  $DPR_{hw}$ , and  $SW_{hw}$ .  $DPR_{hw}$  connectomes have the same degree distribution, the number of connections (1.148), and overall strength (15.3) of the Human.

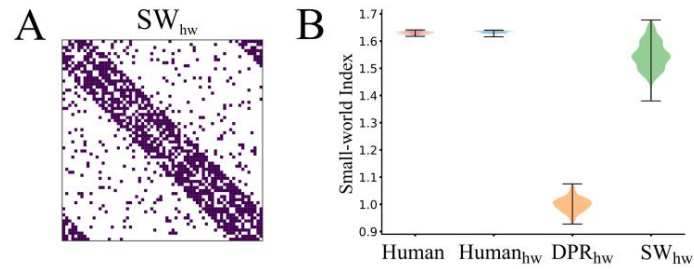


**Figure 7. The  $SW_{hw}$  connectome. (A)** One representative example of the Small-World ( $SW_{hw}$ ) structural connectivity matrix with homogeneous weights. **(B)** Small-world index of Human,  $Human_{hw}$ ,  $DPR_{hw}$ , and  $SW_{hw}$ . Note that the precise value of the small-world index depends on the random network used to normalize. Thus, its value is not deterministic, as can see in the error bars of the Human. The  $SW_{hw}$  connectomes conserve the number of connections (1.148), and overall strength (15.3) of the Human.

The  $SW_{hw}$  networks were used to preserve the global organization of the human connectome (Watts and Strogatz 1998; Humphries et al. 2006). In the case of  $SW_{hw}$  networks, 1.000 networks with 66 nodes and 1.148 edges were built using the Watts and Strogatz Small-World algorithm (Watts and Strogatz 1998). The Watts and Strogatz algorithm starts from a lattice network. Then it is defined as the probability of reconnection  $p$  of each connection. The one thousand  $SW_{hw}$  networks are reduced to one hundred that had a similar value of the small-world coefficient ( $\sigma$ ) of the human (Humphries and Gurney 2008; Hagmann et al. 2008; Alstott et al. 2014; Fornito et al. 2016) (Figure 7B). The  $p$  was adjusted to fit the human connectome to the  $\sigma$  parameter as well as the more similar  $k_{max}$  in the  $k_{max}$ -core sub-network. Notice that it was challenging to obtain slower values for the  $k_{max}$  because of the lattice structure of the source network (Kitsak et al. 2010).

### 3.2. Weighted surrogate connectome (wSCs) models

Weighted surrogate connectome (wSCs) models preserve the weight distribution of the human connectome, disrupting its pair-wise weight relationships (Opsahl et al. 2008; Alstott et

al. 2014; Fornito et al. 2016). I made a vector that contains the connection weights of the human connectome, and with a random permutation, the weights were assigned to the connections of the  $\text{Human}_{\text{hw}}$ , the  $\text{DPR}_{\text{hw}}$ , and the  $\text{SW}_{\text{hw}}$  networks, creating their weighted versions. I built 60 different instances of  $\text{human}_{\text{rw}}$ ,  $\text{DPR}_{\text{rw}}$ , and  $\text{SW}_{\text{rw}}$  networks (Figure 8). Indeed, each of the transformed  $\text{DPR}_{\text{hw}}$  and  $\text{SW}_{\text{hw}}$  networks came from a different network instance (i.e., are different).

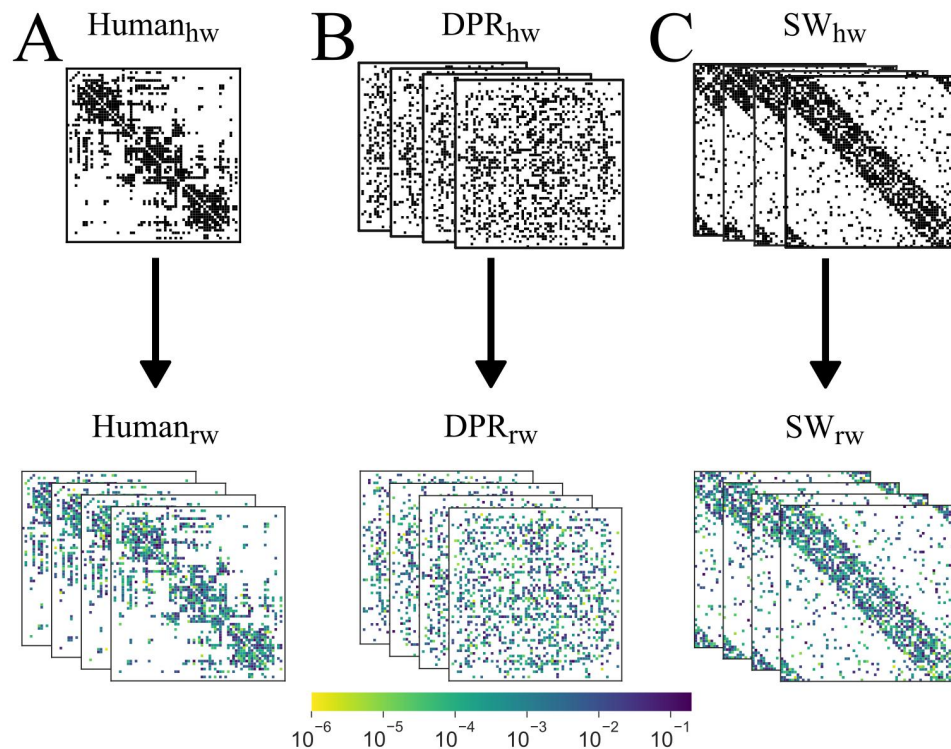


**Figure 8. The weighted surrogate connectomes conserve the weight distribution of the Human.** The values were assigned by random permutation of Human connections to create: (A) 60  $\text{Human}_{\text{rw}}$  from  $\text{Human}_{\text{hw}}$ ; (B) 60  $\text{DPR}_{\text{rw}}$ , from 60  $\text{DPR}_{\text{hw}}$ ; and (C) 60  $\text{SW}_{\text{rw}}$ , from 60  $\text{SW}_{\text{hw}}$ .

## 4. The whole-brain mean-field model of cortical activity

### 4.1. Mean-field model (MFM) of cortical activity

I used the mean-field model (MFM) as a generator of local cortical activity. The MFM comes from a mean-field dimensionality reduction of a large network of *integrate and fire*

neurons. In 2013, Deco et al. (2013b) modified it to capture only the NMDA-associated dynamics. With this reduction, the number of neural elements to be computed drops dramatically, and still preserves the ability to reproduce slow frequency features of resting-state functional data in static (Deco et al. 2013; Messé et al. 2015) and dynamic conditions (Hansen et al. 2015). Then, the MFM operates under the assumption that the time constant of the NMDA (N-methyl-D-aspartate) receptor dominates the time evolution of the system. Thus the local dynamics of a cortical area are explained by the variable  $S_i$ , i.e., the open fraction of NMDA channels (Hlinka et al. 2011; Deco and Jirsa 2012; Deco et al. 2013; Moutard et al. 2015). The equations of the model are:

$$\begin{aligned}\frac{dS_i}{dt} &= -\frac{S_i}{\tau_s} + (1 - S_i)\gamma R_i \\ R_i &= \frac{(a\chi_i - b)}{1 - e^{-d(a\chi_i - b)}} \\ \chi_i &= \omega J_N S_i + J_N G \sum_{j=1; j \neq i} C_{ij} S_j + I_0\end{aligned}$$

Equation 10

$S_i$  (do not confound with the strength lower case  $s_i$ ) is the open fraction of NMDA channels,  $R_i$  is the mean firing rate, and  $\chi_i$  represents the total synaptic input of the  $i$  cortical. The coupling gain parameter,  $G$ , was systematically explored between  $0.05 \leq G \leq 15$ , with steps  $\Delta G=0.005$ .  $C_{ij}$  is the SC matrix with the connections from node  $j$  to node  $i$ .  $\tau_s = 100$  ms is the NMDA decay time constant,  $\gamma=0.641$  is a kinetic parameter,  $a=270$  (V • nC)<sup>-1</sup>,  $b=108$  Hz,  $d=0.154$  s,  $\omega=0.9$  is the relative strength of recurrent connections within the  $i$  region,  $J_N=0.2609$  nA is the intensity scale for synaptic currents, and  $I_0=0.3$  nA is the basal input which sets the regional excitability level (Table 2). The network simulations were run for 120 seconds with steps of  $\Delta t=1$ ms, using

an Euler integration scheme (Butcher 2016). In the Chapter 1, I show how these parameters were chosen.

## 4.2. Computer simulations and fixed-point analysis

To explore the non-linear behavior of the model and the existence of multiple attractors, I analyzed the model dependency on initial conditions (ICs). The local dynamics of each network's node was started in a range of fixed ICs ( $0 \leq S_i \leq 1$ ) with steps of  $\Delta S_i = 0.01$ . Following Deco et al., 2013b and Hansen et al., 2015, I used the maximal value of  $R_{\mathcal{S}}$  at the end of the simulation, called  $R_{max}$ , a proxy for the network state (see Results chapter 1, Figure 10). I modified the range of ICs used by Hansen et al., 2015 to the range of  $0 \leq S_i \leq 0.1$  for *Low* ICs and  $0.3 \leq S_i \leq 1$  for *High* ICs because they optimize the difference between ignition and baseline activity among the coupling gain (see Results chapter 1 Figure 14). The simulations were run with ICs chosen from a uniform random distribution in the High and Low ICs range.

## 4.3. Ignition in the whole-brain model: Bifurcation points and bistable range

The coupling gain of the network, the parameter  $G$ , was varied in the range  $0.5 \leq G \leq 15$  with steps  $\Delta G = 0.005$  to evidence the bistable range of ignition. That was done with both High and Low ICs, and then, I extracted the  $R_{max}$  vs.  $G$  vector. This vector was used to detect the bifurcations of the bistable range at the *ignition point* or  $G_-$ , and at the *flaring point* or  $G_+$ , using a customized python routine, which identifies when the difference of two consecutive points of the  $R_{max}$  vs.  $G$  vector was higher than two standard deviations.

**Table 2. The parameters of the MFM implemented by Hansen et al., 2015, based on Deco et al., 2013.**

Parameter name	Value
$J_N$	0.2609 nA
$\tau_s$	100 ms
$\gamma$	0.641
$I_0$	0.3 nA
$\omega$	0.9
$G$	$0.5 \leq G \leq 15$
$C_{ij}$	66 cortical regions
<b>Time of simulation</b>	15 s
$\Delta t$	0.1 ms
$a$	$270 (V \cdot nC)^{-1}$
$b$	108 Hz
$d$	0.154 s

## 5. Node ignition analysis

### 5.1. Thresholding of node activity

The thresholding of activity is the basis for the ignition analysis (Messé et al. 2015; Deco and Kringelbach 2017; Tagliazucchi et al. 2012). Initially, the threshold was established as a rise of more than two standard deviations of the baseline activity for node  $i$ , in a range of parameter  $G$ . However, this algorithm failed to detect the rise of activity in the network because it included nodes that had low activity regime. To fix that, I examined the typical values of  $R_i$ s in the simulations and established heuristic criteria for the threshold. A node with  $R_i \geq 5$  was assigned to the ignited subset (i.e., with *high* mean firing rate); otherwise, it was part of the baseline subset (i.e., *low* mean firing rate).

### 5.2 Relationship between ignition and network organization

To study the relationship between structure and cortical ignition through the bistable range, I calculated the Spearman rank correlation (Betz et al. 2018) between the ignition  $G$  value of each node and its  $s_{max}$  value (see materials and methods chapter). Note that the Spearman rank correlation is a non-linear metric that adjusts better to the concept of core and shells. The same procedure was repeated to calculate the correlation between the ignition  $G$  value and the (in/out) strength of the nodes. I used a bootstrap resampling of 10.000 replicas to estimate the confidence intervals of the Spearman rank correlation. The bootstrap resampling method provides a statistical significance of the obtained results.

## 6. The pruning of connectome's connections based on the network organization

The structural connections were systematically pruned based on the local and mesoscale organization. The pruning procedure has three steps: first (i) apply the network analysis (i.e., degree, strength,  $k$ -core, or  $s$ -core decomposition). Second (ii) select a node using the chosen network level. Third (iii), randomly prune of one of its connections.

To prune the connections from *highly connected node at local level* (i.e., based on degree or strength) I proceeded to: (1) analyze the degree (or strength) of the network, (2) select the node(s) with the highest degree (or strength), and finally (3) randomly remove one of its connections. If more than one node has the highest degree (or strength), one of them was randomly picked.

To prune the *sparingly connected node at local level* (i.e., based on degree or strength), I change the point (2) from above to: “select the node(s) with the lowest degree (or strength), which also has more than one connection (to not disconnect the node from the network after the pruning procedure).

To prune the connections from *core at mesoscale organization level* (i.e., based on  $k$ -core or  $s$ -core decomposition), I proceed to: (A) analyze network with the  $k$ -core (or  $s$ -core) decomposition, (B) randomly select one node that was part of  $k_{max}$ -core (or  $s_{max}$ -core) subset, and (C) randomly remove one of its connections. This method could remove not only core-to-core connections but also core-to-periphery ones.

To prune the connections from peripheral *shells at the mesoscale organization level* (i.e., based on  $k$ -core or  $s$ -core decomposition), I change the point (B) from above to: ‘randomly select of one node that does not belong to  $k_{max}$ -core (or  $s_{max}$ -core) subset.

Finally, to evaluate the null hypothesis, I realized a random pruning, in which I took a node arbitrarily, and then randomly removed one of its connections. The pruning procedure removes 27 connections and then extracts the bifurcations  $G$  and  $G_+$  of the pruned network. This procedure is iterated to obtain 12 pairs of bifurcation points (removing in total 648 links) from each pruning of the network. Note that 13 pairs of bifurcation values were generated, and one comes from the unpruned (i.e., intact) network. The whole pruning sequence was repeated on 20 network instances of each type (20 Human, 20 Human<sub>hw</sub>, 20 Human<sub>rw</sub>, 20 DPR<sub>hw</sub>, 20 DPR<sub>rw</sub>, 20 SW<sub>hw</sub>, 20 SW<sub>rw</sub>).

Importantly, an additional rule was considered for the pruning procedure, in which no nodes were disconnected from the network when connections are removed.



## Optimizing the detection of cortical ignition in the whole-brain mean-field model

The cortical ignition framework proposes that the fluctuations in the brain dynamics are characterized by fast transitions between low and high activity periods, and that is a multi-scale phenomenon (Moutard, Dehaene, and Malach 2015; Deco and Kringelbach 2017). To study the structural mechanisms that contribute to this shifting in dynamics, I used a whole-brain MFM, which shows ignition in the collective cortical activity. Ignition was studied tangentially by Deco in 2013 and Hansen in 2015, where they showed that the model was ignitable at the network level. However, the parameters that they used are not optimized to display the network ignition. For example, the range of initial conditions for the network activity in which the ignition was maximized was not well defined. Here, I do a systematic study of the ignition in the simulations of the whole-brain MFM. Also, I optimized the detection of the network ignition for a broader range of excitability coupling.

### 1. The ignition in the cortical activity of the isolated MFM: Phase portrait and steady-state

In the model, when a cortical region is disconnected from the other regions, its dynamics are described as isolated, corresponding to the hypothetical idea of local activity without

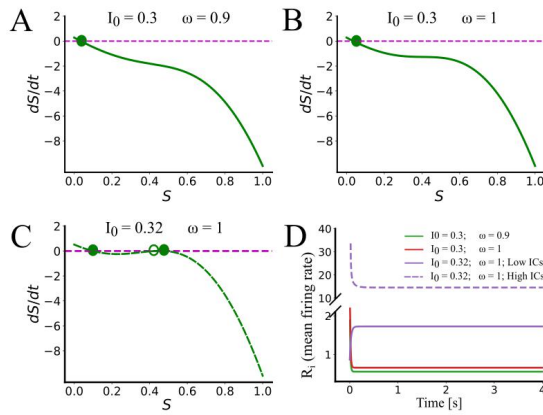


**Figure 9. Phase portrait and time-series of an isolated cortical region using the MFM.** (A-C) Three solutions as a function of  $I_0$  and  $\omega$  for an isolated node (A ( $I_0=0.3$ ;  $\omega=0.9$ ), B ( $I_0=0.3$ ;  $\omega=1$ ), and C ( $I_0=0.32$ ;  $\omega=1$ )). The dynamics of the isolated node gets two attractors in C. (D) Mean firing rate ( $y$ -axis) in time ( $x$ -axis) for the three sets of parameters. In purple (the isolated node with two attractors), segmented and solid lines are simulations started from High ICs ( $0.9 \leq S_i \leq 1$ ) or Low ICs ( $0 \leq S_i \leq 0.01$ ), respectively. The MFM with a single attractor (green and red) only displays a low mean firing rate.

external perturbations (Holcman and Tsodyks 2006). This approach is rooted in the notion that local changes of cortical activity could be mainly explained by the balance between excitation and inhibition (Wong and Wang 2006; Deco and Jirsa 2012) or neuromodulation (van den Brink, Nieuwenhuis, and Donner 2018; Medel et al. 2019; Li et al. 2019; Shine et al. 2019). Figure 9 shows the phase portrait of the MFM, in which the attractor (green circle) is the steady-state of the isolated cortical region.

The isolated dynamics were obtained in the MFM setting SC matrix to 0, as  $C_{ij} = 0$  (Equation 10, see materials and methods chapter). Except this, parameters of the MFM are used as it is described in Table 2, and the methods chapter. The dynamics of those parameters of the MFM has a unique equilibrium point for the variable  $S_i$  with value 0.034, as is shown in the phase portrait of Figure 9A. In other words, the cortical activity of the isolated MFM drops into a fixed-point attractor and, thus, cannot have an ignited steady-state.

To produce an ignited attractor in the isolated MFM, I followed the work of Hansen and colleagues (2015) and made a slight shift in the parameters  $\omega$  (from 0.9 to 1) and  $I_0$  (from 0.3 to 0.322). Those changes in the parameters show how the isolated MFM can have more than one attractor (Figure 9B-C) and, therefore, can be ignitable. The  $\omega$  parameter represents the gain of the recurrent activity, and setting it in 0.9 indicates the loss of 10% of the self-excitation in each

integration step. The increase of the self-excitability to 1 ( $\omega=1$ ) produces a shoulder at the higher activity of the variable  $S_i$ , shown in the phase portrait of Figure 9B. Moreover, when the basal excitatory input,  $I_0$ , is increased ( $\omega=1$  and  $I_0 = 0.322$ ), the system makes a qualitative shift in its space dynamics (Figure 9C), with the apparition of a stable attractor with higher activity (left filled green circle) than the preexisting stable attractor of low activity (right filled green circle). Also, an unstable attractor (empty green circle) emerges between the stable ones. Figure 9D shows the time-series of these three versions of the isolated MFM. The steady-state is reached at the end of the simulations. When the MFM has two stable attractors, the steady-state can be sustained at a high or low mean firing rate (purple lines). In conclusion, changes in the self-excitability and basal excitatory inputs are a plausible explanation for the local cortical ignition.

## 2. The ignition in the cortical activity of the whole-brain MFM: Human connectome adds diversity in the steady-state and generates network ignition

Even though simulations of isolated cortical regions help to understand local ignition, cortical regions are embedded in network topology (Lynn and Bassett 2019), with coordinated dynamics between them (Varela et al. 2001). It has been explored using a whole-brain MFM modeling approach that adds the human connectome and generates a richer activity landscape, in which the network can be ignited (Deco et al. 2013; Hansen et al. 2015; Honey et al. 2009). In this approach, each cortical region has the dynamics of the MFM, and they received ponderated inputs according to the human connectome. The human connectome comes from an average of 5 right-hand male subjects diffusion MRI data (Fischl et al. 2004; Hagmann et al. 2008). The connectome was parcellated following the Desikan-Killiany atlas (Desikan et al. 2006), which has 66 cortical regions (33 per hemisphere in Table 1) and contains 1.148 cortico-cortical

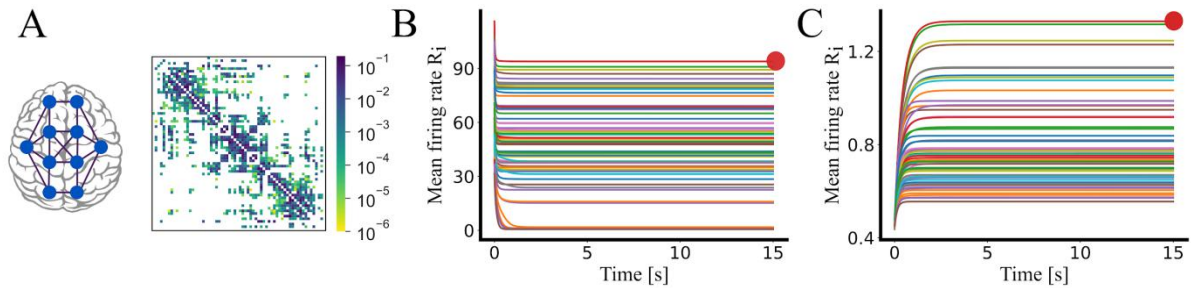


**Figure 10. The human connectome and its collective dynamics.** (A) The human connectome and (B) the time-series of the mean firing rate of its 66 mean-field model-based nodes. In the case of the coupled network, the simulation shows a diverse attractor landscape than the isolated node. Even the lowest  $R_i$  values are higher than in the isolated node. Coupling gain  $G=2.4$ , High ICs ( $0.9 \leq S_i \leq 1$ ), time simulated 15s, and time step  $\Delta t=0.1\text{ms}$ . (C) The mean firing rate of the model with the same parameters but with Low ICs ( $0 \leq S_i \leq 0.001$ ). The steady-state of this simulation stays at lower activity levels than the former, but still, its attractor landscape is more diverse than in the isolated node. Circle in Figures B and C show the node with the higher  $R_i$  value for the steady-state, the  $R_{\max}$ , and it was used to determine if the network activity was ignited or it was at a low baseline level.

connections (Figure 10A) (Hagmann et al. 2008). The connections are long-range excitatory, and they are represented as the entries of the  $C_{ij}$  matrix (Equation 10, Figure 10A).

Figures 10B-C show that whole-brain simulations generate a richer attractor landscape for each cortical region. In this landscape, each cortical region exhibits more diversity in its steady-state than in the case of the isolated MFM (Figure 9D). Moreover, there are (at least) two attractors at the network level. One in which all the cortical regions stay in a low *baseline network state* and another in which some cortical regions make a shift in their activity and enter in a high firing rate regime, which I call the *ignited network state*.

As in the case of the isolated MFM, the network activity state is determined by the initial conditions (ICs) of the variable  $S_i$  (The fraction of open NMDA channels) in each MFM. Figure 10B shows the model starting with random ICs from a low range ( $0 \leq S_i \leq 0.1$ ), whereas Figure 10C shows the case for High ICs ( $0.9 \leq S_i \leq 1$ ) (the range for Low and High ICs will be discussed below). To the naked eye, the steady-state of the simulation started from High ICs is in at least one order of magnitude higher than the simulation started from Low ICs (notice the difference in

the scale of the  $y$ -axis). As an indicator of the collective network state in each simulation, I use  $R_{\max}$ , which is the node with the highest activity at the steady-state ( $R_i$ ) among all the cortical regions, and it easily differentiates whether the network state was ignited or not.

Previous works did not have declared interest in the ignition on the network state, as they showed it tangentially at the level of the network. Because of this, the simulation parameters were not well optimized to display the network ignition. Thus, I evaluated the time of simulation, the time step, and the ICs proposed by the works of Hansen et al., 2015 and Deco et al., 2013b, detailed in Table 3.

## 2.1. Detection of the network steady-state is optimized by the time of simulation and time step

Optimizing the **time of simulation** is crucial in the collective dynamics because not enough time could fail to reach the steady-state in the network state. The network steady-state is captured with a long enough simulation, but also the simulation needs to be short to save computational resources. I optimized this trade-off to obtain the shorter time of simulation that shows the steady-state of all the nodes. The steady-state was measured as the variance of the  $R_{\max}$  in 20 simulations.  $R_{\max}$  values near to zero are indicative of high reliability in the network steady-state across simulations. Figure 11A-H shows deterministic simulations that ran for 0.1, 0.5, 2, 6, 12, 24, 60, and 120 s, with time steps of  $\Delta t=1$  ms using an Euler integration scheme (Butcher 2016). Figure 11I shows in each entry of the matrix the variance of  $R_{\max}$  obtained for the 20 simulations in a range of the coupling gain parameter ( $0.6 \leq G \leq 2.7$ , with steps of  $\Delta G=0.05$ ) and the time of simulation analyzed. The minimum time required to reach the steady-state was 6 s. To guarantee the steady-state of the system, I doubled it to 12 s in the following simulations. For comparison, the time for simulations is not specified in Deco et al., 2013b, whereas Hansen

**Table 3. The time simulation parameters to reach the steady-state in MFM used in the work of Deco (2013) and Hansen (2015).**

Parameter name	Deco et al., 2013	Hansen et al., 2015
Time of simulation	20 min	15 s
$\Delta t$	Not reported	0.1 ms (also reported 0.05 ms)
ICs	$0 < S_i < 1$	High $0.2 < S_i < 1$ Low $0 < S_i < 0.2$

and cols (2015) are set to 15s. Therefore, the simulation time used here is shorter than the reported in previous works optimizing the computational cost. It is interesting to notice that the  $R_{\max}$  shows a higher variance for the time of simulations in the lower values of the coupling parameter.

Another critical issue is the determination of the **time step** of the numerical integration, which has been proved as critical to observe structural effects on neural dynamics (Messé et al. 2015). If the time steps are short, it takes more time to get the results, and if they are too large, it can lead to integration errors. I evaluated the parameters proposed by Hansen (0.1 ms --also, they mention having used 0.05 ms obtaining the same results)) to optimize the trade-off between the large and short time-steps. Deco et al., 2013b do not report the time step implemented in their study. I tested this using the integration scheme of Euler (Butcher 2016), implemented in a python script (appendix 2). Figures 12A-H show the results for  $\Delta t=1000$  ms,  $\Delta t=500$  ms,  $\Delta t=100$  ms,  $\Delta t=50$  ms,  $\Delta t=10$  ms,  $\Delta t=5$  ms,  $\Delta t=1$  ms, and  $\Delta t=0.5$  ms. Figure 12I shows the variance of  $R_{\max}$  obtained for 50 simulations for each time step analyzed, in a range of the coupling gain ( $0.6 \leq G \leq 2.7$ , with steps of  $\Delta G=0.05$ ). The larger time step that maintains a low variance in the network steady-state ( $R_{\max}$ ) was  $t=10$ ms, and I use it in the following simulations. This time step is larger than the reported in previous works (Hansen et al. 2015; Deco et al. 2013); thus, it optimizes the computational costs. It is interesting to notice that the results for the

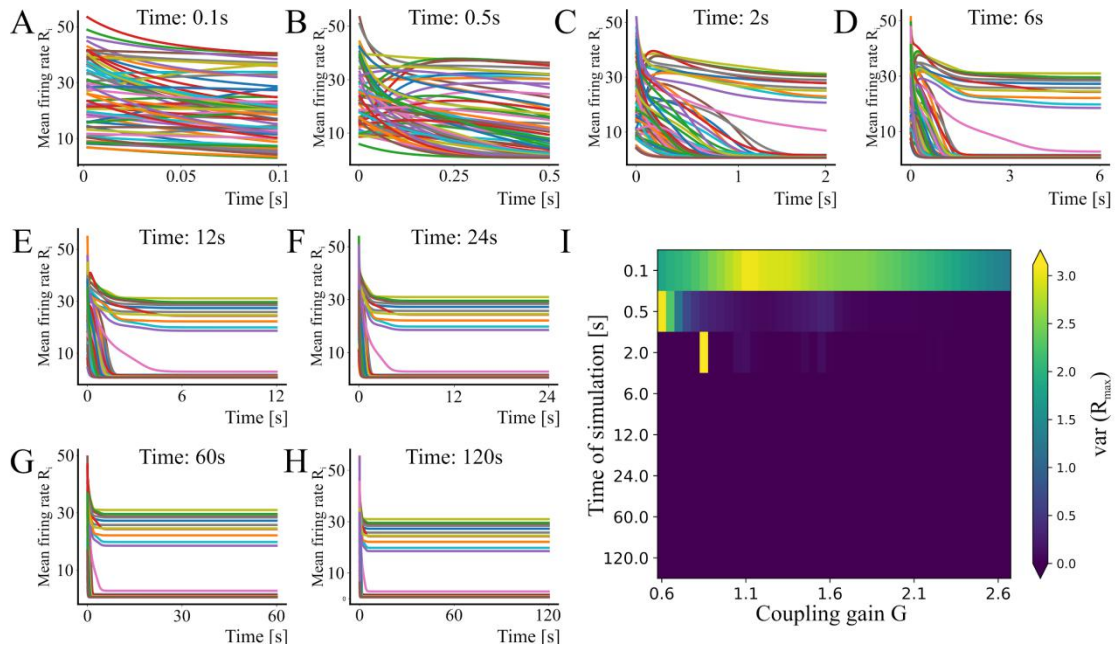


**Figure 11. Optimizing the time of simulations.** (A-H) The simulation was run for 0.1, 0.5, 2, 6, 12, 24, 60, and 120 s, with time steps of  $\Delta t = 1$  ms using an Euler integrations scheme. The coupling gain parameter of the time-series was set to  $G = 1$ . (I) To explore how the time of simulation ( $y$ -axis) affect the  $R_{max}$  in a range of the coupling gain  $G$  (between  $0.6 \leq G \leq 2.7$ , with steps of  $\Delta G = 0.05$ ) ( $x$ -axis), twenty simulations were run for each  $G$ . When the variance of the 20  $R_{max}$  (color bar) was minimized (i.e., near to 0), the steady-state of the time-series were more reliable. The ICs come from a uniform random distribution between  $0 \leq S_i \leq 1$ .

time-step are affected by the coupling gain in a range of coupling gain values.

## 2.2. Detection of the network steady-state is optimized by the initial conditions and is

spanned by the coupling gain of the MFM

Just like changes in the basal excitability and self-excitability make an isolated node ignitable (Figure 9), changes in the coupling gain parameter make the whole-brain model bistable in a defined range. Previous works show that the range of coupling gain  $G$  in which the whole-brain MFM displays ignition is also the range in which the simulations fit best with the

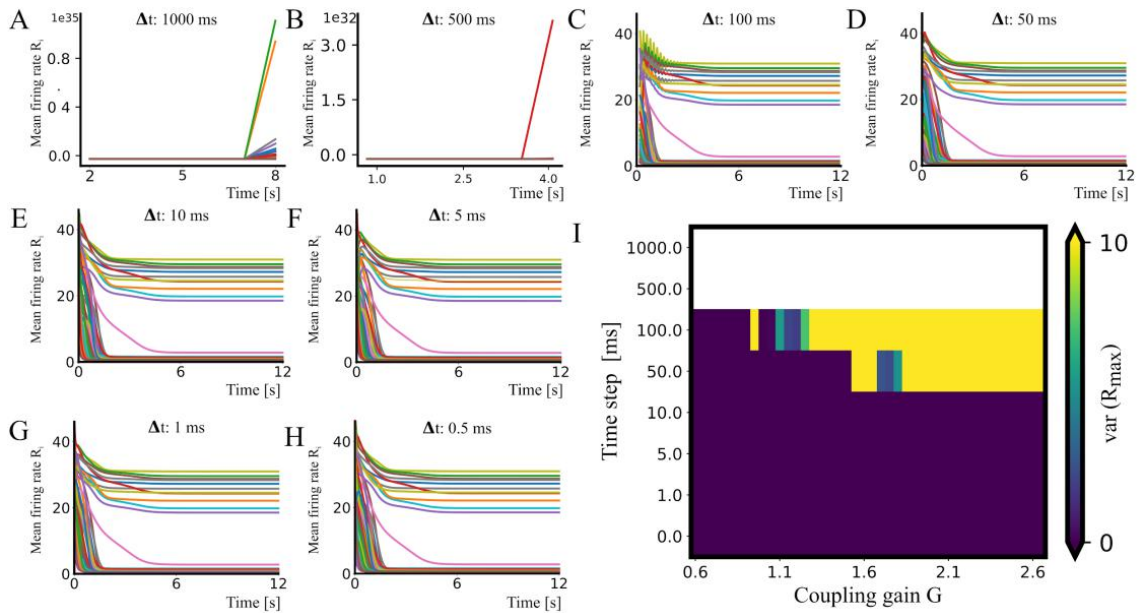


**Figure 12. Optimizing time step for simulations.** (A-H) The simulation was run 12 s with time steps of  $\Delta t=500$  ms,  $\Delta t=100$  ms,  $\Delta t=50$  ms,  $\Delta t=10$  ms,  $\Delta t=5$  ms,  $\Delta t=1$  ms,  $\Delta t=0.5$  ms and  $\Delta t=0.1$  ms using an Euler integration scheme. The coupling gain parameter of the time-series was set to  $G=1$ . (I) Twenty simulations were run for each coupling gain  $G$  in a range between  $0.6 \leq G \leq 2.7$ , with steps of  $\Delta G=0.05$  ( $x$ -axis) to explore how the time step ( $y$ -axis) affect the  $R_{max}$ . When the variance of the 50  $R_{max}$  (color bar) was minimized, i.e., near to zero, the integration for the steady-state was more reliable. The ICs come from a uniform random distribution between  $0.3 \leq S_i \leq 1$ .

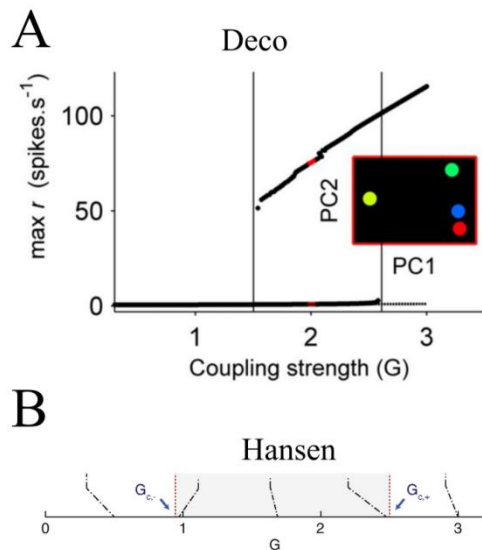


**Figure 13. Previous works had shown a range of ignition through the coupling gain of the whole-brain model.** (A) Deco and cols plot for the network state, in which between the vertical lines was observed, the bistable region of ignition. The coupling gain was explored in the range of  $0 \leq G \leq 3$ , without a reported time step. (B) Hansen and cols plot for the network state, in which the bistable region of ignition is in grey. The coupling gain was explored between the range of  $0 < G < 3.25$ , with  $\Delta G=0.05$  and a time step of 0.1 ms. Vertical black lines in A and red lines in B empirical functional connectivity (Deco et al. 2013; Hansen et al. 2015). It was presented this *bistability range*, with show the bifurcation points  $G_-$  (left) and  $G_+$  (right). Figures are extracted from the work of Deco et al., 2013b (A). and Hansen et al., 2015 (B), respectively.

al., 2015 (B), respectively.

boundaries at bifurcation  $G_-$  and  $G_+$ , in which a low baseline network state coexists with the ignited network state that has a high firing rate in a subset of cortical regions (Figure 10B-C). However, the coupling gain needed to maximize the range of the bistability in ignition has not been well parameterized. For example, in the work of Deco and colleagues (2013), they proposed a bistable range that depends on ICs, but they do not define any particular range ( $0 < S_i < 1$ ) (Figure 13A). In 2015, Hansen and colleagues proposed a strategy to maximize the bistable range, in which they split in two the range of ICs, with a notorious increase in the range of bistability through  $G$  (Figure 13B). Because the procedures to optimize the bistable range was not the primary goal of the previous works (Deco et al. 2013; Hansen et al. 2015), I proposed a new method to obtain the broadest bistable range. A first characterization was performed with all the nodes of the network having the same fixed value in the ICs. Figure 14A shows the exploration of the fixed ICs in a range of  $0.05 \leq S_i < 0.89$  (with steps of  $\Delta S_i = 0.01$ ) and coupling gain  $0.5 \leq G < 4$  (with steps of  $\Delta G = 0.001$ ). The color represents the average  $R_{max}$  value for 20 simulations. Notice that here is evaluated the average and not the variance of  $R_{max}$  because the aim is obtaining the network steady-state for each fixed ICs and not the reliability of the simulations.

The rectangle in Figure 14A shows the range in which the value of  $R_{max}$  depends on both  $G$  and ICs. The ignition network state starts at the ignition point  $G_- = 0.945$  and collapses at the flaring point  $G_+ = 2.545$ . In the  $G_-$ , the ignited network state is obtained with ICs higher than 0.3. Before the collapse in  $G_+$ , the baseline state is kept with ICs lower than 0.1. Fixed ICs between  $0.1 < S_i < 0.3$  follow a sigmoid-like shape through the range of  $G$ , as is shown in the rectangle. Thus, the reliability of  $R_{max}$  is enhanced using ICs outside this rectangle. The range for Low ICs is set as  $0 \leq S_i \leq 0.1$  and High ICs as  $0.3 \leq S_i \leq 1$ . Figure 14B shows the  $R_{max}$  for the range of coupling gain for Low and High ICs, showing the bistable range, similar to the work of Deco (2013b) and

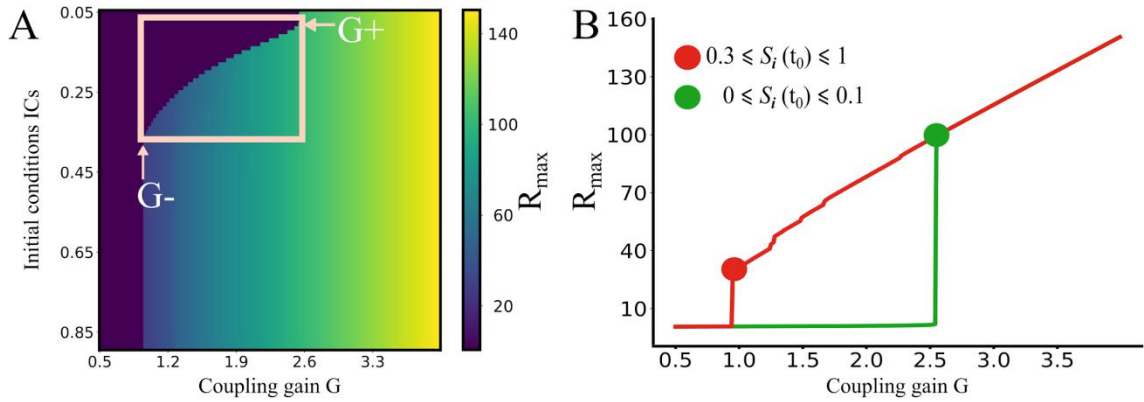


**Figure 14. The ignition in the whole-brain model was optimized in two ranges of initial conditions across the coupling gain parameter. (A)** The  $R_{\max}$  (color bar) is evaluated in a range of the coupling gain (between  $0.5 \leq G < 4$ , with steps of  $\Delta G = 0.001$ ) ( $x$ -axis) and the ICs ( $y$ -axis) space. With fixed ICs in a range between  $0.05 \leq S_i < 0.89$ , with steps of  $\Delta S_i = 0.01$  ( $y$ -axis), the ICs were explored, and thus, in each step, the initials  $S_i$  are equal in all the nodes. A rectangle shows the region in which the  $R_{\max}$  depends on both  $G$  and ICs. Also, the rectangle is shown the optimization for the existence of two states, one ignited and another with baseline activity. **(B)** The optimized ICs for ignition in a bistable range for the human connectome. The bifurcation  $G_-$  is 0.945 (red circle), and the  $G_+$  is 2.545 (green circle). The selected Low and High ranges for ICs are  $0 \leq S_i \leq 0.1$  (green) and  $0.3 \leq S_i \leq 1$  (red), respectively. The coupling gain was varied between  $0.5 \leq G < 4$ , with steps of  $\Delta G = 0.01$ .

Hansen (2015). I optimized the detection of the network ignition in the broadest possible range of the coupling gain parameter. It is important to remark that this method stresses the network dependence of the ignition, a key feature for the successive analysis.

**In conclusion, I show that the local and network ignition can be studied using the whole-brain model based on the local dynamics of the MFM. The model was optimized to show the network steady-state, in which the time of simulation and time-step had the optimal trade-off. Finally, the whole-brain model was tuned to display intrinsic ignition that was determined by the network activity state (represented by the initial conditions regime) and the coupling gain of global excitability.**





## The specific core-shell organization of the human connectome supports ignition in cortical activity

The whole-brain MFM of cortical activity can sustain ignition, a form of fluctuation in cortical activity, at the local and network level. One of the key and not well-understood factors underlying the fluctuations in cortical activity is the structural connectivity (Messé et al. 2014; Christopher J. Honey et al. 2007; C. J. Honey et al. 2009; Hütt, Kaiser, and Hilgetag 2014; Mišić et al. 2015; Messé et al. 2015; Joglekar et al. 2018; Deco et al. 2017; Lynn and Bassett 2019; Swanson, Hahn, and Sporns 2017; Betzel, Medaglia, and Bassett 2018). Thus, is the network organization of the human connectome a factor in the ignition of cortical activity? Moreover, if it is the case, at which level of the network organization (i.e., local, mesoscale, or global; unweighted or weighted) occurs this relationship? In this chapter, I show how the organization of the human connectome is related to the ignition of the cortical activity.

### 1. Cortical ignition and the network organization in the human connectome

#### 1.1. Human connectome: modeling of ignition and network analysis

Ignition and baseline activity are two network states and can be generated using deterministic simulations of the whole-brain MFM (parameters of MFM in Table 2; (Deco et al. 2013; Hansen

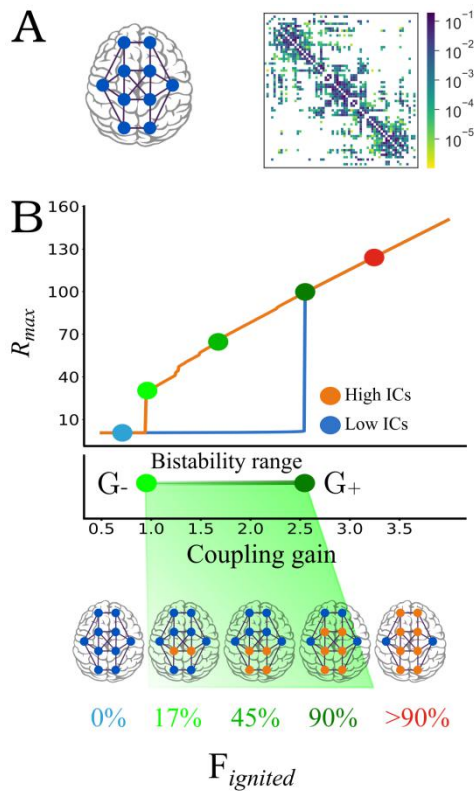


**Figure 15. The ignition in the whole-brain mean-field model of cortical activity wired by the human connectome.** (A) The structural connectivity matrix of the averaged five male subjects. The color bar shows the coupling weight between the two cortical regions. (B) Top, the network activity level ( $R_{max}$  values,  $y$ -axis) of the human connectome as a function of coupling gain ( $x$ -axis), starting either from Low ( $0 \leq S_i \leq 0.1$ , yellow) or High ( $0.3 \leq S_i \leq 1$ , purple) ICs. The network activity level is defined by the  $R_{max}$ , which is the highest steady-state ( $R_i$ ) value among cortical regions. Middle, the bistability range of the ignited network state, which is triggered at ignition point  $G_-$  from High ICs ( $G_- = 0.945$ , light green circle) and collapsing at the flaring point  $G_+$  using Low ICs ( $G_+ = 2.545$ , dark green circle). Bottom, the fraction of ignited nodes,  $F_{ignited}$  (threshold  $R_i > 5$ ), increasing from  $F \sim 17\%$  ( $n = 11$ ) in  $G_-$  to  $F \sim 90\%$  ( $n = 59$ ) in  $G_+$ . The coupling range was  $0.5 \leq G < 4$ , with steps of  $G = 0.001$ .

Hansen et al. 2015)). The whole-brain model uses the dynamics of MFM for each cortical region wired by the human connectome, which came from MRI data and had 66 cortical regions (33 per hemisphere) and 1.148 cortico-cortical connections (Figure 15A, Table 1; details in the previous chapter).

The activity state of the network depends on its ICs (variable  $S_i$ ). The ICs are randomly drawn from a uniform distribution in one of two ranges:  $0 \leq S_i \leq 0.1$  (Low ICs) and  $0.3 \leq S_i \leq 1$  (High ICs). Simulations were run for both ICs in a range of the coupling gain ( $0.5 \leq G < 4$ , with steps of  $G = 0.001$ ). To determine the network activity state, I used the highest steady-state activity ( $R_i$ ) of the network, denoted  $R_{max}$ . Also, several of the analysis involves the activity state of individual nodes (i.e., ignited or not). A node is said to be ignited when its firing rate is above a threshold

( $R_i > 5$ ); otherwise, it is classified as low baseline activity (Tagliazucchi et al. 2012; Deco and Kringelbach 2017) (see materials and methods chapter for details).

The whole-brain model with the human connectome is ignitable in a delimited range of the coupling gain, the *bistability range*, in which the network state can show either low or high  $R_{\max}$  values (Figure 15B, top). This result relies on the coupling gain and, especially, in the ICs of the model, namely High ICs and Low ICs. The network ignition is triggered at the *ignition point*  $G_-$ , where the simulations with High ICs generates an ignited subset of cortical regions ( $R_i > 5$ ) and ends at the *flaring point*  $G_+$ , where the simulations with Low ICs collapse into the high activity attractor (Figure 15B, top). The bifurcations  $G_-$  and  $G_+$  are stressed in the middle of Figure 15B. Within the bistable range, the *fraction of ignited nodes*,  $F_{\text{ignited}}$ , increases with the coupling gain parameter (i.e., the level of network excitability), from  $F_{\text{ignited}} \sim 17\%$  at  $G_-$  to  $F_{\text{ignited}} \sim 90\%$  at  $G_+$  (Figure 15B, bottom).

To study how ignition can be related to the underlying structure of the human connectome, the structural organization is characterized at **local** (Deco et al. 2017), **mesoscale** (Kitsak et al. 2010; Messé et al. 2015; Betzel, Medaglia, and Bassett 2018; Shine et al. 2019), and **global** (Mark D. Humphries and Gurney 2008; Gollo et al. 2015) level (Figure 16)

The local-level of a network is defined by the connections of each node and is used to study how the local organization is relevant for the whole-brain activity (Figure 16A). For *unweighted* network analysis, the degree ( $k_i$ ) is the number of connections of each node. For *weighted* network analysis, the strength ( $s_i$ ) is the sum of the weighted connections of each node (Fornito et al., 2016). This level could be thought of as the independent hierarchy because it does not take into account the existence of collective sub-structures. Two different network instances can have the same degree or strength distribution. Mesoscale of the network takes into account collective sub-structures, as groups of modules or cores. Cores are subsets of densely (for unweighted

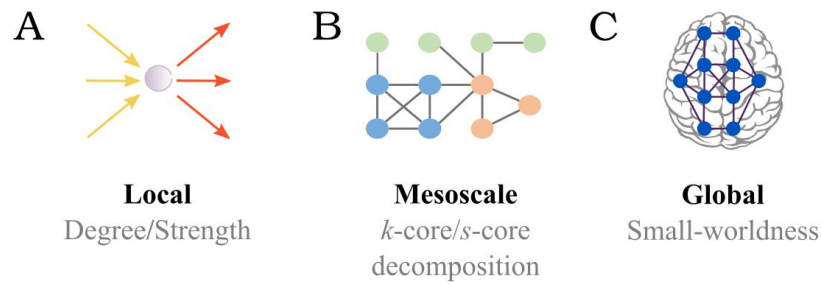


**Figure 16. Network analysis of different levels of the structural organization.** A scheme of the local, mesoscale, and global level of organization of the network. **(A)** The local level is represented by the sum of inputs and outputs of a cortical region. **(B)** The mesoscale level is measured with the core decomposition, composed by shells of incremental within-connected (or strongest) nodes. In the cartoon, *blue* nodes belonging to the 3-core, *orange* to the 2-core shell and *green* to the 1-core shell. **(C)** The global level considers the whole network, in which the *small-worldness* considers the ratio of integration to segregation.

networks) or strongly (for weighted networks) interconnected nodes (Hagmann et al. 2008; Kitsak et al. 2010; Betzel, Medaglia, and Bassett 2018) (Figure 16B; see materials and methods chapter for details). This measure is based on the fact that a network can contain subsets of nodes that are more strongly interconnected between them than on average. Focusing first on unweighted graphs, I define as *k*-core a subgraph -i.e., a subset of nodes and the links interconnecting them- in which all the member nodes have at least *k* neighbors *within the subgraph*. The larger *k* is, the more difficult it is to identify subgraphs that satisfy the *k*-core criteria, resulting in increasingly tighter cores. Any node member of a *k*-core will also belong to any *k'*-core with *k' < k*, resulting in an “onion-like” nesting of progressively denser cores, up to a maximum value  $k_{max}$  such that no *k*-core exists for any  $k > k_{max}$  (Figure 16B; see materials and methods chapter for an explanation of the algorithmic procedure), namely  $k_{max}$ -core.

These definitions of cores and shells can be naturally generalized from unweighted to weighted networks by replacing the notion of node degree (discrete number of outgoing and ingoing connections) with the idea of node strength (sum of the continuous weights of outgoing and ingoing connections). Hence, the *s*-core is the subgraph in which all the nodes have strength greater or equal than *s*. There is a  $s_{max}$ -core, such that *s*-cores with  $s > s_{max}$  do not exist anymore.

Besides, one can define a smooth  $s$ -shell as a set of nodes belonging to  $s'$ -cores with  $s < s' < s + \Delta s$  but not to the inner  $s$ -core (where  $\Delta s$  sets a precision at which continuous  $s$  values are quantized).

Global-scale takes into account the whole network properties, as its integrative and segregative capacities. For example, the small-world index ( $\sigma$ ) is defined as the ratio of characteristic path length to local clustering of the network (Figure 16C; see materials and methods chapter for details) (M. D. Humphries, Gurney, and Prescott 2006; Mark D. Humphries and Gurney 2008).

## 1.2. Ignition in cortical activity is structurally organized

The ignition of the cortical regions was paired to the local and mesoscale organizations of the human connectome, using the strength analysis and the  $s$ -core decomposition, respectively (the unweighted and also the global structural analysis (*small-worldness*) will be covered in the

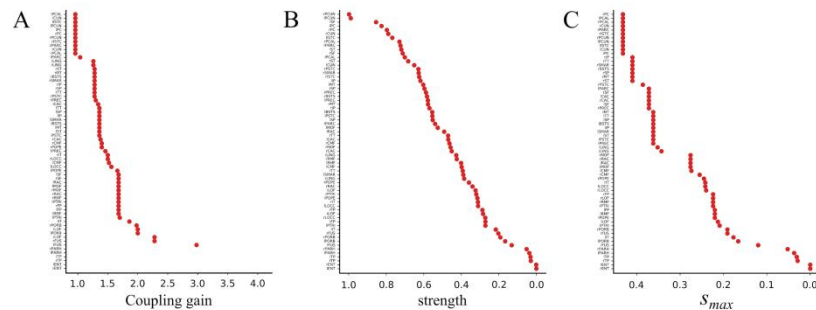


**Figure 17. The cortical regions ignite through the coupling gain and its structural organization.** (A) The cortical regions ( $x$ -axis) were associated and sorted to the coupling gain in the onset of ignition ( $y$ -axis). Initially, there is a small subset of the first ignited regions at the bifurcation  $G$ . (i.e., the *lowest*  $G$  value of ignition), and then regions are recruited through the coupling gain. The ignition of cortical regions follows a group onset rather than a linear increase of them. (B-C) Cortical regions of the human connectome ( $y$ -axis) are sorted either by (B) strength ( $y$ -axis) or (C) by  $s_{max}$  ( $y$ -axis). Note that the  $x$ -axis of structural measures is inverted to stress similarities with the onset of ignition. While the cortical regions follow a linear increase in the strength, they are added in chunks of similar  $s_{max}$ , i.e., the strongly interconnected cores

next section). Figure 17A shows the details of the coupling gain at which each cortical region first ignites, called in the following *ignition recruitment*. The nodes are sorted in terms of its ignition recruitment as a function of the coupling gain. Through the coupling gain, the ignition recruitment follows a stratified sequence in which a subset of nodes ignite earlier at the ignition point  $G$ . Then, the increase in the coupling gain adds groups of nodes rather than individual addition.

Is this subset of nodes that ignite at  $G$ . and then, the ignition recruitment associated with the structural organization? Figure 17B-C shows the cortical regions sorted by their strength and  $s_{max}$  values to stress the hierarchy of the structural organization at the local and mesoscale level. The strength shows a hierarchical linear organization, in which the strength of each node is different and follows a semi-linear dependency (Figure 17B). The ignition starts in a subset of nodes. Thus, it can not be deduced from the strength value of the nodes. Also, ignition recruitment is not linear through the coupling gain (Figure 17A). There are evident similarities between the ignition and  $s_{max}$  of the nodes, showing a stratified hierarchical organization (Figure 17C). As a matter of fact, this is not a coincidence.

I reorganize the data of Figure 17 to stress the structural organization and the ignition in the human connectome through the bistability range. Figure 18A shows the ignition recruitment of the nodes ( $y$ -axis) sorted by the coupling gain in which they first ignite ( $x$ -axis), and colored by their  $s_{max}$  value. Figure 18A shows two underscore results, **(1)** the trigger of ignition is supported by the  $s_{max}$ -core of the network (the highest  $s_{max}$  nodes, the red rows) and **(2)** the ignition recruitment seems to follow the core-shell organization through the coupling gain (in Figure 19 a scheme of this idea).

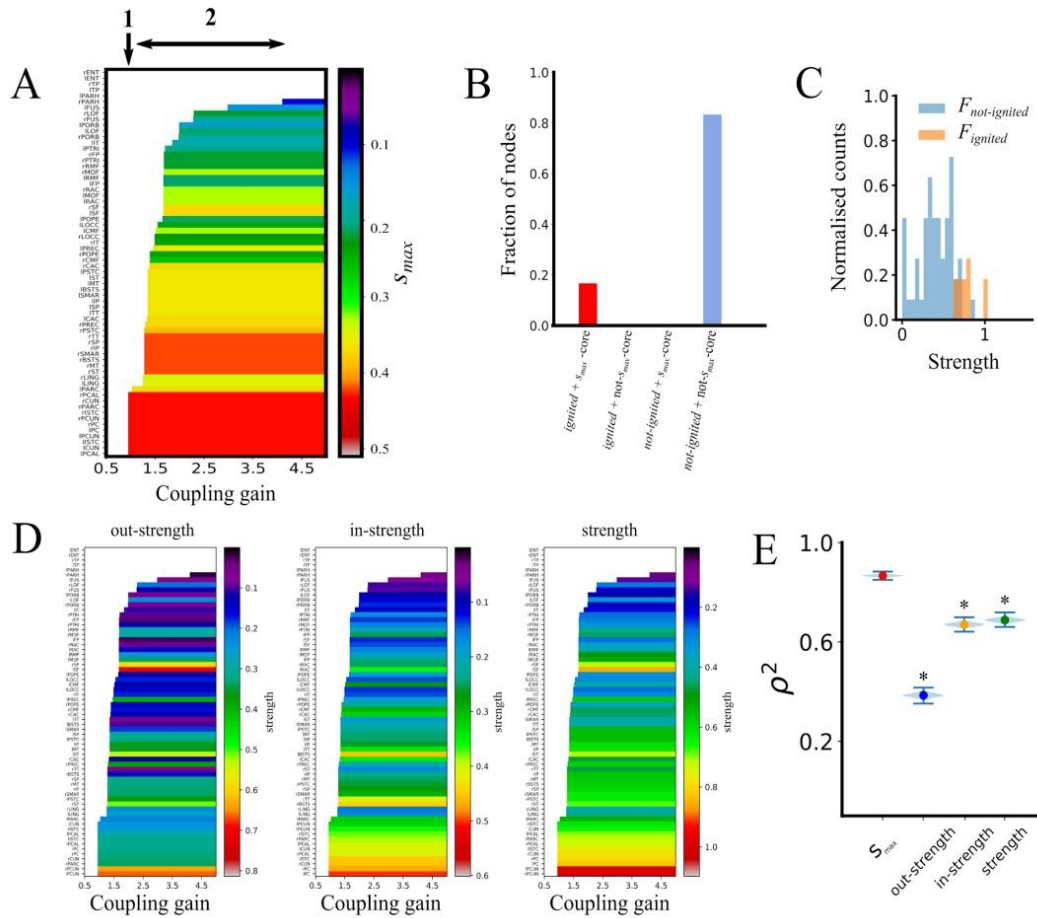


**Figure 18. Ignition in cortical activity is influenced by the core-shell organization of the human connectome.** (A) The relationship between ignition and  $S_{max}$  of each cortical region of the human connectome. The cortical regions in the  $y$ -axis are sorted according to the coupling gain  $G$  ( $x$ -axis) value at which they first ignite. Colour code shows the  $S_{max}$  for each of the ignited cortical regions of Human. (B) The bar plot shows the fraction of nodes that are ignited (red, orange) or not-ignited (green, blue) at the bifurcation  $G$ , and that belong to  $S_{max}$ -core (red, green) or not (orange, blue). (C) The strength distribution of *ignited* (orange) and *not-ignited* (blue) cortical regions at  $G$ . (D) Similarly to A, the relationship between ignition and the out-strength (left), in-strength (middle), and strength (right) of each cortical region. (E) Spearman rank correlation squared ( $\rho^2$ , explained variance) between first ignition  $G$  value of each cortical regions and its  $S_{max}$  (**0.867**, percentile (2.5, 97.5) = (0.858, 0.874), *red dot*), out-strength (**0.386**, percentile (2.5, 97.5) = (0.369, 0.402), *blue dot*), in-strength (**0.671**, percentile (2.5, 97.5) = (0.655, 0.684), *yellow dot*), and strength (**0.687**, percentile (2.5, 97.5) = (0.672, 0.702), *green dot*). Human shows a higher explained variance by the  $S_{max}$  than the in-, out-, or strength. The \* indicates a significant difference between the  $\rho^2$  of  $S_{max}$  and out-, in-, or strength. The significance of  $\rho^2$  was evaluated using 10.000 replicas from bootstrap resampling (violin plots).

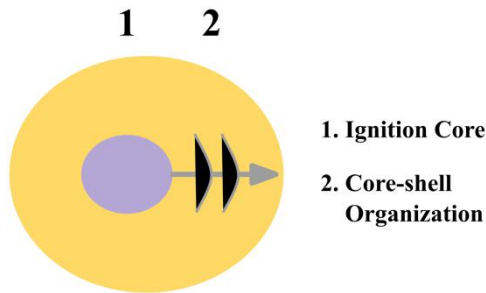


**Figure 19. Ignition scheme for core-shell organization of the human connectome.** The ignition of cortical activity can be split into (1) the trigger subset of regions, and the (2) recruitment of them through the coupling range. The ignition is triggered at  $G_c$  and it is perfectly correlated with the strongest core of the human connectome, the ignition core.

Thus, I call the ignition core to the ignited nodes at the bifurcation  $G_c$ , and that shows a strikingly one-to-one correspondence with the  $s_{max}$ -core of the human connectome (Figure 18B, red column). Consequently, the not ignited cortical regions do not belong to the  $s_{max}$ -core, as is shown in the blue bar. Moreover, being a strongly connected node does not determine the early trigger of the ignition of the cortical regions, as some of them are not ignited at the  $G_c$  (Figure 18C). Thus, for the Human, strength does not have a perfect match with the ignition core as achieved by the  $s_{max}$ -core. The cortical regions that belong to the *ignition core* are the pericalcarine cortex (**PCAL**), cuneus (**CUN**), paracentral lobule (**PARC**), isthmus of the cingulate cortex (**ISTC**), precuneus (**PCUN**) and posterior cingulate cortex (**PC**) (Table 4). Cortical regions of ignition core are present in both hemispheres, except in the case of **PARC**, which only is part of the left hemisphere.

Similar to Figure 18A, Figure 18D shows the sorted ignition recruitment, in which the color index is the out-strength (left), in-strength (middle), and strength (right) of each cortical region. By visual inspection, the ignition recruitment is not well captured by the strength index at the ignition point  $G_c$ , as can be noticed in the inconsistency of the color gradient in the y-axis of Figure 18D. To quantify the relationship between the structural organization (the strength or  $s_{max}$

**Table 4. The identity of the ignited cortical regions at bifurcation G..** Ignited regions are present in both hemispheres, except in the case of PARC, which is ignited only in the left hemisphere. P, present, A, absent.

Cortical Regions	Left Hemisphere	Right Hemisphere
<b>Pericalcarine Cortex (PCAL)</b>	P	P
<b>Cuneus (CUN)</b>	P	P
<b>Paracentral Lobule (PARC)</b>	A	P
<b>Isthmus of the cingulate cortex (ISTC)</b>	P	P
<b>Precuneus (PCUN)</b>	P	P
<b>Posterior Cingulate Cortex (PC)</b>	P	P

index) and the ignition recruitment, the Spearman rank correlation,  $\rho$ , was calculated between them. The  $\rho$  evaluates paired rank relationships, rather than a linear one; thus it is best suited to analyze the ignition recruitment because the ignition appears to take place in chunks of nodes, rather than individual incorporation of them. Figure 18E shows the explained variance of the Spearman rank correlation ( $\rho^2$ ) and it is calculated between ignition recruitment and the  $s_{max}$  (**0.867**, percentile (2.5, 97.5) = (0.858, 0.874)), out-strength (**0.386**, percentile (2.5, 97.5) = (0.369, 0.402)), in-strength (**0.671**, percentile (2.5, 97.5) = (0.655, 0.684)), and strength (**0.687**, percentile (2.5, 97.5) = (0.672, 0.702)). The \* shows the significative difference between  $s_{max}$  and out-, in-, and strength of the human connectome. The significance of  $\rho^2$  was evaluated using 10.000 replicas from bootstrap resampling. The explained variance of ignition recruitment in cortical regions is higher for the  $s_{max}$  than for the in-, out-, or strength. Also, the explained variance of the ignition recruitment and the strength is bigger than the in-strength or out-strength

values. Thus, the strength reports that not only the inputs explain the ignition recruitment but also exist a component in the outputs. In summary, the ignition is triggered in the  $s_{max}$ -core, and then the recruitment follows a core-shell organization, rather than a strength-based organization in the human connectome.

## 2. Ignition in cortical activity is tightly linked to the weighted core-shell organization in the human connectome

The core is a mesoscale feature, and its structural relevance in the cortical network has been previously reported (Hagmann et al. 2008; Deco et al. 2017; Kitsak et al. 2010; Betzel, Medaglia, and Bassett 2018). I go one step further and probe that the ignition (i.e., a dynamic feature) is core-shell organized on the human connectome, something that is not well captured even with models that preserve connectivity pattern, degree distribution, the ratio of integration to segregation ratio, or even its weight distribution. Thus, I show how this core-shell organization is a specific feature of the *human connectome* that supports its ignited cortical activity.

### 2.1. The ignition is triggered in the weighted core of the human connectome

I used surrogate models to assess how different network features of the human connectome pattern were involved in the ignition. As a first approach, I built the *unweighted surrogate connectome* (uSCs) models (Figure 20A). The uSCs have homogeneous weights in their connections (equal to the mean value of the human connectome,  $1.332 \times 10^{-2}$ ), and also conserve the overall strength of the human connectome, 15.3. In this way, I could disentangle effects on the network ignition that was genuinely due to the connectivity structure of the human connectome, irrespectively of the influence of the weight of the connections.

A first surrogate connectome is the  $\text{Human}_{\text{hw}}$  that homogenizes the weight distribution of the human connectome preserving its connectivity pattern (Figure 20A, left). Then, I considered an ensemble of unweighted Degree-Preserving Random ( $\text{DPR}_{\text{hw}}$ ) networks, in which, in addition to making all the weights homogeneous (as in  $\text{Human}_{\text{hw}}$ ), connections were randomly rewired between nodes, breaking the connectivity pattern of Human, but still preserving the degree of each cortical region, as a signature of its local organization (Figure 20A, middle) (Maslov and Sneppen 2002). Finally, I generated an ensemble of Small-World ( $\text{SW}_{\text{hw}}$ ) surrogate connectomes optimized to conserve the global small-worldness of the Human as a signature of its global organization (Figure 7A, right) (Watts and Strogatz 1998; Mark D. Humphries and Gurney 2008). The small-worldness is a ratio of network segregation (clustering coefficient) to integration (small characteristic path length), postulated as a relevant structural organization in the efficient flow of activity in the cortex (Watts and Strogatz 1998; M. D. Humphries, Gurney, and Prescott 2006). It is important to note that  $\text{SW}_{\text{hw}}$  ensembles do not conserve the connectivity pattern or even the degree distribution of the human connectome. As the  $\text{DPR}_{\text{hw}}$  and  $\text{SW}_{\text{hw}}$  ensembles are randomly generated, 100 instances of each were used (see materials and methods chapter for details of the builds of the connectomes).

The deterministic simulations of Human,  $\text{Human}_{\text{hw}}$ , 100  $\text{DPR}_{\text{hw}}$  and, 100  $\text{SW}_{\text{hw}}$  ensembles are summarized in Figure 20B and Table 5. Notice that  $\text{DPR}_{\text{hw}}$  and  $\text{SW}_{\text{hw}}$  ensembles show low dispersion in its bifurcation points,  $G$ . and  $G_+$ , despite the differences of each network instance. Considering uSCs, the first important observation is that the bistability range of ignition is not exclusive to the human connectome. However, the human connectome has the lowest excitability threshold for the bifurcation  $G$ . and  $G_+$ . This low excitability threshold can not be replicated using the connectivity pattern ( $\text{Human}_{\text{hw}}$ ), or the local ( $\text{DPR}_{\text{hw}}$ ) or global ( $\text{SW}_{\text{hw}}$ ) organization of the human connectome. This suggests that the heterogeneous weight of

connections play a role in the low excitability threshold for the trigger and collapse of the network ignition of the human connectome.

Second, the disruption of the connectivity pattern of the human connectome ( $\text{Human}_{hw}$ ) but conserving its local organization ( $\text{DPR}_{hw}$ ) produces similar values for  $G_-$  and  $G_+$ . Thus, the degree distribution of the human connectome is enough to reproduce the thresholds for the

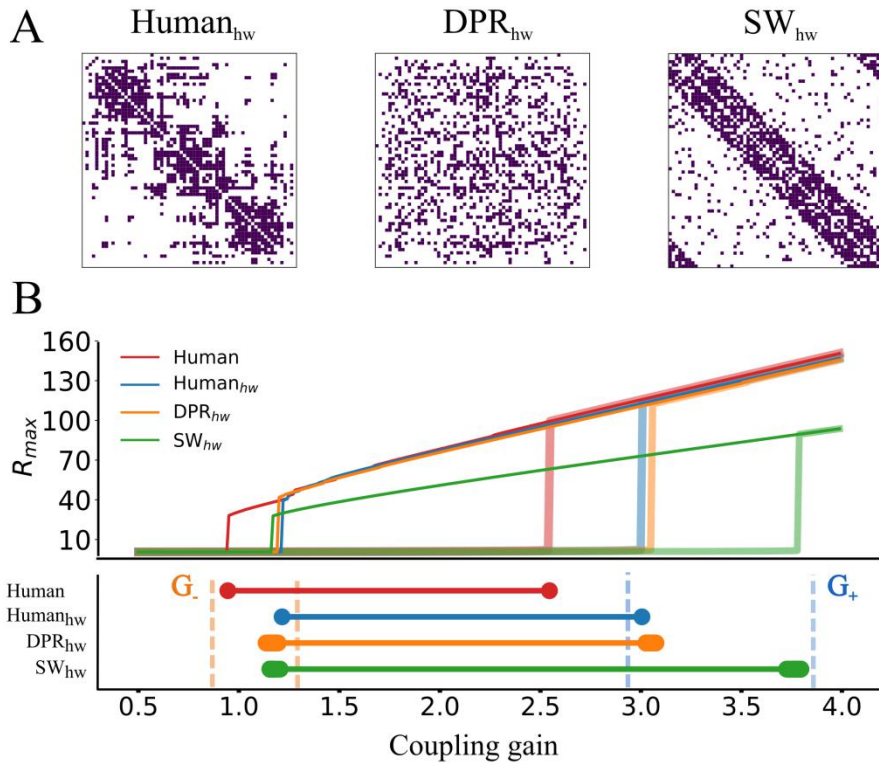


**Figure 20. The human cortical connectome requires a lower coupling gain to display ignition than unweighted surrogate models.** (A) The unweighted surrogate connectomes (uSCs) models, in which the weight value of each connection is set as equal to the mean of the Human ( $1.332 \times 10^{-2}$ ). Left, the  $\text{Human}_{hw}$ . Middle, a representative example of the 100  $\text{DPR}_{hw}$  matrices. Right, a representative example of the 100  $\text{SW}_{hw}$  matrices. (B) Top, the network activity state through the coupling range ( $x$ -axis) for the human connectome and a representative case of each uSCs, using Low and High ICs. The uSCs ensembles present the ignition in the bistability range. Bottom, a summary of the ignition  $G_-$  (left circles) and flaring  $G_+$  (right circles) points in the bistability range of the Human (red),  $\text{Human}_{hw}$  (blue), 100  $\text{DPR}_{hw}$  (orange), and 100  $\text{SW}_{hw}$  (green) ensembles. The *orange dashes* show the range of values for  $G_-$ , whereas the *pale blue dashes* show for  $G_+$ . Notice the small dispersion in the bifurcation values on 100 different  $\text{DPR}_{hw}$  and  $\text{SW}_{hw}$  networks.

**Table 5. The dynamic and structural data of the human and surrogate ensembles.**

Ignition	Human	Human <sub>hw</sub>	DPR <sub>hw</sub>	SW <sub>hw</sub>	Human <sub>rw</sub>	DPR <sub>rw</sub>	SW <sub>rw</sub>
<b>G.</b>	0.945	1.212	1.193	1.158	1.32 (± 0.095)	1.369 (± 0.107)	1.501 (± 0.083)
<b>G+</b>	2.525	3.002	3.052	3.737	2.606 (± 0.154)	2.666 (± 0.228)	2.976 (± 0.148)
<b>N.</b>	11 (~17%)	32 (~48.5%)	45.8 (~69.4%)	63.1 (~95.6%)	23.9 (~36.2%)	30.7 (~46.5%)	26.8 (~42.1%)
<b>k<sub>max</sub>-core nodes</b>	53 (~80.3%)	53 (~80.3%)	49.7 (~75.3%)	59 (~89.4%)	-	-	-
<b>s<sub>max</sub>-core nodes</b>	11 (~17%)	-	-	-	22.5 (~34.1%)	27.9 (~42.3%)	31 (~46.9%)

bistability range produced by its connectivity pattern (Figure 20B, bottom). In other words, the specific connectivity pattern by itself (Human<sub>hw</sub>) is irrelevant for the threshold of the G. and G+ and can be captured by the weighted local level of structural organization.

Third, the SW<sub>hw</sub> networks have the most extensive bistability range, with a similar result for the ignition point G. with the other uSCs but the largest flaring point G+ among all the ensembles (Figure 20B, green). On the one hand, the threshold for the ignition point is not specified by the unique connectivity pattern of the human connectome (Human<sub>hw</sub>) but instead can be achieved with a local (DPR<sub>hw</sub>) or global (SW<sub>hw</sub>) level of organization. On the other hand, the larger

threshold for the flaring point of the  $SW_{hw}$  ensemble shows that local rather than global organization captures better the threshold for the collapse of the network ignition of the human connectome. A possible explanation is based on the fact that the  $SW_{hw}$  ensemble has the narrowest degree distribution among the uSCs, with comparatively fewer connections in their high degree nodes. In this scenario, the nodes with more connections reduce the threshold for the flaring point in  $Human_{hw}$  and  $DPR_{hw}$  networks (see below, Figure 21). Therefore, local rather than global features -degree sequence rather than the small-worldness- account for the network ignition and bistability range that emerges from the connectivity pattern of the human connectome.

**The number of ignited nodes in the uSCs.** Figure 21A shows, for each of the uSCs, the number of ignited nodes,  $N_{ignited}$ , in a range of coupling gain and High ICs. In the case of  $DPR_{hw}$  and  $SW_{hw}$  ensembles, only one representative example is shown. The first jump reveals how many nodes have a high activity right after the ignition point  $G$ , i.e., how many nodes participate in the trigger of network ignition. Figure 21A reveals that the Human not only has the trigger for ignition at the lowest  $G$  value, but it also depends on the smallest subset of nodes ( $n = 11$ ) in the earlier ignition of the nodes. This is not true for the uSCs, in which a large subset of nodes ignites at  $G$ ;  $Human_{hw}$  ( $n = 32$ ),

$DPR_{hw}$  (mean  $n = 45.83 \pm 2.46$ ), and  $SW_{hw}$  (mean  $n = 63.12 \pm 1.85$ ). Additionally,  $N_{ignited}$  increases smoothly in the human connectome and sharply in the case of the uSCs, with the extreme case of the  $SW_{hw}$  in which almost all the nodes ignite at  $G$ . (Figure 8A, green line). Thus, at  $G$ , Human presents a larger amount of not ignited nodes, compared to the uSCs.

**The local and mesoscale organization in the uSCs.** Figure 21B shows the degree distribution of the human connectome and the uSCs. The Human (red) shows a broad degree

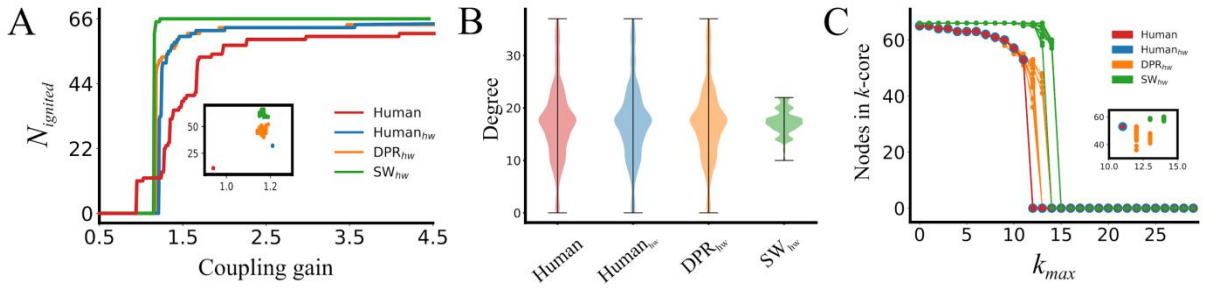


**Figure 21. The ignited nodes and the unweighted network analysis. (A)** The number of ignited nodes,  $N_{\text{ignited}}$  (threshold  $R_i > 5$ ), as a function of coupling gain  $G$  ( $0.5 \leq G < 4$ , with steps of  $G=0.001$ ) in Human (red), Human<sub>hw</sub> (blue), and one representative example of DPR<sub>hw</sub> (orange), and SW<sub>hw</sub> (green) ensembles. The inset shows the  $N_{\text{ignited}}$  in the bifurcation  $G$  for Human and all the uSCs. **(B)** The degree distribution of the Human and the uSCs. The degree distribution of the Human, Human<sub>hw</sub>, and DPR<sub>hw</sub> are equal by construction. The SW<sub>hw</sub> have the narrowest degree distribution, without sparsely and highly connected nodes. **(C)** The  $k$ -core decomposition of Human, Human<sub>hw</sub>, DPR<sub>hw</sub>, and SW<sub>hw</sub>. The  $y$ -axis shows the number of nodes in the shell, whereas the  $x$ -axis shows the minimum  $k_{\text{max}}$  inside that shell. The inset shows the largest  $k_{\text{max}}$ ,  $k_{\text{max}}$ -core, for Human and all the uSCs. The Human has the lowest  $k_{\text{max}}$  (11) and an intermediary  $k_{\text{max}}$ -core value (53 nodes,  $\sim 80.3\%$  of network nodes).

distribution (mean  $k_i = 17.39 \pm 7.42$ ); the Human<sub>hw</sub> (orange) and DPR<sub>hw</sub> (orange) are identical to Human by design. The SW<sub>hw</sub> ensemble (green) has the same mean  $k_i$  of Human, with a comparatively narrow dispersion (mean  $k_i = 17.39 \pm 2.07$ ). Notice that the SW<sub>hw</sub> ensemble presents a lower degree in the highly connected nodes, and as it argued before, this could explain their largest threshold for the flaring point among the uSCs (Figure 21B, green).

Figure 21C shows the  $k$ -core decomposition of the Human (red line) and uSCs. The  $k$ -core decomposition is an unweighted network analysis (using degree instead of strength) to unveil the core-shell organization of the network. Again, Human<sub>hw</sub> (blue line) is identical to Human because they share the connectivity pattern. The value of  $k_{\text{max}}$  is smaller in the Human ( $k_{\text{max}}=11$ ), in comparison with DPR<sub>hw</sub> (mean  $k_{\text{max}} = 12.08 \pm 0.28$ ) or SW<sub>hw</sub> (mean  $k_{\text{max}} = 13.95 \pm 0.22$ ) ensembles. The inset of Figure 21C portrays  $k_{\text{max}}$  values for individual instances of the different surrogate ensembles showing that the  $k_{\text{max}}$  of Human is smaller than the  $k_{\text{max}}$  of any instances of DPR<sub>hw</sub> or SW<sub>hw</sub>. The Human has the lowest number of connections in the core, forming weaker

cores. Also, it is shown that it is easy to form an unweighted core using the local or global features of the human connectome. Furthermore, the  $k_{max}$ -core of the Human includes a larger number of nodes ( $n = 53$ ) with respect to the  $k_{max}$ -core of the  $DPR_{hw}$  ensemble (mean  $n = 49.73 \pm 3.38$ ), but still smaller than the  $SW_{hw}$  networks (mean  $n = 59.0 \pm 0.77$ ).

**Ignition core in uSCs.** Figure 22A shows, at the ignition point  $G_-$ , the fraction of nodes with ignited or baseline activity and whether the nodes belong or not to the  $k_{max}$ -core. The  $k_{max}$ -core of Human catches the ignited subset (red bar) at ignition point  $G_-$ , but also many of its nodes had baseline low activity (green bar). Also, the ignited nodes are a small proportion of the total  $k_{max}$ -core nodes (11/53 nodes). In the bifurcation  $G_-$ , the uSCs present a higher number of nodes ignited and in the  $k_{max}$ -core than Human. Even further, the  $SW_{hw}$  ensemble recruits almost

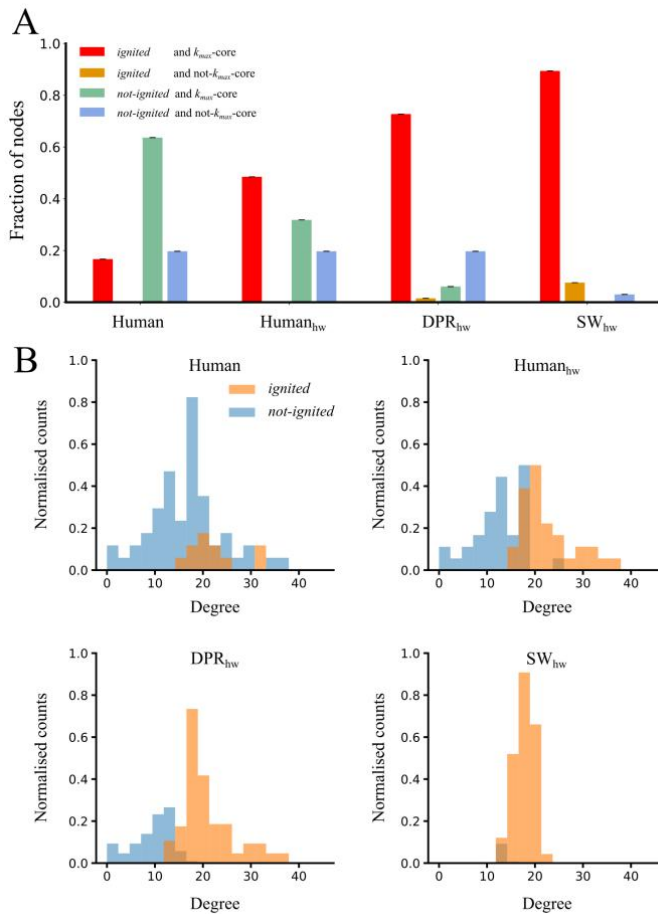


**Figure 22. The ignited cortical regions are loosely related to the unweighted core or degree of the human connectome at the ignition point  $G_-$ .** (A) The bar plot shows the fraction of nodes that are *ignited* (red, orange) or *not-ignited* (green, blue) at  $G_-$ , and that belong to  $k_{max}$ -core (red, green) or not (orange, blue). Note that the  $k_{max}$ -core match with all the *ignited* cortical regions in the Human, but also with a large number of them with *not-ignited* baseline activity. (B) The degree distribution of *ignited* (orange) and *not-ignited* (blue) nodes at the ignition point  $G_-$ , for Human and the uSCs.

all the  $k_{max}$ -core nodes. Also, the  $DPR_{hw}$  and  $SW_{hw}$  ensembles show ignition in the nodes that do not belong to the  $k_{max}$ -core (orange bars). Thus, the unweighted core is not a good predictor of the ignited nodes of Human because a large fraction of the nodes is not ignited in the  $k_{max}$ -core.

Figure 22B shows the degree distribution of the *ignited* (orange) and *not-ignited* (pale blue) nodes of the Human and uSCs ensembles. In the case of the unweighted local features of the network, the high degree nodes of uSCs capture the ignited nodes at ignition point G. The  $Human_{hw}$  shows several nodes with medium degree values, that can be at high or low activity state (Figure 22B, middle-left).  $DPR_{hw}$  ensemble shows ignition in the high degree nodes (Figure 22B, middle-right).  $SW_{hw}$  ensemble shows ignition in almost all the nodes (Figure 22B, right). However, even if the ignited nodes at G. in the Human have a degree slightly higher than the mean, there are several nodes with an even higher degree than stay not-ignited at G. (Figure 22B, left). Thus, the degree poorly explains the ignited cortical regions of the human connectome at G..

**Ignition sequence and core hierarchy in the uSCs.** The relationship between the ignition sequence and the unweighted network organization was evaluated as with the human connectome. Figure 23 shows the relationship between ignition and the sorted coupling gain, for Human,  $Human_{hw}$ , and representative cases of  $DPR_{hw}$  and  $SW_{hw}$  ensembles (Table 6 shows the  $\rho^2$ ). Nodes are ordered from bottom to top according to the ignition recruitment, and the color code is either the  $k_{max}$  (Figure 23A-D) or degree (Figure 23F-I) value of each ignited node. Figure 23E shows the explained variance of the Spearman rank correlation,  $\rho^2$ , between coupling gain after the ignition turns up and the  $k_{max}$  for Human (**0.210**, percentile (2.5, 97.5) = (0.194, 0.226)),  $Human_{hw}$  (**0.550**, percentile (2.5, 97.5) = (0.535, 0.565)),  $DPR_{hw}$  (**0.887**, (2.5, 97.5) = (0.874, 0.900)), and  $SW_{hw}$  (**0.700**, (2.5, 97.5) = (0.671, 0.727)). The explained variance between node ignition and  $k_{max}$  is lower for Human than for the  $Human_{hw}$ ,  $DPR_{hw}$ , or even the  $SW_{hw}$

ensemble. The lowest  $\rho^2$  values of the Human can be explained based on the fact of a large number of nodes that belong to the  $k_{max}$ -core and not-ignite (Figure 22A). The ignition recruitment of the 13 regions that do not belong to the  $k_{max}$ -core is conflated with the other 42

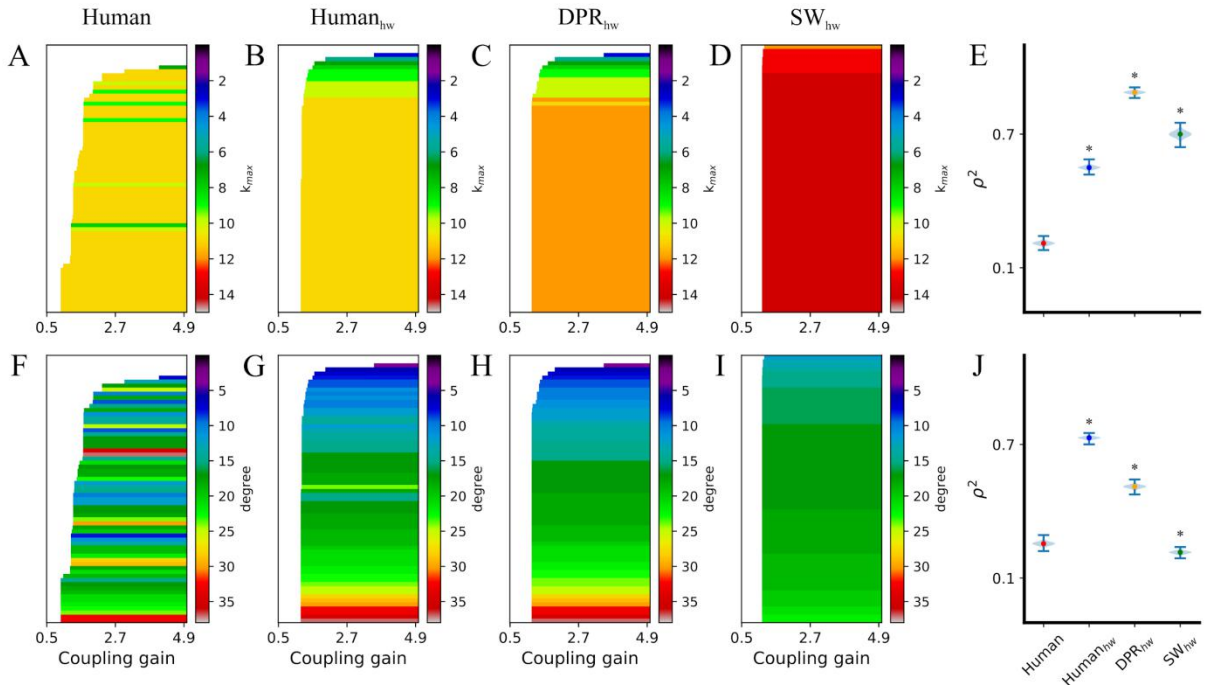


**Figure 23. The ignition in the human connectome was not related to the unweighted core organization or degree. (A-D)** Cortical regions in the  $y$ -axis are sorted according to the coupling gain  $G$  ( $x$ -axis) value at which they first ignite. Colour code shows the  $k_{max}$  for each of the ignited regions of (A) Human, (B) Human<sub>hw</sub>, and one representative example of (C) DPR<sub>hw</sub>, and (D) SW<sub>hw</sub> ensembles. (E) Spearman rank correlation squared ( $\rho^2$ , explained variance) between ignition recruitment and the  $k_{max}$  for Human (**0.210**, percentile (2.5, 97.5) = (0.194, 0.226)), Human<sub>hw</sub> (**0.550**, percentile (2.5, 97.5) = (0.535, 0.565)), DPR<sub>hw</sub> (**0.887**, percentile (2.5, 97.5) = (0.874, 0.900)), and SW<sub>hw</sub> (**0.700**, percentile (2.5, 97.5) = (0.671, 0.727)). (F-I) Similarly, color code shows the degree for each of the ignited cortical regions of (F) Human, (G) Human<sub>hw</sub>, and one representative example of (H) DPR<sub>hw</sub>, and (I) SW<sub>hw</sub> ensembles. (J) Spearman rank correlation squared ( $\rho^2$ , explained variance) between ignition recruitment and the degree for Human (**0.255**, percentile (2.5, 97.5) = (0.238, 0.271)), Human<sub>hw</sub> (**0.730**, percentile (2.5, 97.5) = (0.718, 0.742)), DPR<sub>hw</sub> (**0.511**, percentile (2.5, 97.5) = (0.496, 0.525)), and SW<sub>hw</sub> (**0.216**, percentile (2.5, 97.5) = (0.202, 0.229)). The \* indicates a significant difference between the  $\rho^2$  of Human and uSCs. The significance of  $\rho^2$  was evaluated using 10,000 replicas from bootstrap resampling (violin plots).

regions that belong to it, but are not ignited at the G-. The green stripes of Figure 23A (low  $k_{max}$  nodes) are a good example of this.

The explained variance of ignition recruitment by the  $k_{max}$  is the highest in the  $DPR_{hw}$  ensemble, and also is high in the  $Human_{hw}$  and  $SW_{hw}$ , suggesting as a first glance that connectivity pattern, local, or global organization is enough to capture this relationship in unweighted network analysis. However, the large number of nodes that ignite at G. are part of the  $k_{max}$ -core (Figure 22A), and that is a significant bias in the value of  $\rho^2$ . Thus, that bias in the value of  $\rho^2$  is inherent to the uSCs ensembles. Nodes that are ignited through the coupling gain have less relevance in the final value of  $\rho^2$ , as in the case of  $Human_{hw}$  and  $DPR_{hw}$  ensembles. Compared to the  $DPR_{hw}$  ensemble, the  $Human_{hw}$  has a smaller number of nodes that ignite at G-, and also lower  $\rho^2$ . Thus, the explained variance by the connectivity pattern of  $Human_{hw}$  is not accountable, taking only the local organization of the  $DPR_{hw}$  ensemble. The  $SW_{hw}$  ensemble is the most prominent exponent of the effect of the large ignited subset at G+ because those networks also show high relation between  $k_{max}$  and ignition recruitment. These high values of  $\rho^2$  in the  $SW_{hw}$  ensemble is explained because almost all nodes of the network ignite, without graded control. I call this type of ignition recruitment in the network biphasic because all nodes are turned on or off. Figure 23J shows the variance of the Spearman rank correlation,  $\rho^2$ , between ignition recruitment and the degree for Human (**0.255**, percentile (2.5, 97.5) = (0.238, 0.271)),  $Human_{hw}$  (**0.730**, percentile (2.5, 97.5) = (0.718, 0.742)),  $DPR_{hw}$  (**0.511**, (2.5, 97.5) = (0.496, 0.525)), and  $SW_{hw}$  (**0.216**, (2.5, 97.5) = (0.202, 0.229)). The explained variance of ignition recruitment by the degree of Human is slightly higher to the observed with  $k_{max}$ . Also, the  $Human_{hw}$  increase the explained variance of ignition recruitment using the degree instead of  $k_{max}$ . Contrary,  $DPR_{hw}$  and  $SW_{hw}$  ensembles decrease the explained variance of the ignition when the degree, instead of  $k_{max}$ , is considered. The considerable decrease in the explained variance

**Table 6. The explained variance of the Spearman rank correlation between ignition and structural measures for *Human* and uSCs.** The explained variance of the Spearman rank correlation ( $\rho^2$ ) between ignition and either  $k_{max}$ , or degree in Human,  $Human_{hw}$ ,  $DPR_{hw}$ , and  $SW_{hw}$ . The percentiles to evaluate the significance of  $\rho^2$  was performed using 10.000 replicas from bootstrap resampling.

<b>Ignition</b>	<b>Human</b> $\rho^2$ , percentile (2.5, 97.5)	<b>Human<sub>hw</sub></b> $\rho^2$ , percentile (2.5, 97.5)	<b>DPR<sub>hw</sub></b> $\rho^2$ , percentile (2.5, 97.5)	<b>SW<sub>hw</sub></b> $\rho^2$ , percentile (2.5, 97.5)
<i>k<sub>max</sub></i>	<b>0.210</b> , (0.194, 0.226)	<b>0.550</b> , (0.535, 0.565)	<b>0.887</b> , (0.874, 0.900)	<b>0.700</b> , (0.671, 0.727)
<b>degree</b>	<b>0.255</b> , (0.238, 0.271)	<b>0.730</b> , (0.718, 0.742)	<b>0.511</b> , (0.496, 0.525)	<b>0.216</b> , (0.202, 0.229)

of ignition recruitment given by the degree in the  $SW_{hw}$  ensemble could be explained by its biphasic network ignition, in which almost all the  $k_{max}$ -core nodes ignite in the ignition point  $G$ . Thus, there are fewer nodes to correlate with  $k_{max}$  through ignition recruitment.

**The correlation between unweighted network features and ignition is lower in the human connectome than when the weighted characteristics are considered. The weights of the human connectome confer lower thresholds for the trigger and collapse of the bistability range. Indeed, ignition core and recruitment is related to the weighted features of the human connectome. In the next section is explored the relevance of the weights of the human connectome in the ignition.**

## 2.2. The ignition recruitment is organized by the weighted core of the human connectome

To disentangle if the heterogeneity can explain the ignition features of the human connectome in its connection weights, I considered the weighted surrogate connectomes (wSCs).

The wSCs preserve the weight distribution of the human connectome but break its specific order (i.e., change the strength distribution, see materials and methods for details). There are 60  $\text{Human}_{\text{rw}}$  (Figure 24A, left), 60  $\text{DPR}_{\text{rw}}$  (Figure 24A, middle), and 60  $\text{SW}_{\text{rw}}$  (Figure 24A, right) ensembles.

The deterministic simulations of the Human, 60  $\text{Human}_{\text{rw}}$ , 60  $\text{DPR}_{\text{rw}}$ , and 60  $\text{SW}_{\text{rw}}$  are summarized in Figure 24B and Table 5. As a first observation, all the wSCs present two bifurcation points in a range of coupling parameter  $G$ , reaffirming that the bistability range is not exclusive to the human connectome. For wSCs, the dispersion of  $G$  and  $G_+$  values through different random instances from the same ensemble was more extensive than for uSCs. Given that all the instances had precisely the same set of connection weights, but randomly assigned to different links, this large dispersion already suggests that specific weight-to-connectivity arrangements can influence how low or high critical points are.

Also, introducing heterogeneous weights generally decreased the threshold for the flaring point  $G_+$  of wSCs, compared to their uSCs counterparts. Indeed, the flaring point for the Human reference connectome falls now well within the fluctuation range of flaring points for  $\text{Human}_{\text{rw}}$  and  $\text{DPR}_{\text{rw}}$  ensembles. This overlap emphasizes the role of weight diversity, suggesting it as an explanation for the reduction in the threshold in the flaring point  $G_+$  of the wSCs. The simulations of  $\text{SW}_{\text{rw}}$  ensembles show a decrease in the bifurcation  $G_+$  compared to  $\text{SW}_{\text{hw}}$  ensembles. Thus, the abnormally large threshold for the flaring point in the  $\text{SW}_{\text{hw}}$  ensembles is compensated by the heterogeneity in the connection's weight (Figures 20B and 24B, green). This suggests that the flaring point  $G_+$  value observed for the Human connectome can be accounted for by its degree and weight distributions (shared with the  $\text{Human}_{\text{rw}}$  and  $\text{DPR}_{\text{rw}}$  ensembles, but not with the  $\text{SW}_{\text{rw}}$  ensemble), rather than by its small-worldness (shared with the  $\text{SW}_{\text{rw}}$  ensemble, but not with the  $\text{Human}_{\text{rw}}$  and  $\text{DPR}_{\text{rw}}$  ensembles). However, the human connectome has the lowest threshold for the ignition point  $G$  compared to wSCs, similarly to the

obtained with respect of the uSCs. This indicates that both the heterogeneity in the weights (not found in  $\text{Human}_{\text{rw}}$ ) and the specific pattern in which these weights are distributed (disrupted in  $\text{Human}_{\text{rw}}$ ) are essential for maintaining a low ignition point  $G$ . (Figure 24B). This characteristic of the Human connectome is thus exceptional, in the sense that it is unlikely to arise by chance

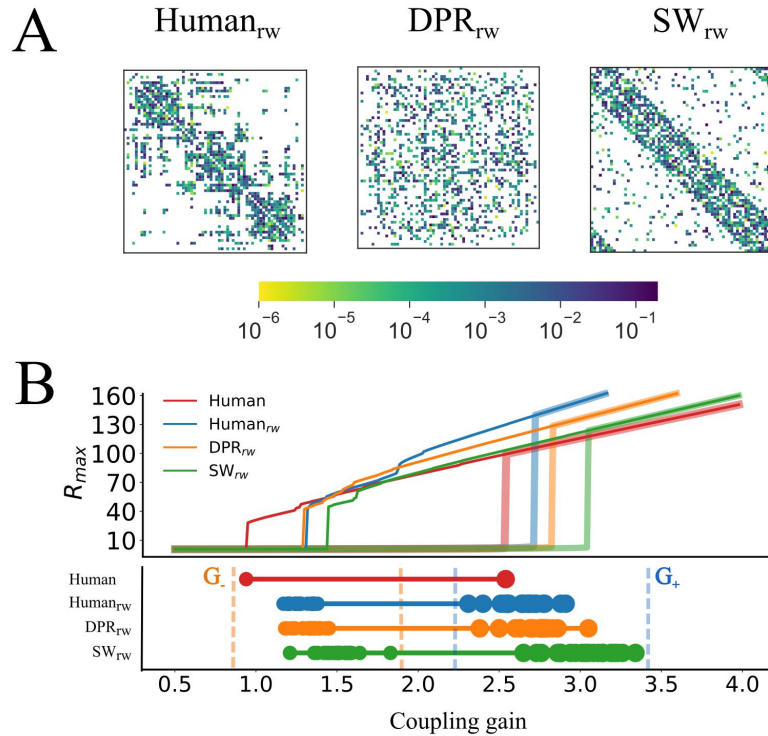


**Figure 24. The human cortical connectome requires a lower coupling gain to display ignition than weighted surrogate models.** (A) One example of the weighted surrogate connectomes (wSCs) matrices. The color bar shows the connection weights in a log-scale. Left, the  $\text{Human}_{\text{rw}}$  matrix, which conserves the connectivity pattern and the weight distribution of Human but disrupts its specific organization. Middle, the  $\text{DPR}_{\text{rw}}$  matrix, which conserves specific degree distribution and weight distribution of the Human connectome but disrupts their local organization. Right, the  $\text{SW}_{\text{rw}}$  matrix, which generates a similar global organization of the Human and preserves its weight distribution. (B) Top, the network activity state through the coupling range ( $x$ -axis) for the human connectome and a representative case of each wSCs, using Low and High ICs. The wSCs ensembles present network ignition in the bistability range. Bottom, a summary of the ignition  $G$ . (left circles) and flaring  $G_+$  (right circles) points in the bistability range of the Human (red),  $\text{Human}_{\text{rw}}$  (blue), 60  $\text{DPR}_{\text{rw}}$  (orange), and 60  $\text{SW}_{\text{rw}}$  (green) ensembles. The orange dashes show the range of values for  $G_-$ , whereas the pale blue dashes show for  $G_+$ . Notice the wider dispersion of the bifurcation points in wSCs than uSCs (Figure 20B).

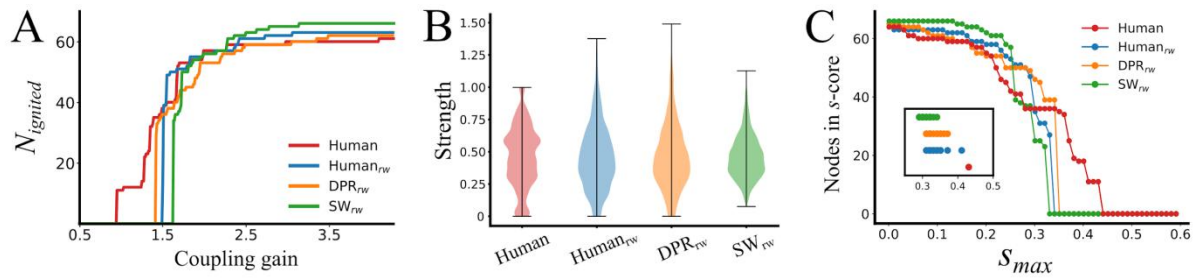


**Figure 25. The ignited nodes and the weighted network analysis.** (A) The number of ignited nodes,  $N_{\text{ignited}}$  (threshold  $R_i > 5$ ), as a function of coupling gain  $G$  in Human (red), and one representative example of Human<sub>rw</sub> (blue), DPR<sub>rw</sub> (orange), and SW<sub>rw</sub> (green). (B) The strength distribution of the Human and the wSCs. The SW<sub>hw</sub> has similar strength distribution with the other wSCs, opposite to the case of the uSCs (degree distribution, see Figure 21B). (C) The  $s$ -core decomposition of Human (red), Human<sub>rw</sub> (blue), DPR<sub>rw</sub> (orange), and SW<sub>rw</sub> (green), using steps of  $s_{\text{max}}=0.01$ . The  $y$ -axis shows the number of nodes in the shell, whereas the  $x$ -axis shows the  $s_{\text{max}}$  of that shell. Only one example for each type of wSCs is shown in the main plot. The inset shows the  $s_{\text{max}}$  for all the networks used. The Human has the largest  $s_{\text{max}}$  (0.431) in a small  $s_{\text{max}}$ -core (11 regions,  $\sim 16.7\%$  of network nodes).

in the organization of the studied surrogate ensembles.

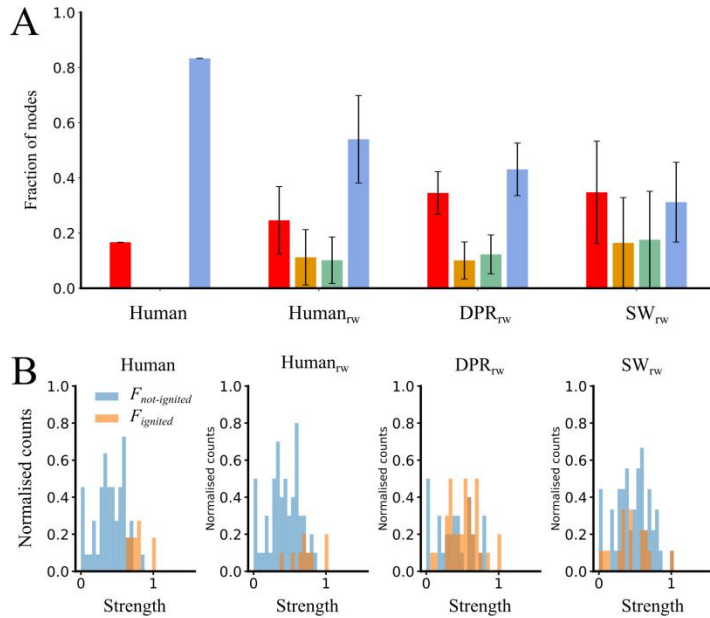
**The number of ignited nodes in the wSCs.** Figure 25A shows the number of ignited nodes versus  $G$  for Human and one representative case of Human<sub>rw</sub>, DPR<sub>rw</sub>, and SW<sub>rw</sub>. The  $N_{\text{ignited}}$  at  $G$  for Human ( $n = 11$ ), Human<sub>rw</sub> (mean  $n = 23.88 \pm 10.02$ ), DPR<sub>rw</sub> (mean  $n = 30.67 \pm 8.77$ ), and SW<sub>rw</sub> (mean  $n = 26.78 \pm 14.29$ ) ensembles. The  $N_{\text{ignited}}$  at the ignition point is reduced in the wSCs ensembles compared to the uSCs ones but still is larger than the human connectome subset. Also, ignited nodes increase more smoothly as a function of the coupling gain in wSCs than in the case of uSCs.

**Network properties of the wSCs.** Figure 25B shows the strength distribution of the Human connectome (mean  $s_i = 0.464 \pm 0.237$ ), Human<sub>rw</sub> (mean  $s_i = 0.464 \pm 0.254$ ), DPR<sub>rw</sub> (mean  $s_i = 0.464 \pm 0.256$ ) and SW<sub>rw</sub> (mean  $s_i = 0.464 \pm 0.175$ ) ensembles. The random assignation of the weights does not change the strength distribution of the wSCs dramatically with respect to the Human, as shown in Figure 25B. All the strength distributions are highly

overlapped. Indeed, the strength distribution as a weighted network feature makes the  $SW_{rw}$  ensemble more similar to the human connectome than the weighted features (degree distribution). This could be related to their decrease in the threshold values for the flaring point  $G_+$  (Figure 24B, green).

Figure 25C shows the  $s$ -core decomposition of the Human and wSCs, which reveals the weighted core-shell organization in the networks. Figure 25C shows the  $s$ -core decomposition of the Human and wSCs. The  $s_{max}$  within the nodes of the  $s_{max}$ -core is the largest in the Human ( $s_{max} = 0.431$ ), in comparison with Human<sub>rw</sub> (mean  $s_{max} = 0.339 \pm 0.020$ ), DPR<sub>rw</sub> (mean  $s_{max} = 0.329 \pm 0.016$ ) or SW<sub>rw</sub> (mean  $s_{max} = 0.308 \pm 0.013$ ). The inset of Figure 25C portrays  $s_{max}$  values of the core for individual instances of the different surrogate ensembles showing that the  $s_{max}$  is larger in Human than in any of the wSCs. Furthermore, the  $s_{max}$ -core of the Human includes the compact  $s_{max}$ -core ( $n = 11$ ) compared to the Human<sub>rw</sub> (mean  $n = 22.53 \pm 9.21$ ), DPR<sub>rw</sub> (mean  $n = 27.95 \pm 9.29$ ), and SW<sub>hw</sub> (mean  $n = 30.97 \pm 15.65$ ) ensembles. Notice that the  $N_{\text{ignited}}$  and the number of nodes in the  $s_{max}$ -core decrease in the wSCs compared to the uSCs ensembles (see Table 5).

**Ignition core in the wSCs.** Figure 26A shows the fraction of nodes with ignited or baseline activity and whether the nodes belong or not to the  $s_{max}$ -core at the ignition point  $G_+$ . Previously, I have shown a one-to-one correspondence of the ignited regions and the  $s_{max}$ -core after the ignition point  $G_+$ . This one-to-one correspondence is lost whenever the strengths are randomized, even if the connectivity pattern is maintained, as in Human<sub>rw</sub>. Thus, the human connectome has a unique weighted pattern that is related to the low threshold value for the ignition at  $G_+$ , and the specific connectivity pattern does not explain that. Additionally, at  $G_+$ , all the wSCs show ignited nodes that do not belong to  $s_{max}$ -core as well as nodes that are belonging to this core and are not-ignited (orange and green bars, respectively, in Figure 26A).



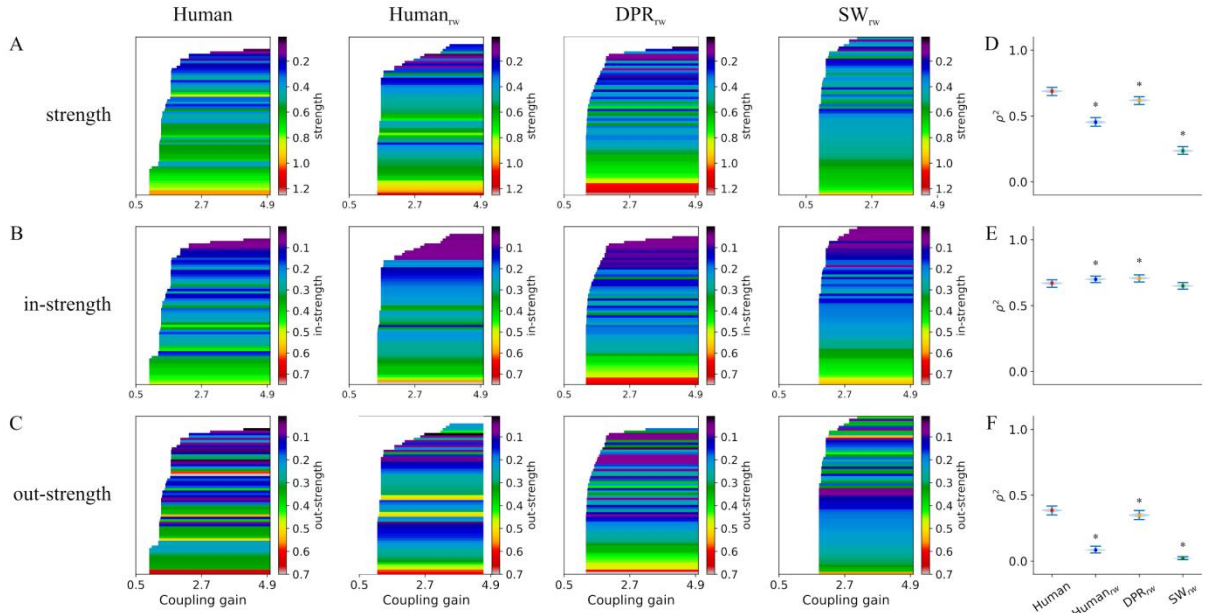
**Figure 26. Ignited cortical regions match perfectly the weighted core of the human connectome at the ignition point G.** (A) The bar plot shows the fraction of nodes that are *ignited* (red, orange) or *not-ignited* (green, blue) at the G. bifurcation, and that belong to  $S_{max}$ -core (red, green) or not (orange, blue). (B) The strength distribution of *ignited* (orange) and *not-ignited* (blue) nodes at the ignition point G-, for Human and the wSCs.

Figure 26B shows the strength distribution of the *ignited* (orange) and *not-ignited* (pale blue) nodes of the Human and wSCs ensembles. The nodes with high strength of the Human show a higher overlap with the ignited subset, compared to the degree (compare Figures 22B and 26B). The strength is a better predictor of ignition in cortical regions of Human than the degree. However, the strength shows nodes with high values and not-ignited in the Human and also in the wSCs. Thus, strength does not capture all the features that define the lowest threshold for the ignition point in the human connectome.

**Ignition sequence and core hierarchy in the wSCs.** Figure 27A-C shows the relationship between the ignition recruitment and the weighted local organization (i.e., strength, in-strength, and out-strength), for Human (left), and a representative case of Human<sub>rw</sub> (middle-left), DPR<sub>rw</sub> (middle-right) and SW<sub>rw</sub> (right) ensembles. Nodes are sorted from bottom to top according to the

onset of ignition, and the color code is either the strength (Figure 27A), in-strength (Figure 27B), and out-strength (Figure 27C) value of each ignited node.

Figure 27D-F shows the explained variance of Spearman rank correlation ( $\rho^2$ ) between ignition recruitment and the strength (Figure 27D), in-strength (Figure 27E), and out-strength (Figure



**Figure 27. The ignition in the human connectome is related to the weight of inputs more than outputs of the local organization.** (A-C) Cortical regions in the  $y$ -axis are sorted according to the coupling gain  $G$  ( $x$ -axis) value at which they first ignite. Colour code shows the (A) strength, (B) in-strength, and (C) out-strength for each of the ignited nodes of Human (left column), and one representative example of Human<sub>hw</sub> (middle-left column), DPR<sub>rw</sub> (middle-right column), and SW<sub>rw</sub> (right column) ensembles. (D) Spearman rank correlation squared ( $\rho^2$ , explained variance) between ignition recruitment and the strength of Human (**0.687**, percentile (2.5, 97.5) = (0.672, 0.702)), Human<sub>rw</sub> (**0.453**, percentile (2.5, 97.5) = (0.435, 0.469)), DPR<sub>rw</sub> (**0.620**, percentile (2.5, 97.5) = (0.606, 0.633)), and SW<sub>rw</sub> (**0.235**, percentile (2.5, 97.5) = (0.221, 0.250)). (E) Spearman rank correlation squared ( $\rho^2$ , explained variance) between ignition recruitment and the in-strength for Human (**0.671** percentile (2.5, 97.5) = (0.655, 0.684)), Human<sub>rw</sub> (**0.700**, percentile (2.5, 97.5) = (0.687, 0.713)), DPR<sub>rw</sub> (**0.709**, percentile (2.5, 97.5) = (0.695, 0.721)), and SW<sub>rw</sub> (**0.650**, percentile (2.5, 97.5) = (0.636, 0.662)). (F) Spearman rank correlation squared ( $\rho^2$ , explained variance) between ignition recruitment and the out-strength for Human (**0.386** percentile (2.5, 97.5) = (0.369, 0.402)), Human<sub>rw</sub> (**0.084**, percentile (2.5, 97.5) = (0.073, 0.096)), DPR<sub>rw</sub> (**0.348**, percentile (2.5, 97.5) = (0.331, 0.365)), and SW<sub>rw</sub> (**0.021**, percentile (2.5, 97.5) = (0.027, 0.015)). The \* indicates a significant difference between the  $\rho^2$  of Human and wSCs. The significance of  $\rho^2$  was evaluated using 10.000 replicas from bootstrap resampling (violin plots).

27F) for Human, Human<sub>rw</sub>, DPR<sub>rw</sub>, and SW<sub>rw</sub> ensembles. Also, in the human connectome, the explained variance of ignition recruitment by the strength is larger than for the in-strength or out-strength of each cortical region. However, that is not true in the wSCs because ignition recruitment has a higher  $\rho^2$  for the in-strength than strength or even out-strength. This result of the wSCs emphasizes the importance of the incoming connections of the nodes for ignition recruitment in the local organization. By extension, all of the wSCs ensembles show the worst fit with the ignition recruitment when the out-strength was considered. Indeed, human and wSCs ensembles show closer values for the  $\rho^2$  value when in-strength was considered.

The strength shows an inferior performance in the fit of the  $\rho^2$  than in-strength in the wSCs because the low performance of the out-strength draws it. Thus, the in-strength predicts better the fit with the ignition recruitment among the weighted local organization of the wSCs. However, their performance is lesser than the obtained with the  $s_{max}$  in the case of the human connectome.

Figure 28A-C shows the relationship between the trigger of node ignition and the weighted core organization (i.e.,  $s_{max}$ , in- $s_{max}$ , and out- $s_{max}$ ), for Human (left), and a representative case of Human<sub>rw</sub> (middle-left), DPR<sub>rw</sub> (middle-right) and SW<sub>rw</sub> (right) ensembles. Nodes are sorted from bottom to top according to the ignition sequence, and the color code is either the  $s_{max}$  (Figure 28A), in- $s_{max}$  (Figure 28B), and out- $s_{max}$  (Figure 28C) value of each ignited node.

Figure 28E-F shows the explained variance of Spearman rank correlation ( $\rho^2$ ) between ignition recruitment and the  $s_{max}$  (Figure 28D), in- $s_{max}$ (Figure 28E), and out- $s_{max}$  (Figure 28F; details in Table 7) for Human, Human<sub>rw</sub>, DPR<sub>rw</sub>, and SW<sub>rw</sub> ensembles. Human shows the highest explained variance of ignition recruitment by the  $s_{max}$ , in- $s_{max}$ , and out- $s_{max}$ , and that is higher than in any of the wSCs. The best fit of ignition recruitment is given by the in- $s_{max}$  of Human and

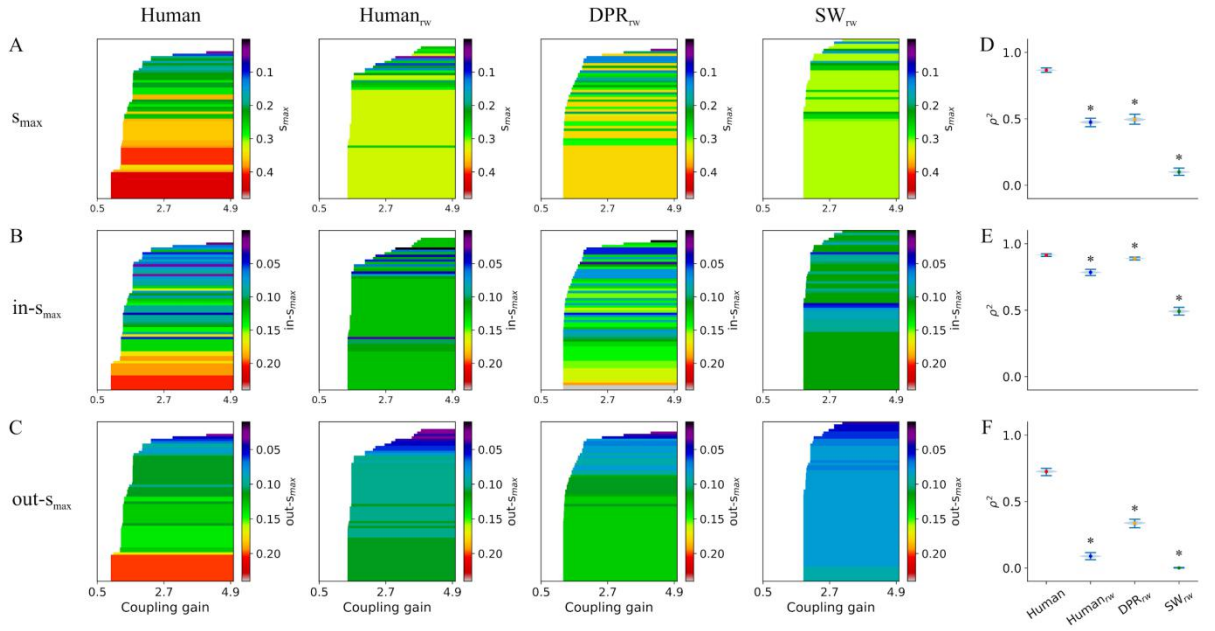


**Figure 28. The ignition in the human connectome is tightly related to the core-shell organization.** (A-C) The cortical regions in the  $y$ -axis are sorted according to the coupling gain  $G$  ( $x$ -axis) value at which they first ignite. Color code shows the (A)  $s_{max}$ , (B)  $in-s_{max}$ , and (C)  $out-s_{max}$  value of each of the ignited nodes of Human (left column), and one representative example of  $Human_{rw}$  (middle-left column),  $DPR_{rw}$  (middle-right column), and  $SW_{rw}$  (right column) ensembles. (D) Spearman rank correlation squared ( $\rho^2$ , explained variance) between ignition recruitment and the  $s_{max}$  Human (**0.867**, percentile (2.5, 97.5) = (0.858, 0.874)),  $Human_{rw}$  (**0.474**, percentile (2.5, 97.5) = (0.459, 0.490)),  $DPR_{rw}$  (**0.495**, percentile (2.5, 97.5) = (0.477, 0.512)), and  $SW_{rw}$  (**0.100**, percentile (2.5, 97.5) = (0.088, 0.112)). (E) Spearman rank correlation squared ( $\rho^2$ , explained variance) between ignition recruitment and the  $in-s_{max}$  Human (**0.915**, percentile (2.5, 97.5) = (0.910, 0.920)),  $Human_{rw}$  (**0.785**, percentile (2.5, 97.5) = (0.773, 0.796)),  $DPR_{rw}$  (**0.889**, percentile (2.5, 97.5) = (0.884, 0.895)), and  $SW_{rw}$  (**0.491**, percentile (2.5, 97.5) = (0.477, 0.505)). (F) Spearman rank correlation squared ( $\rho^2$ , explained variance) between ignition recruitment and the  $out-s_{max}$  Human (**0.726**, percentile (2.5, 97.5) = (0.711, 0.740)),  $Human_{rw}$  (**0.089**, percentile (2.5, 97.5) = (0.076, 0.102)),  $DPR_{rw}$  (**0.339**, percentile (2.5, 97.5) = (0.322, 0.355)), and  $SW_{rw}$  (**0.0006**, percentile (2.5, 97.5) = ( $2 \times 10^{-6}$ , 0.0021)). The \* indicates a significant difference between the  $\rho^2$  of Human and wSCs. The significance of  $\rho^2$  was evaluated using 10.000 replicas from bootstrap resampling (violin plots).

also in the wSCs ensembles. This emphasizes the importance of the inputs in the core as in the local organization with the in-strength. The human connectome fits best to the weighted

core-shell organized than any of the wSCs ensembles. Mesoscale organization fit best with ignition recruitment than the local organization in the human connectome.

Moreover, when the in- $s_{\max}$  is considered, the fit with the ignition sequence is higher than for out- $s_{\max}$  or  $s_{\max}$ . In particular, for the Human<sub>rw</sub> and DPR<sub>rw</sub> ensembles, the  $\rho^2$  value is closer between the  $s_{\max}$  and the in- $s_{\max}$ . However, in the case of the out- $s_{\max}$ , the explained variance of the ignition sequence falls to very low values in the wSCs ensembles. The SW<sub>rw</sub> ensemble shows the lowest  $\rho^2$  between the core and ignited sequences among the analyzed networks. The inputs in the mesoscale organization as in the local organization show a higher relationship with the ignition recruitment through the coupling gain. Thus, the ignition of the human connectome fits best to the weighted core-shell organized than any of the wSCs ensembles.

**Therefore, the weighted mesoscale organization rather than a local one explains better the threshold for the ignition and the ignition recruitment in the human connectome. Also, this exceptional feature of the human connectome cannot be replicated with its connectivity pattern, weight distribution, or even with its local or global organization. The cortical ignition in the connectome is a mesoscale phenomenon rather than a local one, and it is organized in the form of core-shell arrangements.**

### 3. Ignition in neural activity of other organisms is related to the weighted core organization

Finally, I propose that the weighted core-shell organization of ignition is a structural neural principle rooted in evolution, rather than a human connectome uniqueness. These evolutionary roots are assessed using the available connectomes of related organisms, like the macaque (*Macaca mulatta*), the rat (*Rattus norvegicus*), the mouse (*Mus musculus*) or the fruit fly (*Drosophila melanogaster*).

**Table 7. The explained variance of the Spearman rank correlation between ignition and structural measures for *Human* and wSCs.** The explained variance of the Spearman rank correlation ( $\rho^2$ ) between ignition and either  $s_{max}$ , or in-strength, or out-strength, or strength in Human,  $Human_{rw}$ ,  $DPR_{rw}$ , and  $SW_{rw}$ . The percentiles to evaluate the significance of  $\rho^2$  was performed using 10.000 replicas from bootstrap resampling.

<b>Ignition</b>	<b>Human</b> $\rho^2$ , percentile (2.5, 97.5)	<b>Human<sub>rw</sub></b> $\rho^2$ , percentile (2.5, 97.5)	<b>DPR<sub>rw</sub></b> $\rho^2$ , percentile (2.5, 97.5)	<b>SW<sub>rw</sub></b> $\rho^2$ , percentile (2.5, 97.5)
<b>out-<math>s_{max}</math></b>	<b>0.726</b> , (0.711, 0.740)	<b>0.089</b> , (0.076, 0.102)	<b>0.339</b> , (0.322, 0.355)	<b>0.0006</b> , (0.000002, 0.0021)
<b>in-<math>s_{max}</math></b>	<b>0.915</b> , (0.910, 0.920)	<b>0.785</b> , (0.773, 0.796)	<b>0.889</b> , (0.884, 0.895)	<b>0.491</b> , (0.477, 0.505)
<b><math>s_{max}</math></b>	<b>0.867</b> , (0.858, 0.874)	<b>0.474</b> , (0.459, 0.490)	<b>0.495</b> , (0.477, 0.512)	<b>0.100</b> , (0.088, 0.112)
<b>out-strength</b>	<b>0.386</b> , (0.369, 0.402)	<b>0.084</b> , (0.073, 0.096)	<b>0.348</b> , (0.331, 0.365)	<b>0.021</b> , (0.015, 0.027)
<b>in-strength</b>	<b>0.671</b> , (0.655, 0.684)	<b>0.700</b> , (0.687, 0.713)	<b>0.709</b> , (0.695, 0.721)	<b>0.650</b> , (0.636, 0.662)
<b>strength</b>	<b>0.687</b> , (0.672, 0.702)	<b>0.453</b> , (0.435, 0.469)	<b>0.620</b> , (0.606, 0.633)	<b>0.235</b> , (0.221, 0.250)

### 3.1. Organism's connectomes: modeling of ignition and network analysis

The evolutionary root of the core-shell organization and ignition core were assessed using the available connectomes of other organisms. I utilized the connectome of the fruit fly (Figure 15A, top), which has  $N = 50$  neural processing units and 2.049 directed and weighted

connections (network density  $\sim 83\%$ ) (Chiang et al. 2011; Shih et al. 2015); the mouse connectome (Figure 29B, top), parcellated into  $N = 112$  regions (56 per hemisphere) and 6.542 weighted connections (network's density  $\sim 52\%$ ) (Oh et al. 2014; Rubinov et al. 2015); the connectome of the rat (Figure 29C, top), which has  $N = 156$  cortical regions and 6.805 directed connections (network's density  $\sim 28\%$ ) (Bota, Dong, and Swanson 2005; Bota, Sporns, and Swanson 2015); and the CoCoMac dataset of the right hemisphere of the macaque (Figure 29D, top), which has 212 cortical regions and 4.090 directed and unweighted connections (network's density  $\sim 9.1\%$ ) (Bakker, Wachtler, and Diesmann 2012).

To make reliable comparisons with the human connectome, the weight value of the connections in the other organisms was normalized to conserve the overall strength of the Human (15.3). Deterministic simulations show that at steady-state, all the connectomes of other organisms present the bistability range in a range of coupling gain (Figure 29). Thus, the bistability range is conserved in other organisms as a qualitative result (bifurcation points in

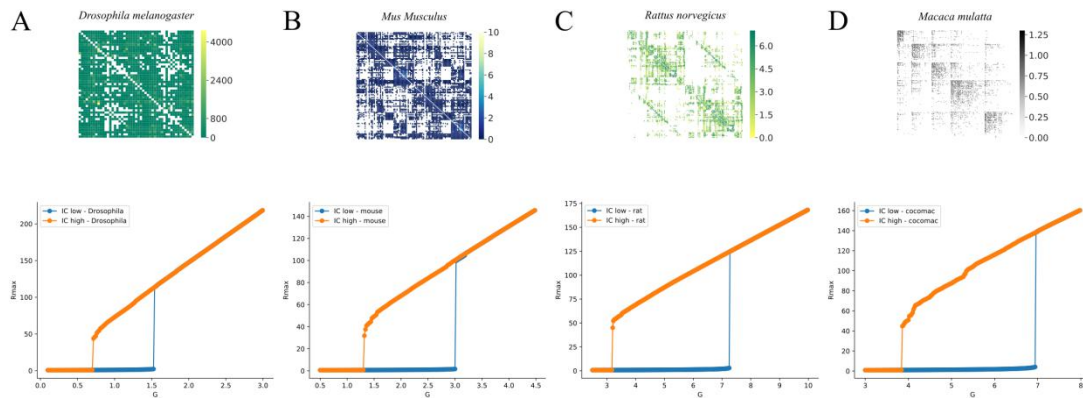


**Figure 29. The bistability range of ignition is preserved in related organisms.** (A) Fruit fly matrix (left) comprises 50 local processing units (columns and rows) and 2.049 weighted connections. (B) Mouse matrix (middle-left) comprises 112 cortical regions (56 per hemisphere) and 6.542 weighted connections. (C) Rat matrix (middle-right) comprises 156 cortical regions and 6.805 weighted connections. (D) Macaque matrix (right) contains 212 cortical regions (right hemisphere) and 4.090 unweighted connections. Bottom, the bistability range of ignition was evaluated in a band of the coupling range for (A) fruit fly ( $0.1 \leq G < 3$ ), (B) mouse ( $0.5 \leq G < 4.5$ ), (C) rat ( $2.5 \leq G < 10$ ), and (D) macaque ( $3 \leq G < 8$ ), all of them with steps of  $G=0.01$ .

**Table 8. The dynamic and structural data of the other organisms connectomes.**

<b>Ignition</b>	<b>Fruit fly</b>	<b>Mouse</b>	<b>Rat</b>	<b>Macaque</b>
<b>G.</b>	0.71	1.31	3.20	3.86
<b>G+</b>	1.53	3.02	7.28	6.94
<b>N.</b>	15 (~30%)	12 (~10.7%)	86 (~55.1%)	59 (~27.8%)
<b>k<sub>max</sub>-core nodes</b>	37 (~74%)	102 (~91.1%)	98 (~62.8%)	104 (49.1%)
<b>s<sub>max</sub>-core nodes</b>	9 (~18%)	16 (~14.3%)	107 (~68.6%)	106 (50%)

Table 8). Nevertheless, the threshold for ignition and flaring points differ between the different organisms connectomes, which could be the result of the differences in the number of nodes, connections, and network density, as well as the weighted pattern, as I demonstrate in the previous section.

### 3.2. The ignition is triggered in the weighted core in other organisms

Table 9 shows the overlaps between the activity state of a region, ignited or not, and if it belongs to s<sub>max</sub>-core -also in or out- or not. I found a larger correspondence in the ignited and s<sub>max</sub>-core of regions at the ignition point G. of the organism's connectomes. However, ignition occurs in regions that belong to neither out-s<sub>max</sub>-core or s<sub>max</sub>-core in all of the organisms. Only in the fruit fly, all the s<sub>max</sub>-core (and out-s<sub>max</sub>-core) ignite at G.. Also, regions that are not-ignited at

**Table 9. The core and the ignited nodes at the G. in the other organisms.** The ignited and not-ignited proportions paired with the belong to the core. The left is the in- $s_{max}$ -core, middle the out- $s_{max}$ -core and right  $s_{max}$ -core, in each entry.

	<b>Fruit fly nodes in/out/total</b>	<b>Mouse nodes in/out/total</b>	<b>Rat nodes in/out/total</b>	<b>Macaque nodes in/out/total</b>
<b>ignited and <math>s_{max}</math>-core</b>	15 /12/ 9	12 /6/ 6	86 /64/ 77	59 /46/ 55
<b>ignited and not <math>s_{max}</math>-core</b>	0 /3/ 6	0 /6/ 6	0 /22/ 9	0 /13/ 4
<b>not-ignited and <math>s_{max}</math>-core</b>	4 /0/ 0	12 /10/ 10	44 /30/ 30	58 /58/ 51
<b>not-ignited and not-<math>s_{max}</math>-core</b>	31 /35/ 35	88 /90/ 90	26 /40/ 40	125 /125/ 132

G. belong massively to the periphery nodes, except in the case of the rat connectome. In fact, in the rat connectome, nearly half of the regions ignite in the bifurcation G-, which is similar to the observed in the uSCs ensembles.

In summary, the ignition is triggered at G. by the nodes that belong to the in- $s_{max}$ -core (Figures 30-33A, left).

### 3.3. The ignition recruitment is related to the structural organization in other organisms

Next, I assessed if the nodes susceptible to be ignited are incorporated following a weighted core-shell rule. Figures 30-33 show the relationship between the ignition recruitment and either the  $s_{max}$  or strength of each node of the connectome of the other organisms (Table 10).

Figure 30A shows the relationship between ignition and the mesoscale organization of the fruit fly connectome. Figure 30B shows the  $\rho^2$  between ignition recruitment and in- $s_{max}$  (**0.965**, percentile (2.5, 97.5) = (0.963, 0.968)), out- $s_{max}$  (**0.772**, percentile (2.5, 97.5) = (0.763, 0.782)), and  $s_{max}$  (**0.925**, percentile (2.5, 97.5) = (0.922, 0.929)) of the fruit fly connectome. Fruit fly connectome shows the best fit of the ignition recruitment with the in- $s_{max}$ -core. Figure 30C shows the relationship between ignition and the local organization of the fruit fly connectome. Figure 30D shows the  $\rho^2$  between ignition recruitment and in-strength (**0.960**, percentile (2.5, 97.5) = (0.958, 0.962)), out-strength (**0.751**, percentile (2.5, 97.5) = (0.741, 0.761)), and strength (**0.920**, percentile (2.5, 97.5) = (0.917, 0.923)) of the fruit fly connectome. The explained variance of the ignition recruitment is higher for the in- $s_{max}$  than the in-strength in the fruit fly connectome, and it is qualitatively similar to the relationship found in the human connectome. It must be said, although, the difference of  $\rho^2$  is statistically significant, is small between the local and mesoscale organization. Also, fruit fly shows the best fit, compared to the other organisms, of the ignition recruitment with the in-strength of the local organization (Table 10).

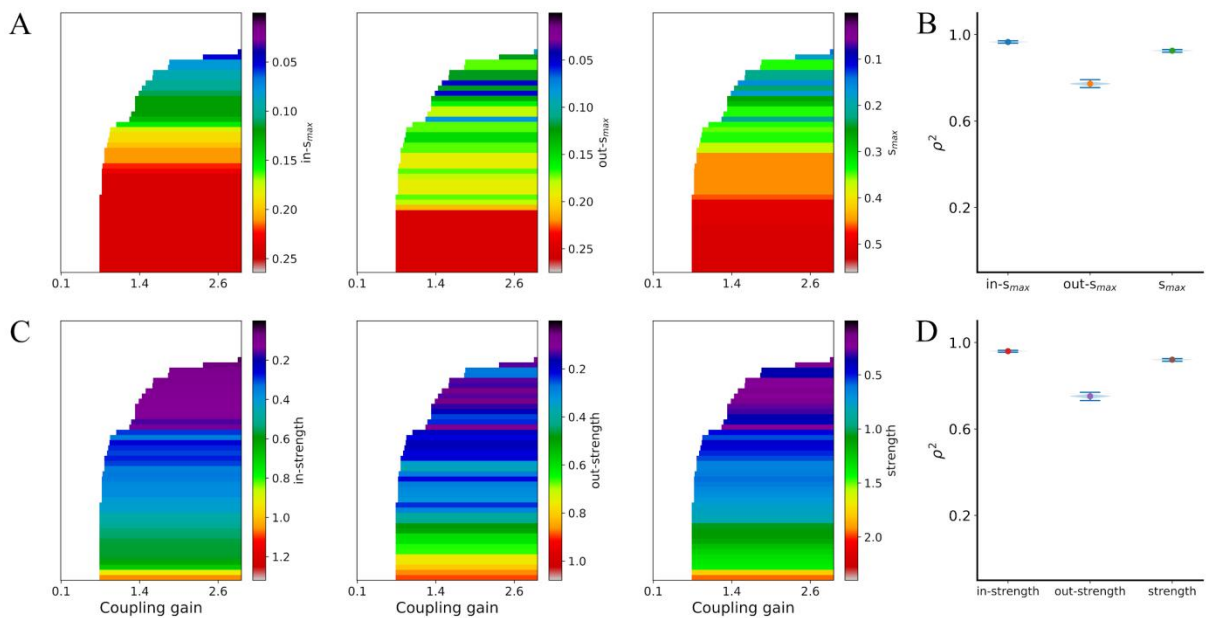
Figure 30A shows the relationship between ignition and the mesoscale organization of the fruit fly connectome. Figure 30B shows the  $\rho^2$  between ignition recruitment and in- $s_{max}$  (**0.965**, percentile (2.5, 97.5) = (0.963, 0.968)), out- $s_{max}$  (**0.772**, percentile (2.5, 97.5) = (0.763, 0.782)), and  $s_{max}$  (**0.925**, percentile (2.5, 97.5) = (0.922, 0.929)) of the fruit fly connectome. Fruit fly connectome shows the best fit of the ignition recruitment with the in- $s_{max}$ -core. Figure 30C shows the relationship between ignition and the local organization of the fruit fly connectome. Figure 30D shows the  $\rho^2$  between ignition recruitment and in-strength (**0.960**, percentile (2.5, 97.5) = (0.958, 0.962)), out-strength (**0.751**, percentile (2.5, 97.5) = (0.741, 0.761)), and strength (**0.920**, percentile (2.5, 97.5) = (0.917, 0.923)) of the fruit fly connectome. The explained

variance of the ignition recruitment is higher for the in- $s_{max}$  than the in-strength in the fruit fly connectome, and it is qualitatively similar to the relationship found in the human connectome. It must be said, although, the difference of  $\rho^2$  is statistically significant, is small between the local and mesoscale organization. Also, fruit fly shows the best fit, compared to the other organisms, of the ignition recruitment with the in-strength of the local organization (Table 10).

**Table 10. The explained variance of the Spearman rank correlation between ignition and structural measures for other organisms connectomes.** The explained variance of the Spearman tfrank correlation ( $\rho^2$ ) between ignition and either  $s_{max}$ , or in-strength, or out-strength, or strength in fruit fly, mouse, rat, and macaque. The percentiles to evaluate the significance of  $\rho^2$  was performed using 10.000 replicas from bootstrap resampling.

<b>Ignition</b>	<b>Fruit fly</b> $\rho^2$ , percentile (2.5, 97.5)	<b>Mouse</b> $\rho^2$ , percentile (2.5, 97.5)	<b>Rat</b> $\rho^2$ , percentile (2.5, 97.5)	<b>Macaque</b> $\rho^2$ , percentile (2.5, 97.5)
<b>out-<math>s_{max}</math></b>	<b>0.772</b> , (0.763, 0.782)	<b>0.345</b> , (0.327, 0.363)	<b>0.135</b> , (0.122, 0.148)	<b>0.350</b> , (0.334, 0.367)
<b>in-<math>s_{max}</math></b>	<b>0.965</b> , (0.963, 0.968)	<b>0.936</b> , (0.933, 0.939)	<b>0.508</b> , (0.492, 0.524)	<b>0.880</b> , (0.875, 0.886)
<b><math>s_{max}</math></b>	<b>0.925</b> , (0.922, 0.929)	<b>0.761</b> , (0.751, 0.771)	<b>0.401</b> , (0.382, 0.420)	<b>0.645</b> , (0.630, 0.658)
<b>out-strength</b>	<b>0.751</b> , (0.741, 0.761)	<b>0.246</b> , (0.223, 0.261)	<b>0.120</b> , (0.108, 0.132)	<b>0.365</b> , (0.348, 0.383)
<b>in-strength</b>	<b>0.960</b> , (0.958, 0.962)	<b>0.913</b> , (0.908, 0.917)	<b>0.697</b> , (0.684, 0.709)	<b>0.912</b> , (0.908, 0.916)
<b>strength</b>	<b>0.920</b> , (0.917, 0.923)	<b>0.673</b> , (0.660, 0.686)	<b>0.443</b> , (0.427, 0.458)	<b>0.685</b> , (0.673, 0.697)

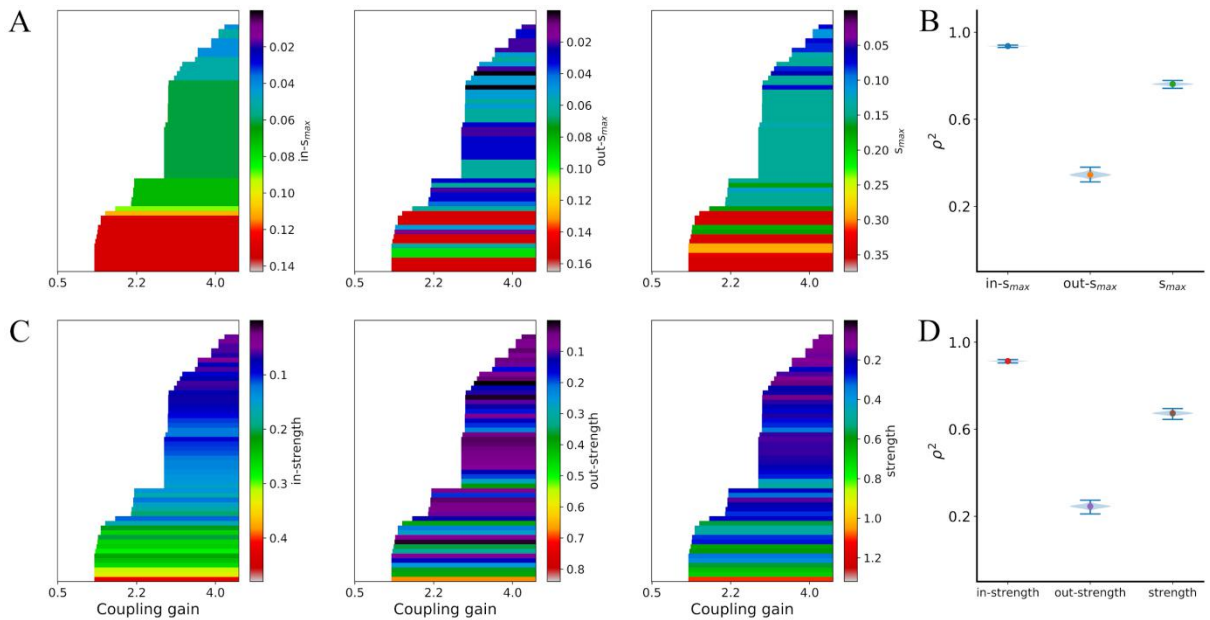
Figure 31A shows the relationship between ignition and the mesoscale organization of the mouse connectome. Figure 31B shows the  $\rho^2$  between ignition recruitment and in- $s_{max}$  (**0.936**, percentile (2.5, 97.5) = (0.933, 0.939)), out- $s_{max}$  (**0.345**, percentile (2.5, 97.5) = (0.327, 0.363)), and  $s_{max}$  (**0.761**, percentile (2.5, 97.5) = (0.751, 0.771)) of the mouse connectome. Figure 31C shows the relationship between ignition and the local organization of the mouse connectome. Figure 31D shows the  $\rho^2$  between ignition recruitment and the in-strength (**0.913**, percentile



**Figure 30. The ignition,  $s_{max}$  and strength levels for each node in the fruit fly (*Drosophila melanogaster*) dataset. (A)** The ignition recruitment of neural processing units ( $y$ -axis) was sorted by the coupling gain ( $x$ -axis). The colour bar shows the in- $s_{max}$  (left), out- $s_{max}$  (middle), and  $s_{max}$  (right) value of each neural processing unit when were ignited. **(B)** Spearman rank correlation squared ( $\rho^2$ , explained variance) between the ignition recruitment and the in- $s_{max}$  (**0.965**, percentile (2,5, 97,5) = (0.963, 0.968), *blue circle*), out- $s_{max}$  (**0.772**, percentile (2,5, 97,5) = (0.763, 0.782), *orange circle*), and  $s_{max}$  (**0.925**, percentile (2,5, 97,5) = (0.922, 0.929), *green circle*). **(C)** Similarly, the sorted ignition recruitment of neural processing units, in which the colour bar represents the in-strength (left), out-strength (middle), and strength (right) value of each neural processing unit when were ignited. **(D)** Spearman rank correlation squared ( $\rho^2$ , explained variance) between the ignition recruitment and the in-strength (**0.960**, percentile (2,5, 97,5) = (0.958, 0.962), *red circle*), out-strength (**0.751**, percentile (2,5, 97,5) = (0.741, 0.761), *purple circle*), and strength (**0.920**, percentile (2,5, 97,5) = (0.917, 0.923), *brown circle*). The significance of  $\rho^2$  was evaluated using 10.000 replicas from bootstrap resampling (the blue violin plots).

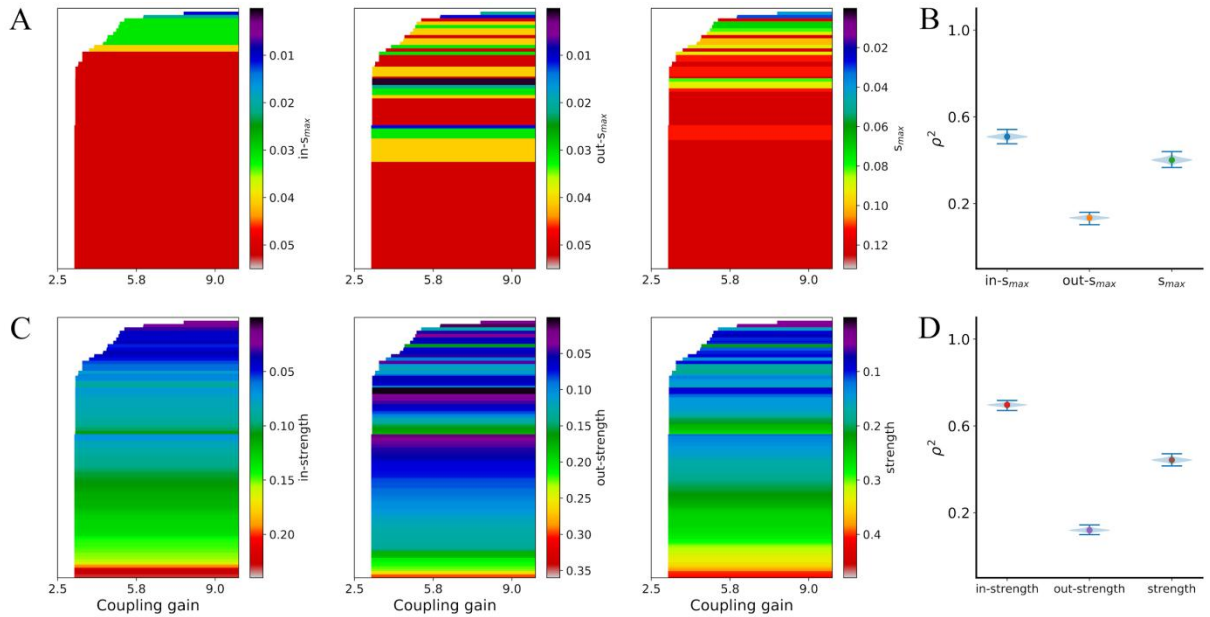
(2.5, 97.5) = (0.908, 0.917)), out-strength (**0.246**, percentile (2.5, 97.5) = (0.223, 0.261)), and strength (**0.673**, percentile (2.5, 97.5) = (0.660, 0.686)) of the mouse connectome. As in the fruit fly, the in- $s_{max}$  of mouse connectome shows a small but statistically significant better fit with the ignition recruitment than the in-strength. Also, the out- $s_{max}$  and out-strength show a lousy relationship with the ignition recruitment in the mouse connectome. That results are qualitatively similar to the relationship between core and ignition found in the human connectome.

Figure 32A shows the relationship between ignition and the mesoscale organization of the



**Figure 31. The ignition,  $s_{max}$  and strength levels for each node in the mouse (*Mus musculus*) dataset. (A)** The ignition recruitment of cortical regions ( $y$ -axis) was sorted by the coupling gain ( $x$ -axis). The colour bar shows the in- $s_{max}$  (left), out- $s_{max}$  (middle), and  $s_{max}$  (right) value of each region when were ignited. **(B)** Spearman rank correlation squared ( $\rho^2$ , explained variance) between the ignition recruitment and the in- $s_{max}$  (**0.936**, percentile (2,5, 97,5) = (0.933, 0.939), *blue circle*), out- $s_{max}$  (**0.345**, percentile (2,5, 97,5) = (0.327, 0.363), *orange circle*), and  $s_{max}$  (**0.761**, percentile (2,5, 97,5) = (0.751, 0.771), *green circle*). **(C)** Similarly, the sorted ignition recruitment of regions, in which the colour bar represents the in-strength (left), out-strength (middle), and strength (right) value of each cortical region when were ignited. **(D)** Spearman rank correlation squared ( $\rho^2$ , explained variance) between the ignition recruitment and the in-strength (**0.913**, percentile (2,5, 97,5) = (0.908, 0.917), *red circle*), out-strength (**0.246**, percentile (2,5, 97,5) = (0.223, 0.261), *purple circle*), and strength (**0.673**, percentile (2,5, 97,5) = (0.660, 0.686), *brown circle*). The significance of  $\rho^2$  was evaluated using 10.000 replicas from bootstrap resampling (the blue violin plots).

rat connectome. Figure 32B shows the  $\rho^2$  between ignition recruitment and the in- $s_{max}$  (**0.508**, percentile (2.5, 97.5) = (0.492, 0.524)), out- $s_{max}$  (**0.135**, percentile (2.5, 97.5) = (0.122, 0.148)), and  $s_{max}$  (**0.401**, percentile (2.5, 97.5) = (0.382, 0.420)) of the rat connectome. Figure 32C shows the relationship between ignition and the local organization of the rat connectome. Figure 32D shows the  $\rho^2$  between ignition recruitment and in-strength (**0.697**, percentile (2.5, 97.5) = (0.684, 0.709)), out-strength (**0.120**, percentile (2.5, 97.5) = (0.108, 0.132)), and strength (**0.443**, percentile (2.5, 97.5) = (0.427, 0.458)) of the rat connectome. Again, the best fit for ignition



**Figure 32. The ignition,  $s_{max}$  and strength levels for each node in the rat (*Rattus norvegicus*) dataset. (A)** The ignition recruitment of cortical regions ( $y$ -axis) was sorted by the coupling gain ( $x$ -axis). The colour bar shows the in- $s_{max}$  (left), out- $s_{max}$  (middle), and  $s_{max}$  (right) value of each region when were ignited. **(B)** Spearman rank correlation squared ( $\rho^2$ , explained variance) between the ignition recruitment and the in- $s_{max}$  (**0.508**, percentile (2,5, 97,5) = (0.492, 0.524), *blue circle*), out- $s_{max}$  (**0.135**, percentile (2,5, 97,5) = (0.122, 0.148), *orange circle*), and  $s_{max}$  (**0.401**, percentile (2,5, 97,5) = (0.382, 0.420), *green circle*). **(C)** Similarly, the sorted ignition recruitment of regions, in which the colour bar represents the in-strength (left), out-strength (middle), and strength (right) value of each cortical region when were ignited. **(D)** Spearman rank correlation squared ( $\rho^2$ , explained variance) between the ignition recruitment and the in-strength (**0.697**, percentile (2,5, 97,5) = (0.684, 0.709), *red circle*), out-strength (**0.120**, percentile (2,5, 97,5) = (0.108, 0.132), *purple circle*), and strength (**0.443**, percentile (2,5, 97,5) = (0.427, 0.458), *brown circle*). The significance of  $\rho^2$  was evaluated using 10.000 replicas from bootstrap resampling (the blue violin plots).

recruitment is with the inputs. The in-strength shows a better fit of  $\rho^2$  with ignition recruitment than the observed for the in- $s_{max}$ . Thus, the local organization of the rat connectome is best related to ignition recruitment, contrary to the observed in the human connectome. One possible explanation is that the ignition in the rat looks as semi-biphasic, in which a lot of the regions ignite nearly the G.. That recalls the performance of the SW<sub>rw</sub> ensemble, in which the in-strength is higher than the in- $s_{max}$ . Thus, the larger network ignition fits better with the in-strength.

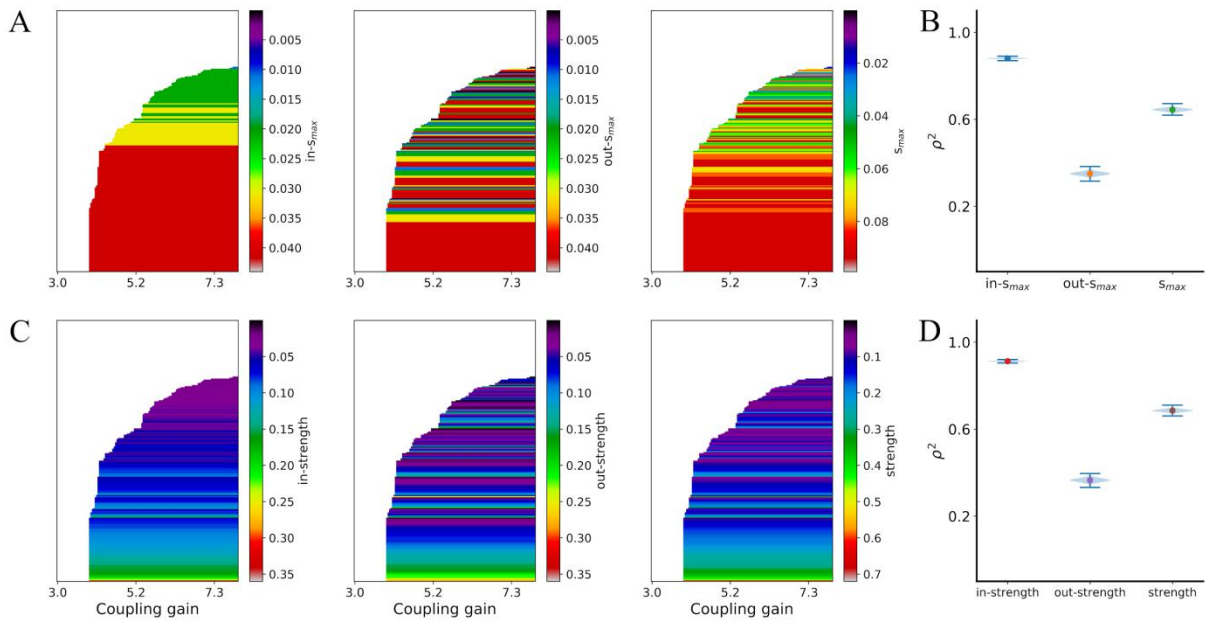


**Figure 33. The ignition,  $s_{max}$  and strength levels for each node in the macaque (*Macaca mulatta*) dataset. (A)** The ignition recruitment of cortical regions ( $y$ -axis) was sorted by the coupling gain ( $x$ -axis). The colour bar shows the in- $s_{max}$  (left), out- $s_{max}$  (middle), and  $s_{max}$  (right) value of each region when were ignited. **(B)** Spearman rank correlation squared ( $\rho^2$ , explained variance) between the ignition recruitment and the in- $s_{max}$  (**0.880**, percentile (2,5, 97,5) = (0.875, 0.886), *blue circle*), out- $s_{max}$  (**0.350**, percentile (2,5, 97,5) = (0.334, 0.367), *orange circle*), and  $s_{max}$  (**0.645**, percentile (2,5, 97,5) = (0.630, 0.658), *green circle*). **(C)** Similarly, the sorted ignition recruitment of regions, in which the colour bar represents the in-strength (left), out-strength (middle), and strength (right) value of each cortical region when were ignited. **(D)** Spearman rank correlation squared ( $\rho^2$ , explained variance) between the ignition recruitment and the in-strength (**0.912**, percentile (2,5, 97,5) = (0.908, 0.916), *red circle*), out-strength (**0.365**, percentile (2,5, 97,5) = (0.348, 0.383), *purple circle*), and strength (**0.685**, percentile (2,5, 97,5) = (0.673, 0.697), *brown circle*). The significance of  $\rho^2$  was evaluated using 10.000 replicas from bootstrap resampling (the blue violin plots).

Figure 33A shows the relationship between ignition and the mesoscale organization of the macaque connectome. Figure 33B shows the  $\rho^2$  between ignition recruitment and the in- $s_{max}$  (**0.880**, percentile (2.5, 97.5) = (0.875, 0.886)), out- $s_{max}$  (**0.350**, percentile (2.5, 97.5) = (0.334, 0.367)), and  $s_{max}$  (**0.645**, percentile (2.5, 97.5) = (0.630, 0.658)) of the macaque connectome. Figure 33C shows the relationship between ignition and the local organization of the macaque connectome. Figure 33D shows the  $\rho^2$  between ignition recruitment and in-strength (**0.912**, percentile (2.5, 97.5) = (0.908, 0.916)), out-strength (**0.365**, percentile (2.5, 97.5) = (0.348, 0.383)), and strength (**0.685**, percentile (2.5, 97.5) = (0.673, 0.697)) of the macaque connectome. Once again, the best fit for ignition recruitment is with the inputs, and the in-strength shows a better fit of  $\rho^2$  with ignition recruitment than the observed for the in- $s_{max}$ . Thus, the local organization of the macaque connectome is best related to ignition recruitment, like the rat and contrary to the observed in the human connectome. This could be related to the fact that the macaque connectome comes from a homogeneous (binary) connectome.

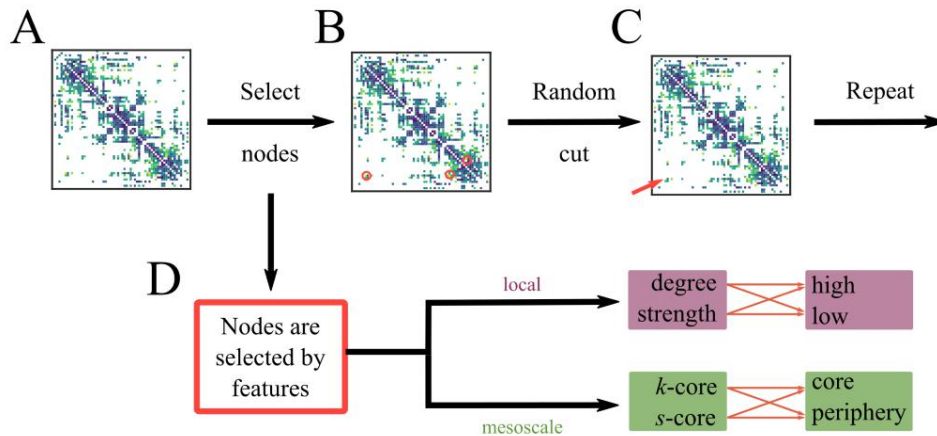
**In conclusion, the s-core decomposition of the human connectome reveals the specific relationship between ignited nodes and its weighted core-shell organization. In phylogenetically related organisms, it is found that the ignition recruitment is primarily related to the inputs to each node. However, best fits with the ignition recruitment could be the local, as in macaque and rat, or mesoscale, as in the fruit fly and mouse. In summary, ignition in other organisms is organized in a core-shell arrangement, but also rely on the nodes with the strongest inputs.**





## Brain network under attack: pruning of the core connections of the human connectome disrupts the bistability range of ignition in cortical activity

So far, I have shown that the ignition in the cortex depends on the structural organization of the human connectome, in particular in the core-shell organization (see chapter 2). I found that regions belonging to a maximally strong  $s$ -core are among the first to sustain spontaneous ignition during simulated resting-state and show the best fit with the ignition recruitment as coupling gain is increased. Also, the high strength nodes explain ignition recruitment through the coupling gain. This chapter further assesses the extent to which the bistability range of ignition is supported by the connections of the cortex, based on their topological organization. I realized a selective pruning of the connectome's connections, distinguishing the local and mesoscale level as highly connected nodes as well as the membership of a densely interconnected core. I hypothesize that connections of the local and/or mesoscale organization are critical to poise the bistability range of the ignition in the human connectome. In this way, I expect that when pruning connections, the remarkably low threshold for the ignition  $G_-$  and flaring  $G_+$  points will be lost. This global effect of pruning on the ignition threshold will be more pronounced when pruning high degree (or high strength) nodes and  $k_{max}$ -core (or  $s_{max}$ -core) than when pruning low degree (or low strength) nodes and those who do not belong to  $k_{max}$ -core (or  $s_{max}$ -core).



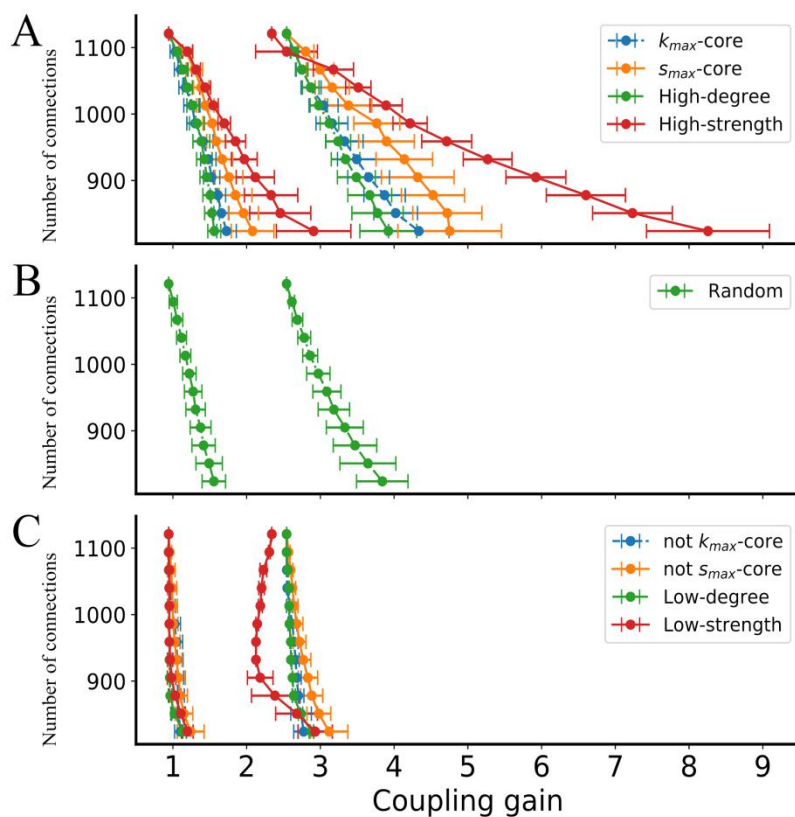
**Figure 34. The pruning procedure.** From the structural connectome (A), I selected a node based on their network organization level to be pruned. From the selected node (B), I randomly removed a connection (C) and then repeated it from (A). (D) Network analysis was applied to select nodes at either local (i.e., degree or strength) or mesoscale (i.e.,  $k$ -core or  $s$ -core decomposition) level. At the local level, I selected either the highly or sparsely connected nodes. At the mesoscale level, I selected nodes that were part of either the core or the periphery.

Figure 34 shows a cartoon of the pruning, in which the structural connections were systematically removed based on the local and mesoscale organization. The pruning procedure has three steps: first (i) apply the network analysis (i.e., degree, strength,  $k$ -core, or  $s$ -core decomposition).

Second (ii) select a node using the chosen network level. Third (iii), randomly prune of one of its connections. I iterate this three steps (i to iii) 27 times and then measure the bifurcation points ( $G_-$  and  $G_+$ ). The procedure is repeated 12 times, thus obtaining 13 bifurcation points, corresponding to pruning 0, 27, 54, 81, 108, 135, 162, 189, 216, 243, 270, 297, and 324 connections. The whole procedure was replicated 20 times on the human connectome. Note that the first bifurcation points correspond to the unpruned network (1.148 connections).

## 1. Pruning of the densely connected nodes

Figure 35A shows the increase of the  $G_-$  and  $G_+$  bifurcation points (left and right lines of the same color, respectively) as the number of connections is decreased (downwards) by pruning connections from nodes with either a high degree (green), high strength (red),  $k_{max}$ -core (blue), or  $s_{max}$ -core (orange). First, the  $G_-$  and  $G_+$  are displaced to the right towards larger  $G$  values. This reinforces the idea that the connections of either highly connected nodes (often called hub nodes) or the core nodes play a fundamental role in the balance for the threshold of the bifurcation  $G_-$  and  $G_+$ . (see the Figures 20B and 24B, chapter 2). Second, pruning connections based on weighted features (strength or  $s_{max}$ -core) of the network have a more substantial effect than the unweighted features



**Figure 35. Effect of selective pruning of the human connectome in the ignition threshold for the bistability range.** Connections were removed from nodes having (A) high-degree (green), high-strength (red), or belonging to  $k_{max}$ -core (blue) or  $s_{max}$ -core (orange); (B) randomly pruning (green); or having (C) low-degree (green), low-strength (red), not belonging to  $k_{max}$ -core (blue) or  $s_{max}$ -core (orange). For each color, lines at the left of each plot are the ignition point  $G_-$  and the lines at right the flaring point  $G_+$ .

(degree or  $k_{max}$ -core). This result is in agreement with the fact that the ignition relationship with structural features has a higher explained variance by the weighted network measures (ignition and  $s_{max}=0.867$ , ignition and strength=0.687; Table 7) than the unweighted ones (ignition and  $k_{max}=0.210$ , ignition and degree=0.255; Table 6).

Third, the pruning of high strength nodes causes a bigger increase in the bifurcation points than the pruning of  $s_{max}$ -core nodes. That could be explained based on the fact that the high strength nodes overlap with the  $s_{max}$ -core nodes, as I show in the previous chapter. Indeed, the core and strongest connected nodes could be responsible for the propagation in the trigger and collapse of the bistable range of ignition. The flaring point  $G_+$  shows the largest increase, and that could explain the decrease of  $G_+$  when the weight distribution is added to the uSCs ensembles (i.e., wSCs ensembles). In particular, the difference in the  $G_+$  bifurcation between the  $SW_{hw}$  and  $SW_{rw}$  networks can be explained with this heterogeneity in the weight of the connections. Thus, the intrinsic ignition is disrupted with the pruning of the highly connected nodes of the human connectome.

## 2. Random pruning

Surprisingly, the random pruning (Figure 35B) has a similar effect as cutting from high degree nodes. This counterintuitive result can be explained because the highest degree nodes ( $n=13$ , 19.7%) concentrate almost one-third of the connections of the connectome (369 connections, 32.14%). Indeed, one-half of nodes ( $n=32$ , 50%) with the lower degree have less than the third of the connections (343 connections, ~29.88%) of the network. In this sense, the

human connectome is far from being homogeneous, and that unique structural manifold allows stable and less expensive cortical ignition. And the same reasoning would apply to the  $k_{max}$ -core nodes ( $n=53$ , 80.3%) of the human connectome, which concentrate almost all the connections of the network (1.058 connections, 91.72%). Thus, the random pruning is highly biased when unweighted network measures are used, and that could explain the similarity with the random pruning, and also with the high degree nodes.

In the case of weighted measures, the high strength nodes ( $n = 11$ , 16.67%) concentrate at least one-third of the overall strength of the network (summed strength = 5.510, 36.01%). Again, the random pruning is highly biased by the specific distribution of the connections' weights of the human connectome. The  $s_{max}$ -core nodes bring together at least a quarter of the overall strength of the network (*summed* strength = 4.054, 26.5%). The summed strength is higher in the high strength nodes than in the  $s_{max}$ -core. Thus, pruning of either strength or  $s_{max}$ -core nodes causes a bigger increase in the bifurcation points than random pruning.

### 3. Pruning of the sparsely connected nodes

Figure 35C shows the overall results of applying the pruning procedure of sparsely connected nodes or periphery nodes (i.e., the ones that do not belong to the core). Pruning connections either from nodes with low-degree, low-strength, or not belonging to  $k_{max}$ -core or  $s_{max}$ -core has a small or null change in the bifurcations  $G_-$  and  $G_+$ . This result supports that the low-degree, low-strength, and peripheral nodes (from  $k_{max}$ -core or  $s_{max}$ -core) are not relevant to the stability of the bifurcations. Note the curious behavior of the pruning of low-strength nodes.

The result of the pruning of the sparsely connected nodes and the peripheral ones confirm that stability in bifurcations  $G_-$  and  $G_+$  depends on the local highly connected nodes as well as on

the core organization of the human connectome. Thus, the effects of pruning connections in the ignition are relevant only when the high degree and strength nodes are considered, as well as when they belong to the  $k_{max}$ -core or  $s_{max}$ -core.

Thus, selectively pruning connections based on connectivity properties, confirms once again the main conclusions of this thesis, obtained in Chapter 2: the strongest nodes (locally or assembling cores) are the most important for ignition and collapse of the network ignition through the coupling gain. This results are in line de Pasquale and colleagues, with say that hubs and cores are fundamental for the network dynamics (de Pasquale et al., 2018). Highly connected nodes and the core of the human connectome sustain bistability at low excitability values.





---

## Discussion

---

This thesis has shown that the bistability of cortical ignition can robustly and naturally occur in the resting-state as an effect of the interplay between regional dynamics and long-range interactions mediated by the cortical connectome. Not all the regions display the same propensity to get ignited. This work contributes to understanding the connectivity influence on the ignition of cortical activity, who is called by Lynn and Basset, the heterogeneous patterns of structural connections (Lynn and Bassett 2019). Using analyses of the graph topology of the connectome -and, notably, of its weighed shell-core structure-, I was able to predict with considerable accuracy the order with which different regions can get spontaneously ignited with increasing inter-regional coupling. I found that regions belonging to a maximally strong s-core are among the first to sustain spontaneous ignition during simulated resting-state. Comparing the Human with a variety of random surrogate connectome ensembles, I found that empirically observed connectomes are “non-random,” in the sense that they display an exceptionally strong and compact  $s_{max}$ -core and give rise to a particularly smooth and gradual increase in the number of ignitable regions as a function of the strength of inter-regional coupling. The main result of my thesis is that the structural organization of the connectome influences the propagation of ignition in cortical activity. In particular, the organization of cores correlates better with ignition recruitment.

Here, I used deterministic simulations to stress the structural influence on the ignition. Deterministic simulations fall in a steady-state, governed by the initial conditions of the system. The whole-brain model was tuned to show the network ignition in the broader range of the coupling gain. I optimized in chapter 1 two ranges of the initial conditions in which the network state is fully determined by their structural relationships and not by the dynamics of the system. Thus, when the model is initialized from the selected range of either Low or High ICs, the broadest possible extent of the bistable network dynamics is obtained. The results are very similar to those obtained by Hansen et al., 2015, despite the optimization of the range of ICs. Thus, it is important to note that in my framework, the ignition depends substantially on the structural organization of the human cortex (Messé et al. 2014; Hansen et al. 2015).

The structural organization is thus a strong determinant of the observed collective dynamics, in line with previous evidence (Honey et al. 2007; Mišić et al. 2015). More than local topology metrics, such as degrees or strengths, or global topology metrics, such as overall small-worldness, I found a mesoscale topological organization,  $s_{max}$  of the core, to be the best predictor of the bistable activity patterns expressed by the model. Most of the regions with largest  $s_{max}$ -core, such as Cuneus, Cingulate, or Precuneus cortices are also members of what Hagmann et al. (Hagmann et al. 2008) dub the “structural core” of Human cerebral cortex, as well as strongly functionally implied in default mode network (DMN) fluctuations (Utevsky, Smith, and Huettel 2014). Such a set of densely interconnected regions had already been hypothesized to play an important role in shaping large-scale resting-state dynamics (Mišić et al. 2015; Hagmann et al. 2008; Betzel, Medaglia, and Bassett 2018), a hypothesis which I here further confirm. Probably, the differences between the core reported here and that reported by Hagmann et al. 2008 arise from the fact that they applied the s-core decomposition to each one of the five individuals and then took an average of the measures. In contrast, I analyze the s-core

on the averaged Human SC. However, I think that I capture qualitatively the same core with the s-core approximation.

At the trigger of the ignition (i.e., at bifurcation G.), there is a correspondence one-to-one with the strongest core of the network. The cortical regions that ignite at G. are present in both hemispheres, except in the case of PARC, which only is part of the left hemisphere (Table 4). The neurobiological relevance of the ignited cortical regions could be useful to the clinical approach, and that is summarized in the next list:

*Pericalcarine cortex* (PCAL), also named the primary visual cortex V1 (Bergmann et al. 2016), was associated with language processing (Bedny et al. 2011), and its neurochemical changes were related to congenital blindness (Coullon et al. 2015). *Cuneus* (CUN) has been identified as a hub of the visual network (Tomasi and Volkow 2011; Widjaja et al. 2013), which was associated with visual working memory (Coppen et al. 2018). In particular, it has been related as an integrator of the early responses of primary visual cortices (Vanni et al. 2001), switching attention and orientation selectivity (Sabbah et al. 2017). *Paracentral lobule* (PARC) was identified as a secondary (or provincial) hub in the visual network (Tomasi and Volkow 2011), as well as in the sensorimotor cortex (Widjaja et al. 2013). It was related to motor action (Zhang et al. 2015), auditory attention shifting, and orienting effect (Xiao et al. 2016). From a clinical perspective, it showed a greater probability of activation in ADHD patients (Xiao et al. 2016; Dickstein et al. 2006), as well as greater functional connectivity in late-life depression (Xiao et al. 2016; Kenny et al. 2010). *Isthmus of the cingulate cortex* (ISTC) was associated with face recognition in the EEG study (Kozlovskiy et al. 2017). Also, it has been reported an early accumulation of  $\beta$ -amyloid, a marker of Alzheimer's disease (Palmqvist et al. 2017). *Precuneus* (PCUN) has been associated with the DMN (Parker, Zalusky, and Kirbas 2014; Deco et al. 2017), the visual and dorsal attention network (Tomasi and Volkow 2011; Widjaja et al. 2013).

From a cognitive perspective, it is related to consciousness (Cavanna 2007), to working memory (Parker, Zalusky, and Kirbas 2014), switching attention and orientation selectivity (Sabbah et al. 2017). Also, it has been reported an early accumulation of  $\beta$ -amyloid, a marker of Alzheimer's disease (Palmqvist et al. 2017). The *posterior cingulate cortex* (PC) has been associated with the DMN (Deco et al. 2017; Widjaja et al. 2013) and the cerebellum hub network (Tomasi and Volkow 2011). Task-related experiments show its relevance in working memory (Parker, Zalusky, and Kirbas 2014). Also, it has been reported an early accumulation of  $\beta$ -amyloid, a marker of Alzheimer's disease (Palmqvist et al. 2017).

From a more abstract statistical mechanics perspective, coreness and core-shell decompositions have been used to describe the propagation of infection on complex networks with inhomogeneous density (Kitsak et al. 2010). Here, an analogy could be drawn between “ignition” and “infection,” with ignition being onset in the densest s-cores, where nodes in a strongly connected neighborhood can trigger each other into an ignited state by mutual excitation (analogously to infection) and mutually stabilize their ignited state by preventing the return to baseline state (analogously to suppressed recovery). Interestingly, the rank correlation between the ignition sequence and the in- or out-strengths in the connectome for different regions were stronger for in-strengths than for out-strengths. This fact indicates that a core region sustains its “infected” state by its neighbors (i.e., trigger from core nodes into an excited state), and the node recruitment will be more likely to get “infected” preferentially via strong input connections from the core regions, enough to maintain them ignited on their turn. Thus, an ignited region by itself cannot excite the peripheral nodes (a leaf) only based on their outputs but requires that the target region receives inputs from other core nodes (a shell). The existence of strong loops of mutual excitation within the largest s-core is thus key to stabilize the ignited state for all the regions belonging to the s-core.

The precise regions that belong to the largest s-core of the connectome do vary depending on the specific chosen empirical reconstruction, and their enumeration is also necessarily affected by the used parcellation. Figures 36-40 of the appendix show indeed that, comparing five alternative empirical reconstructions of the human connectome, the overlap between the included regions is only partial. Remarkably, however, for all these alternative human connectomes, the set of regions that are early ignited largely match the largest s-core. On the contrary, this is not true for the considered surrogate connectomes: all of them display a higher degree of “ignition spill-over” (early ignited regions outside the largest s-core) or “incomplete ignition” (some of the regions in the largest s-core not igniting). It may be that the use of ad hoc search procedures (e.g., genetic algorithms (Alexander Bailey Brock University, St. Catharines, Canada, Mario Ventresca University of Toronto, Toronto, Canada, and Beatrice Ombuki-Berman Brock University, St. Catharines, Canada n.d.)) will allow engineering non-standard surrogate connectomes that would display Human-like or even better than Human ignition capabilities. However, I failed to identify any obvious graph-theoretical feature that confers to Human s-cores their exceptional ignition boosting properties, beyond the ones of generic s-cores. This result opens a way to understand the network influence in cortical activity, and it needs to be tested in experimental predictions. Those predictions need to consider the level of network organization in the intrinsic ignition.

Finally, ignition dynamics are affected not uniquely by an individual graph-theoretical organization of the connectome but by correlations between multiple properties as well. This fact is epitomized by the differences in ignition dynamics between the Human and Human<sub>rw</sub> connectomes. Indeed, the Human<sub>rw</sub> connectome shares with the Human identical unweighted topology and distribution of weights, but the correlations between the two have been disrupted. Analogously, surrogate connectomes with randomized weights display a larger variability over

the ensemble of the actual values of the ignition and flaring points,  $G$  and  $G_+$ , than unweighted ensembles. The fact that all instances within these surrogate ensembles with randomized weights share the same weight distribution and a common statistical distribution of degrees or other topological properties confirms that the critical ignition behavior of the model is influenced much more by weight-to-topology correlations than by weights or topology distributions (Alstott et al. 2014).

Indeed, the ignition features are not well captured by the connectivity pattern of the human connectome. The  $\text{Human}_{\text{hw}}$  gives similar results for ignition as the randomized connectomes of the  $\text{DPR}_{\text{hw}}$ , in which only the number of connections of each cortical region is maintained, but the mesoscale structures are destroyed. Moreover, the result for the fit between ignition and structural measures is very similar in the  $\text{Human}_{\text{rw}}$  and  $\text{DPR}_{\text{rw}}$ . Thus, the specific weight-to-degree pattern of the human connectome is far from being random.

Here I am describing in the connectome an organization that cannot be explained in terms of only pairwise node-to-node relationships, as degree or strength do. The interactions between more than a pair of nodes (i.e., high order interdependencies) have been studied using information theory tools (Rosas et al. 2019; Camino-Pontes et al. 2018). High order interactions give rise to phenomena like redundancy and synergy that appear in the brain activity, that require more than pairwise relationships. A similar situation can be occurring at the connectome level and the strongest s-core, in which the collective organization described by the s-core is a first step toward the description of structural high-order interactions. A question for future research is whether the functional high-order interactions -like the one revealed by non-trivial “meta-connectivity,” constraining fluctuations of pairwise resting-state functional links -are related to the core-shell organization of the connectome (Lombardo et al. 2020).

Even if I cannot yet fully explain the observed ignition behavior of the model in terms of the network organization of the connectome it embeds, this organization remains a strong determinant of the observed dynamics nevertheless. This finding is in apparent contrast with theoretical works based on more abstract network topologies (Battaglia et al. 2012; Kirst, Timme, and Battaglia 2016; Orio et al. 2018) in which the variety of possible dynamical behaviors transcends structural complexity. The first possible reason is that dynamical diversity is strongly amplified by connectome symmetries and the resulting possibility of a multiplicity of ways of breaking these symmetries (Battaglia et al. 2012). Now, the Human connectome, with all its heterogeneities and idiosyncrasies, is far from being symmetric, and the asymmetries need to be tested in the future (Seguin, Razi, and Zalesky 2019). Second, I probe the network influence on ignition of cortical activity, and what is more, which is the level of the network in which this relationship operates. Ignition in cortical activity is supported by core-shell organization in connectomes of human and also related organisms. All the organisms' models have ignition in a bistable range (Figure 29, chapter 2). Third, I focus this work on the network multi-stability between the two main ignited and baseline activity branches of the mean-field whole brain model. However, other sub-dominant states exist between the early ignition  $G_-$  and the late flaring  $G_+$  points, in which the spatial patterns of regional low or high activation levels are less influenced by the structural backbone (Hansen et al. 2015).

Finally, I adopted here straightforward regional dynamics, with bistability between just two fixed points. However, I expect that using neural masses able to express richer regimes -oscillatory, bursting, chaotic, etc. (Orio et al. 2018; Stefanescu and Jirsa 2008; Spiegler et al. 2011)- could eventually reduce the influence of connectivity on collective emergent dynamics. For example, Deco and colleagues use a different approach based on a model with oscillatory activity in each cortical region to define the dynamic core. The main difference between both

approximations is that they used the synchrony features of the system, and I explored the energy of the system exposed in the ignition (i.e., transitions of the mean firing rate activity). In other words, this framework relies on the changes in the energy of the cortical phenomena, and not in the oscillatory phase of the cortical regions. Thus, the selection of the model was a limitation of this work.

Future extensions of this model will have not only to embed richer dynamics but also to investigate more dynamic notions of ignition. The specific way in which I treat ignition within the present study is rather static. I focus on the possibility that specific regions develop bistability between a baseline and an ignited state, and I track at which value of the inert-regional coupling  $G$  this bistability becomes first sustainable. However, I do not study the effects on the ongoing dynamics of an actual switching from baseline to ignited state occurring. Experimentally, local ignition is associated with a “glow,” e.g., to a reverberation of enhanced activation followed by propagation toward neighboring regions (Moutard, Dehaene, and Malach 2015; Noy et al. 2015). Due to this, my approach does not consider the stochasticity in cortical dynamics -another key feature in the ignition-, and that could affect the obtained outcomes (Orio et al. 2018).

Previous studies show that a critical step is the thresholding of activity, which is the basis for the ignition analysis (Messé et al. 2015; Deco and Kringelbach 2017), and it has been studied in the context of epidemic disease (Kitsak et al. 2010; Rock et al. 2014) as well as in neural dynamics (Hütt, Kaiser, and Hilgetag 2014; Mišić et al. 2015). In this context, the mesoscale feature of modularity supports a higher correlation between the structural and functional connectivity in propagation (i.e., the susceptible-excited-refractory (SER) model) and oscillatory models (i.e., Fitzhugh-Nagumo model) (Messé et al. 2015). However, the ignition definition used in those studies (Kitsak et al. 2010; Mišić et al. 2015), and also here, is less sensitive to

dynamic interdependencies of the cortical activity. That is because the models used to capture the steady-state, or the propagation of ignition events, beds on the selected threshold procedure. Thus, the definition of the ignition by the thresholding of cortical activity could be a limitation of the present approach.

Recently, mean-field whole-brain models able to reproduce certain conditions such as propagation of ignition, thanks to a balanced amplification mechanism, have been introduced (Joglekar et al. 2018). Analogously, other modeling studies have measured the “intrinsic ignition” capabilities of different regions by quantifying their capacity to propagate to neighboring regions the effects on activation of a locally received perturbation (Deco and Kringelbach 2017). In my model, I expect that, near the ignition point, perturbing a node within the largest s-core to switch from baseline to a locally ignited state would quickly result in all the other nodes within the largest s-core to get ignited as well, given the strong mutual excitation loops presented within this core. However, I chose here for simplicity to characterize the collective equilibrium state after network ignition has taken place, postponing to future studies the investigation of the out-of-equilibria transient dynamics leading to these ignited equilibria. In this sense, my definition of an ignition core is static. The subset of regions whose local dynamics is pushed by network dynamics to be close to its critical instability point -making them able to switch between low and high firing rate states easily- is quite related to the notion of “dynamic core” introduced by Deco and colleagues (Deco et al. 2017).

In the work of Deco et al., 2017b, they proposed the dynamic core regions, identified after the convergence of a fitting procedure (and not by the study of their participation into ignition dynamic transients), are defined as sitting closely at the bifurcation between asynchronous and oscillating local states. The core regions are the ones closer to the bifurcation after the optimization method. The dynamical cortical core is highly lateralized, in which MOF, PC, and

TT compose the right hemisphere. The left hemisphere is composed of CMF, PREC, PCUN, RAC, and TT. The ignition core (which I proposed) and the dynamic core of Deco have in common only the PCUN and PC. Also, both cortical regions are part of the DMN of resting-state (Deco et al. 2017).

Even without studying the actual propagation dynamics of ignition, my modeling approach discovered that the effects of ignition (i.e., the resulting ignited network states) supported by the Human connectome are the most graded and fine-tunable among all the tested surrogate connectomes. In the “intrinsic ignition framework,” Deco and Kringelbach define the highest level of ignited nodes as the “binding nodes” for the broadcasting of information (Deco and Kringelbach 2017). They proposed that this obeys a hierarchical information processing pattern, which they split into four classes of ignition is defined, that range from weak non-hierarchy to graded uniform hierarchy (Figure 36A-D). In the first case, all the nodes have the same susceptibility to be ignited, while in the latter case, there exists a linear uniform gradation in the ignition of the nodes. Between these poles, two other classes are staircase hierarchy and graded non-uniform hierarchy.

My results fit better with the staircase hierarchy class; there is a subset of nodes susceptible to be ignited, and this number is smoothly controlled by the coupling gain (Figure 36E, orange arrow). In the surrogate models, there is a narrower range for the recruitment of cortical regions as  $G$  is increased (Figure 36F). Moreover, my investigation of randomized surrogate connectomes reveals that the likelihood that connectome structures supporting such a graded non-uniform hierarchy of possible ignited network states arise by chance is rather small. Thus, there must be some reason for which the Human happens to be as it is, a needle in the haystack of possible connectomes.

In this sense, the ignition core defines a set of densely interconnected cortical regions that allows the first ignition. Because the cortical regions of the human cortex are also observed in static and well defined resting-state networks, I propose that the ignition core is related to this ongoing cortical activity of the brain. Although they can be thought of as the core regions that support static activity fluctuations, they are a weak candidate to explain the dynamic fluctuations of the cortical activity (de Pasquale et al. 2018). In other words, their rough control of ignition across different excitatory levels makes them a bad option to modulate the fast fluctuations in cortical activity. Instead, the subsequent shells of the core organization could be modulated by the excitatory level of the network. They are stronger candidates to be related to dynamical fluctuations in cortical activity observed in human resting-state data (Hansen et al. 2015). The human connectome shows that the controllability of the ignition by the core-shell organization is greater than described for the structural models, which have a weaker core-shell structure. Thus, shells allow a richer dynamic range of ignition and are more complex in the human connectome.

Regarding that evidence, I suggest that the ignition needed to conscious perception but also for the intrinsic cortical activity (Moutard, Dehaene, and Malach 2015), could have evolutionary roots in the structural organization. This is because the ignition is supported and constrained by the core-shell organization. The evolutionary roots of ignition in a mesoscale level have support in the work of Betzel, Medaglia, and Bassett (Betzel, Medaglia, and Bassett 2018). They found that mesoscale organization is conserved in human and non-human connectomes, in the form of assortative communities (modules more within- than between-connected), disassortative communities (modules defined by similarities in the organization pattern), and cores. In my work, I go one step further. I show that core-shell organization is crucial to support ignition in a large-scale model of cortical activity of mouse (*Mus musculus*) and fruit fly (*Drosophila*

*melanogaster*). In this sense, the conservation of mesoscale organization can be considered as the neural principle to support the ignition in cortical activity.

The relationship between ignition and core-shell organization could be related to developmental or evolutionary constraints. The first scenario is that the selection of a connectome with such non-random features is driven by developmental constraints, imposing specific construction principles to be respected but keeping network connectivity otherwise maximally random. The development also has a critical role in the fine-tuning of the determination and variability of the structural connectivity in humans (Teeuw et al. 2019) and non-human brains (Khundrakpam et al. 2013). Thus, evolution is more a component to be added in the assembly of the structural connectivity of the organisms than a determinant. Rubinov (Rubinov and Sporns 2010) evokes the notion of “spandrel,” the triangular spaces that are unavoidably created between arches, pillars, and beams when constructing a cathedral. These spandrels are statistically as frequent than the other structural architectural elements -the arches, pillars, and beams that bear the weight of the building- but are not in the plan, i.e., they are byproducts of other constraints and construction targets. Such a scenario of the emergence of a Human-like ignition-core as a byproduct of some other graph-theoretical construction rule, e.g., imposed degree or small-worldness, was implicitly probed by the procedure of testing the Human connectome against null-hypotheses, represented by increasingly more constrained

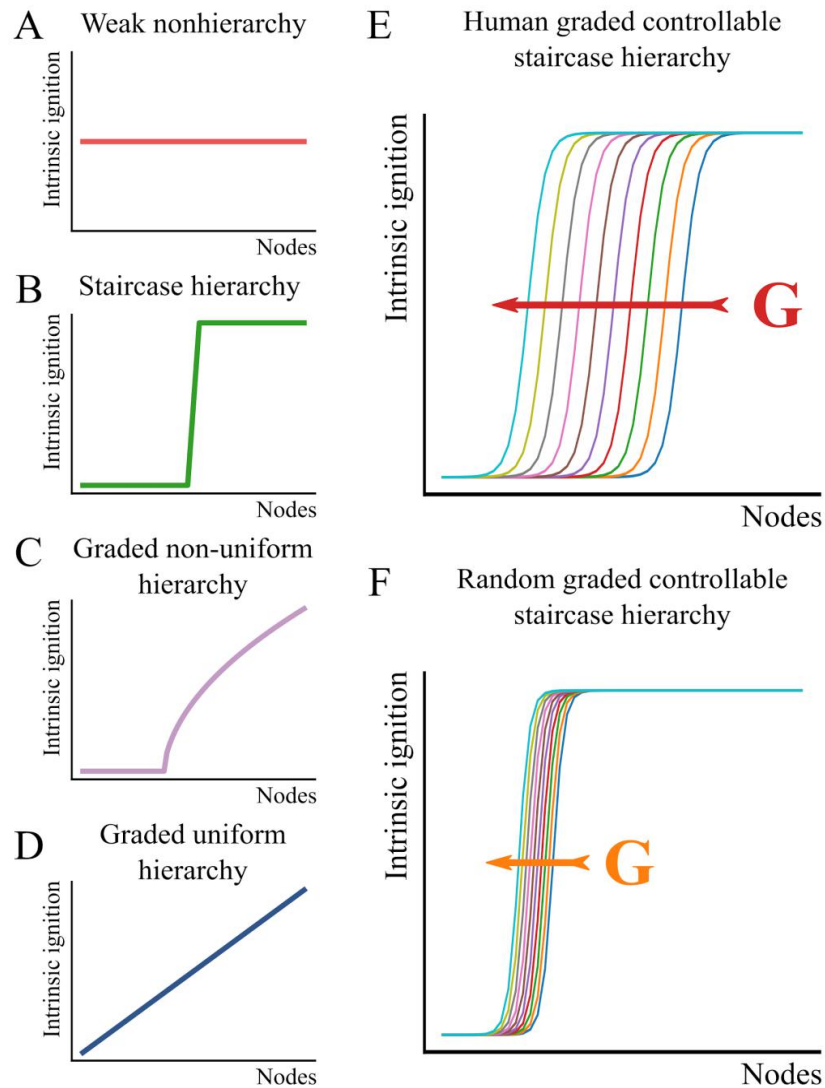


**Figure 36. The intrinsic ignition framework.** Following Deco and Kringelbach (2017a), I used the ignition framework to classify the cortical regions of the Human. They define four classes ignition, that range from **(A)** weak non-hierarchy to **(D)** graded uniform hierarchy. In the first case, all the nodes have the same susceptibility to be ignited, while in the latter case exists a linear uniform gradation in the hierarchy between the nodes. Between these poles, two other classes are **(B)** staircase hierarchy and **(C)** graded non-uniform hierarchy. In both cases, only a subset of nodes in the network is susceptible to be ignited; in the staircase, the ignited nodes are a subset without specific hierarchy, while in **(C)** ignited nodes have a non-uniform hierarchy. **(E)** The results fit better with the staircase hierarchy class. The number of nodes susceptible to be ignited in the Human is smoothly controlled by the coupling gain, as shown in the orange arrow. Moreover, ignited nodes of Human are modulated on a broader range than in the **(F)**  $DPR_{rw}$  (blue arrow), as in the example.

families of surrogate connectomes. The failure to reproduce Human-like ignition-cores in any of the attempted surrogates leaves, however, opens the question of which could be the hidden developmental constraints inducing the emergence of the exceptional Human s-core.

A second scenario is that such an exceptional core organization as the Human does not emerge as a “spandrel” but is actually favored over others along with evolution for the fitness, if not optimality in some sense, that it confers. Interestingly, empirical connectomes extracted from another non-human organism (Betzel, Medaglia, and Bassett 2018; Markov et al. 2013; Gămănuț et al. 2018), also include prominent structural cores in their organization that matches the set of firstly ignited nodes (Figures 29-33, chapter 2). There are many examples of ignition. In the work of Aulet and collaborators, suggest that the neural mechanism needed for the canine sense of quantity perception has been conserved across mammalian evolution (Aulet et al. 2019). Also, the resting-state networks substantially overlap between macaque (*Macaca mulatta*), common marmoset monkey (*Callithrix jacchus*) and humans (Ghahremani et al. 2017).

Future investigations may check whether an ignition behavior as the one I observed for Human connectomes is progressively set in place while adopting connectomes that follow a phylogenetic sequence, even if comparative connectomic analyses are still incomplete (Betzel, Medaglia, and Bassett 2018; van den Heuvel, Bullmore, and Sporns 2016). Furthermore, yet, the specific optimization goals for which the empirical connectomes should be constructed are unknown. Several independent studies suggest that wiring cost minimization may be relevant but not sufficient to explain the observed connectome wiring, which at the same time seems to optimize information-processing related quantities (Kaiser and Hilgetag 2006; Vertes, Hoover, and Rodriguez 2012).

Here I advance the hypothesis that eventual reasons making the human connectome fit, and thus selected under evolutionary pressure, could (speculatively) be: first, the exceptionally low ignition point  $G_c$ , allowing to initiate and sustain an ignited state with relatively low inter-areal couplings (and thus more efficient use of synaptic transmission resources and connecting fibers amount); second, the exceptionally graded increase of the number of regions admitting bistable ignition when further increasing the coupling  $G$ . Indeed, thanks to this graded rise -here modeled by changes of the effective  $G_c$ , shifts in the cortical networks' "working point" induced, e.g., by neuromodulation (Shine et al. 2018; Medel et al. 2019), arousal (Ham et al. 2008; Churchland et al. 2010; Pinto et al. 2013; Noy et al. 2015), or other intrinsic or extrinsic mechanisms (Moutard, Dehaene, and Malach 2015), would give rise to the largest extent of possible ignition patterns and then, possibly, to subtle controllability of the extent of inter-regional integration.

My hypothesis implicitly postulates a decisive functional role for the existence of subsets of ignited regions and the possibility of their fine-tuned control (Figure 36). As previously mentioned, the emergence of ignited activity into extended regional subsets, beyond early sensory regions has been repeatedly associated with conscious perception (Moutard, Dehaene, and Malach 2015), requiring the recruitment of a global workspace (Dehaene and Changeux 2011). In this sense, connectomes facilitating early ignition would favor at the same time, the emergence of a substrate dynamical repertoire required for integrated perception and, more in general, integrated information processing. Analogously, the potential ignited network states characterized by graded non-uniform hierarchy (e.g., recruiting narrower or wider nested circles of regions), could provide the mechanistic basis for "graded consciousness" states (Windey and Cleeremans 2015). In this sense, the ignition workspace for consciousness can take place in a variety of possible ways, encompassing an increasing number of possible dimensions (Bayne, Hohwy, and Owen 2016), rather than just being "all-or-none."

The Global Workspace Theory, proposed by Baars in 1988 (Baars 30 de julio de 1993), defines a network in which the activity pattern of the central nodes define the conscious perception, and it is called the global workspace. From a biological perspective, the mammalian brain instantiates such a global workspace architecture (Connor and Shanahan 2007). Periphery nodes compete and collaborate in a structured fashion to broadcast their activity to the global workspace nodes. The cortical activity fluctuations, supported by the core, were postulated as the changes in the global workspace (Moutard, Dehaene, and Malach 2015). In my work, the ignition in cortical activity was supported by a specific anatomical backbone, the core-shell organization.

The ignition in the human connectome has an exceptional feature related to the core-shell organization. First, ignition has an exceptionally low excitability coupling threshold for its first trigger. Second, in Human, the ignition sequence is more core-shell organized than in surrogate models. Both results strongly suggest a neural activity organization at this level. Moreover, I find that this relationship is maintained in the neural circuits of related organisms. Combining those results, I propose as a principle rooted in evolution, in which the relationship between a core-shell organization and the ignition sequence of cortical regions emerges as a principle of the neural architecture.

In summary, I optimized the model to show the broader bistability range, depending on the time of simulation, time-step, and initial conditions. Then, I show that at the trigger of the network ignition exists a perfect relationship with the strongest interconnected core nodes, the ignition core. Also, the ignition recruitment of the cortical regions in the human connectome is more related to a core-shell organization rather than a strength gradient of its cortical regions. The core organization is a mesoscale feature of the networks, and its underpinnings in cortical structure have been previously reported. The ignition core and the core-shell organization of

ignition are not well captured even with models that preserve connectivity patterns, local sequence, complex features, or even the weight distribution of the human connectome. Thus, this core-shell organization is a specific feature of the human connectome that supports its ignited cortical activity. Finally, I examine the evolutionary roots of this relationship using the available connectomes of related organisms, like the macaque, the rat (*Rattus norvegicus*), the mouse, or even the fruit fly. Ignition core is preserved for the in- $s_{\max}$ -core in the related organism's connectomes. However, the ignition recruitment can have the best fit for in-strength than for the  $s_{\max}$ , as in rat and macaque connectomes. In conclusion, this specific ignition core is a structural principle of neural ignition.



## 1. Controls for the human dataset of Hagmann

The relationship between ignition in cortical activity and core organization of the Hagmann's human connectome dataset (Hagmann et al. 2008) is the principal result of chapter 2. However, the process to generate the human connectome has high variability between and within-population datasets (Lynn and Bassett 2019). Here, using other human datasets, it is evaluated if the results obtained for that Hagmann data are reliable (Table 11).

**Schirner dataset.** First, I test the reliability of the DKA. I use the Schirner dataset, which comprises an average of 50 subjects (Schirner et al. 2015) (Figure 37A). This dataset has a higher network density (~98%) than the Hagmann one (~27%). The Schirner dataset has the bistability range, in which the ignition point is  $G_-=0.825$ , and the flaring point is  $G_+ = 1.725$ .

Figure 37B shows the sorted coupling gain of the first ignition ( $x$ -axis) of each cortical area ( $y$ -axis). In color is shown the  $s_{\max}$  of each cortical area. Similarly, Figure 37C shows in color the strength of each cortical area. The ignition starts in the  $s_{\max}$ -core nodes (4, ~6%). The strength does not capture the ignited nodes at  $G_-$  as well as the  $s_{\max}$ -core. In the Schirner dataset, the four cortical regions that ignite at  $G_-$  are Medial Orbitofrontal Cortex (MOF, R), Lingual Gyrus (LING, R), Superior Parietal Cortex (SP, L), and the Lateral Occipital Cortex (LOCC, L). Figure 37D shows the Spearman rank correlation squared ( $\rho^2$ , explained variance) between ignition recruitment and either  $s_{\max}$  (0.967) or strength (0.906). Even if the  $\rho^2$  is statistically higher when

**Table 11. The explained variance of the Spearman rank correlation between ignition and structural measures for Human connectomes.** The explained variance of the Spearman rank correlation ( $\rho^2$ ) between ignition and either  $s_{max}$  or strength in the Human connectomes of Schirner, Wirsich, Deco76, Deco90, and Deco116. The percentiles to evaluate the significance of  $\rho^2$  was performed using 10.000 replicas from bootstrap resampling.

<b>Ignition</b>	<b>Schirner</b> $\rho^2$ , percentile (2.5, 97.5)	<b>Wirsich</b> $\rho^2$ , percentile (2.5, 97.5)	<b>Deco76</b> $\rho^2$ , percentile (2.5, 97.5)	<b>Deco90</b> $\rho^2$ , percentile (2.5, 97.5)	<b>Deco116</b> $\rho^2$ , percentile (2.5, 97.5)
<b><math>s_{max}</math></b>	<b>0.967</b> , (0.965, 0.969)	<b>0.876</b> , (0.871, 0.881)	<b>0.846</b> , (0.839, 0.854)	<b>0.667</b> , (0.655, 0.679)	<b>0.634</b> , (0.614, 0.654)
<b>strength</b>	<b>0.906</b> , (0.902, 0.910)	<b>0.576</b> , (0.563, 0.589)	<b>0.551</b> , (0.535, 0.567)	<b>0.515</b> , (0.498, 0.531)	<b>0.625</b> , (0.611, 0.638)

the  $s_{max}$  is considered, the strength values also very high in the Schirner dataset. Thus, the Schirner dataset supports that the ignition recruitment is related to core organization, despite the differences in the network density with the Hagmann connectome. Although, the network density of the Schirner dataset seems to be relevant in the values of the rank correlation of the strength with the ignition recruitment.

**Wirsich dataset.** Then, I test the reliability of the results of the Hagmann dataset using another atlas, the AAL atlas (Tzourio-Mazoyer et al. 2002; Rolls, Joliot, and Tzourio-Mazoyer 2015). The Wirsich connectome is an average of 11 subjects, with 96 nodes and 8.866 connections (Wirsich et al. 2018) (Figure 38A). The Wirsich dataset also has a higher network density (~97%) than the Hagmann one (~27%), and present the bistability range, in which the ignition point is  $G_- = 1.795$ , and the flaring point is  $G_+ = 4.415$ .

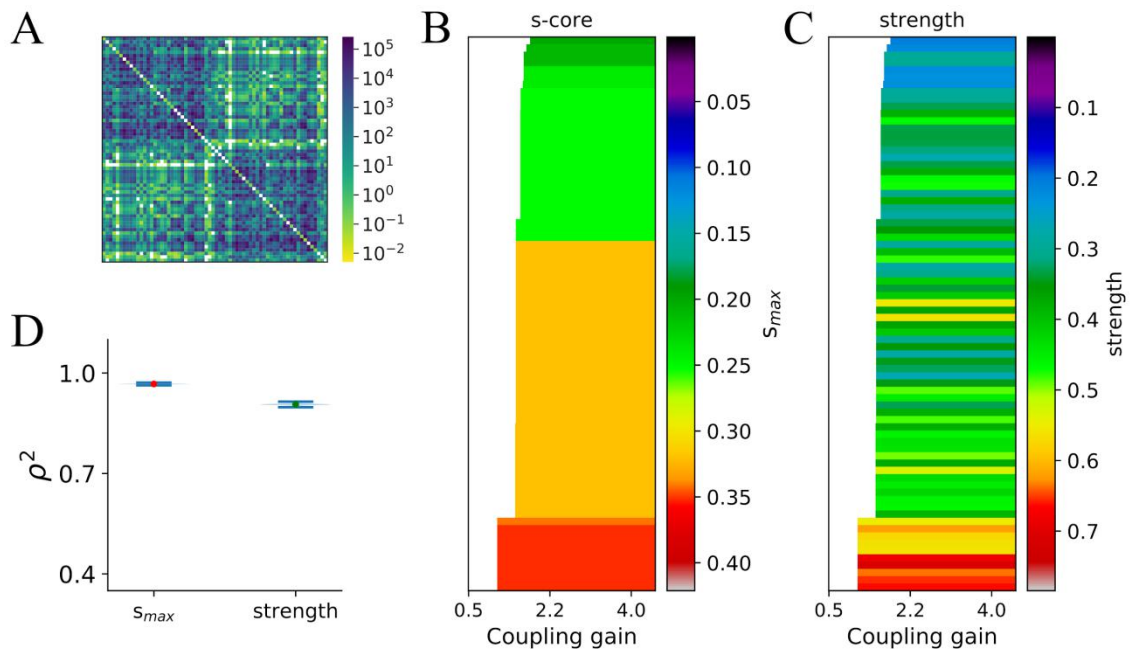


**Figure 37. The ignition, s-core, and strength levels for each cortical region in the Schirner dataset.** (A) The Schirner connectivity matrix was parcellated using the Desikan-Killiany atlas (66 cortical regions and 4.290 connections). (B) The relationship between ignition and  $s_{max}$  of each cortical region of the Schirner connectome. Cortical regions in the  $y$ -axis are sorted according to the coupling gain  $G$  ( $x$ -axis) value at which they first ignite. Colour code shows the  $s_{max}$  for each of the ignited cortical regions. (C) Similarly, the relationship between ignition recruitment and the strength (color bar) of each cortical region. (D) The explained variance of Spearman rank correlation ( $\rho^2$ ) between ignition recruitment and the  $s_{max}$  (**0.967**, percentile (2.5, 97.5) = (0.965, 0.969), *red dot*), and strength (**0.906**, percentile (2.5, 97.5) = (0.902, 0.910), *green dot*). The Schirner connectome shows that  $s_{max}$  has a significantly higher explained variance of ignition recruitment than the strength. However, both rank values are very high. The significance of  $\rho^2$  was evaluated using 10.000 replicas from bootstrap resampling (violin plots).

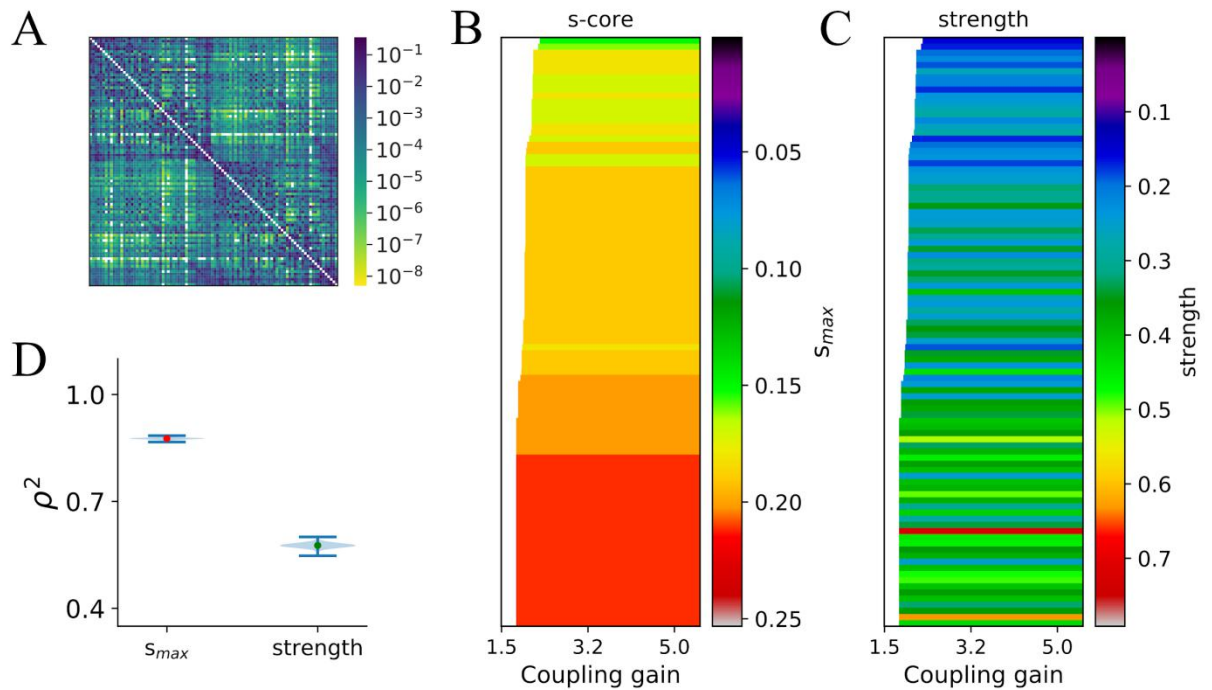
Figure 38B shows the sorted coupling gain of the first ignition ( $x$ -axis) of each cortical area ( $y$ -axis). In color is shown the  $s_{max}$  of each cortical area. Similarly, Figure 38C shows in color the strength of each cortical area. In the Wirsich dataset, the ignition starts in the  $s_{max}$ -core nodes (28, ~29%). However, six nodes that do not belong to the  $s_{max}$ -core are ignited at  $G$ . The strength does not capture the ignited nodes at  $G$  as well as the  $s_{max}$ -core.

Figure 38D shows the Spearman rank correlation squared ( $\rho^2$ , explained variance) between ignition recruitment and either  $s_{\max}$  (0.876) or strength (0.576). The  $\rho^2$  of ignition recruitment is statistically higher when the  $s_{\max}$  is considered. However, ignition recruitment is enclosed in a very narrow range of the coupling gain. Thus, the Wirsich dataset supports that the ignition recruitment is related to core organization, despite the differences in the parcellation with the Hagmann connectome.

**Deco dataset.** Finally, I test if the number of neural elements considered in the parcellation influences the relationship between ignition recruitment and core organization. For that, I use the connectome reported by the group of Deco (Deco et al. 2018), which was parcellated using the AAL from an average of 16 subjects, and it is divided into cortical regions, cortical + subcortical regions and cortical + subcortical + cerebellum regions.

The parcellation that considers only cortical regions was called the Deco76 dataset, which had 76 nodes and 2.076 connections (Figure 39A). The Deco76 dataset also has a higher network density ( $\sim 36\%$ ) than the Hagmann one ( $\sim 27\%$ ), and present the bistability range, in which the ignition point is  $G_-=1.115$ , and the flaring point is  $G_+ = 3.125$ .

Figure 39B shows the sorted coupling gain of the first ignition ( $x$ -axis) of each cortical area ( $y$ -axis). In color is shown the  $s_{\max}$  of each cortical area. Similarly, Figure 39C shows in color the strength of each cortical area. In the Deco76 dataset, the ignition starts in the  $s_{\max}$ -core nodes (9,  $\sim 11\%$ ). However, one node that does not belong to the  $s_{\max}$ -core is ignited at  $G_-$ . The strength also captures the ignited nodes at  $G_-$  as well as the  $s_{\max}$ -core. In the deco76 dataset the ten cortical regions that ignite at  $G_-$  are Precuneus (PCUN, R), Supramarginal Gyrus (SMG, R), Posterior Cingulate Gyrus (PCC, L), ParaHippocampal Gyrus (PHG, L), Hippocampus (HIP, L),



**Figure 38. The ignition, s-core, and strength levels for each region in the Wirsich dataset.** (A) The Wirsich connectivity matrix was parcellated using the Automated Anatomical Labelling atlas (96 cortical + subcortical regions, and 8.866 connections). (B) The relationship between ignition and  $s_{max}$  of each region of the Wirsich connectome. Cortical and subcortical regions ( $y$ -axis) are sorted according to the coupling gain  $G$  ( $x$ -axis) value at which they first ignite. Colour code shows the  $s_{max}$  for each of the ignited regions. (C) Similarly, the relationship between ignition recruitment and the strength (color bar) of each region. (D) The explained variance of Spearman rank correlation ( $\rho^2$ ) between ignition recruitment and the  $s_{max}$  (**0.876**, percentile (2.5, 97.5) = (0.871, 0.881), *red dot*), and strength (**0.576**, percentile (2.5, 97.5) = (0.563, 0.589), *green dot*). The Wirsich connectome shows that  $s_{max}$  has a significantly higher explained variance of ignition recruitment than the strength. The significance of  $\rho^2$  was evaluated using 10.000 replicas from bootstrap resampling (violin plots).

Calcarine Fissure (CAL, L), Inferior Parietal Gyrus (IPG, L), Inferior Temporal Gyrus (ITG, R), and Angular Gyrus (ANG, R).

Figure 39D shows the Spearman rank correlation squared ( $\rho^2$ , explained variance) between ignition recruitment and either  $s_{max}$  (0.846) or strength (0.551). The  $\rho^2$  of ignition recruitment is statistically higher when the  $s_{max}$  is considered. Thus, the Deco76 dataset supports that the

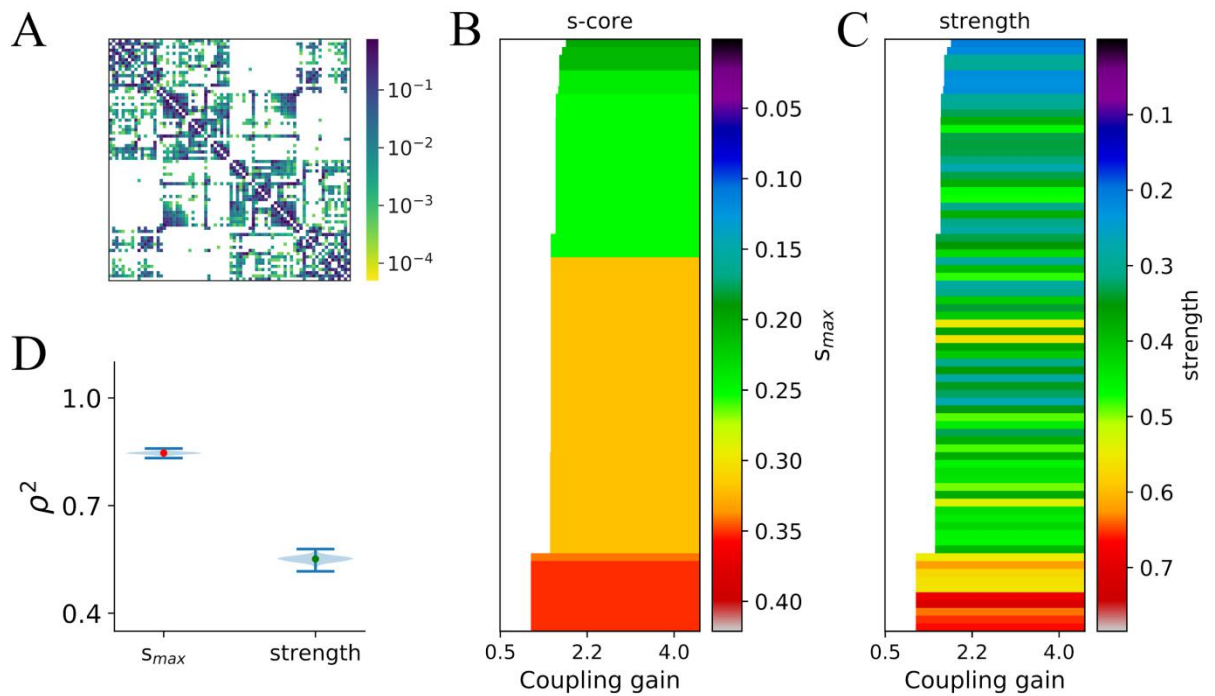


**Figure 39. The ignition,  $s$ -core, and strength levels for each cortical region in the Deco76 dataset.** (A) The Deco76 connectivity matrix was parcellated using the Automated Anatomical Labelling atlas (76 cortical regions and 2.076 connections). (B) The relationship between ignition and  $s_{max}$  of each cortical region of the Deco76 connectome. Cortical regions in the  $y$ -axis are sorted according to the coupling gain  $G$  ( $x$ -axis) value at which they first ignite. Colour code shows the  $s_{max}$  for each of the ignited cortical regions. (C) Similarly, the relationship between ignition recruitment and the strength (color bar) of each cortical region. (D) The explained variance of Spearman rank correlation ( $\rho^2$ ) between ignition recruitment and the  $s_{max}$  (**0.846**, percentile (2.5, 97.5) = (0.839, 0.854), *red dot*), and strength (**0.551**, percentile (2.5, 97.5) = (0.535, 0.567), *green dot*). The Deco76 connectome shows that  $s_{max}$  has a significantly higher explained variance of ignition recruitment than the strength. The significance of  $\rho^2$  was evaluated using 10.000 replicas from bootstrap resampling (violin plots).

ignition recruitment is related to core organization, despite the differences in the parcellation with the Hagmann connectome.

The parcellation that considers cortical + subcortical regions was called Deco90 dataset, which had 90 nodes and 3.162 connections (Figure 40A). The Deco90 dataset also has a higher network density (~39%) than the Hagmann one (~27%), and present the bistability range, in which the ignition point is  $G_-=1.465$ , and the flaring point is  $G_+ = 3.985$ .

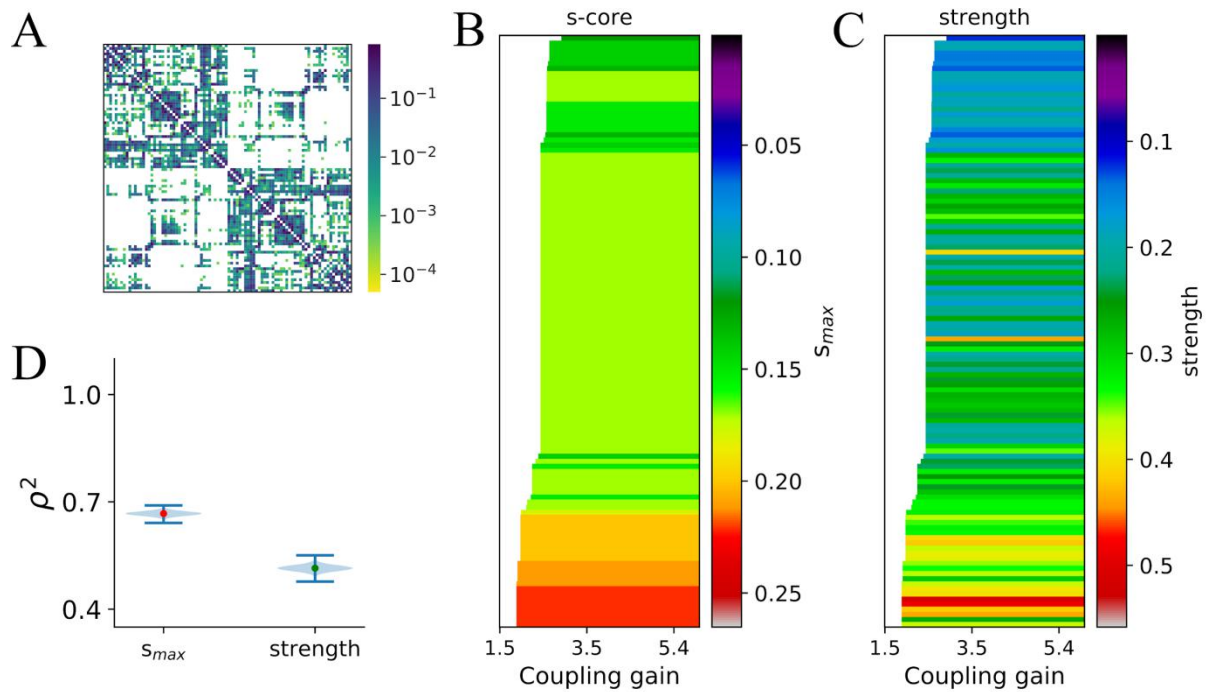


**Figure 40. The ignition,  $s_{\max}$ , and strength levels for each region in the Deco90 dataset.** (A) The Deco90 connectivity matrix was parcellated using the Automated Anatomical Labelling atlas (90 cortical + subcortical regions, and 3.162 connections). (B) The relationship between ignition and  $s_{\max}$  of each region of the Deco90 connectome. Regions in the  $y$ -axis are sorted according to the coupling gain  $G$  ( $x$ -axis) value at which they first ignite. Colour code shows the  $s_{\max}$  for each of the ignited regions. (C) Similarly, the relationship between ignition recruitment and the strength (color bar) of each region. (D) The explained variance of Spearman rank correlation ( $\rho^2$ ) between ignition recruitment and the  $s_{\max}$  (**0.667**, percentile (2.5, 97.5) = (0.655, 0.679), *red dot*), and strength (**0.515**, percentile (2.5, 97.5) = (0.498, 0.531), *green dot*). The Deco90 connectome shows that strength has a significantly higher explained variance of ignition recruitment than the  $s_{\max}$ . The significance of  $\rho^2$  was evaluated using 10.000 replicas from bootstrap resampling (violin plots).

Figure 40B shows the sorted coupling gain of the first ignition ( $x$ -axis) of each cortical area ( $y$ -axis). In color is shown the  $s_{\max}$  of each cortical area. Similarly, Figure 40C shows in color the strength of each cortical area. In the Deco90 dataset, the ignition starts in the  $s_{\max}$ -core nodes (9, ~10%). However, one node that does not belong to the  $s_{\max}$ -core is ignited at  $G$ . The strength also captures the ignited nodes at  $G$ . as well as the  $s_{\max}$ -core. In the deco90 dataset, the nine cortical regions that ignite at  $G$ .

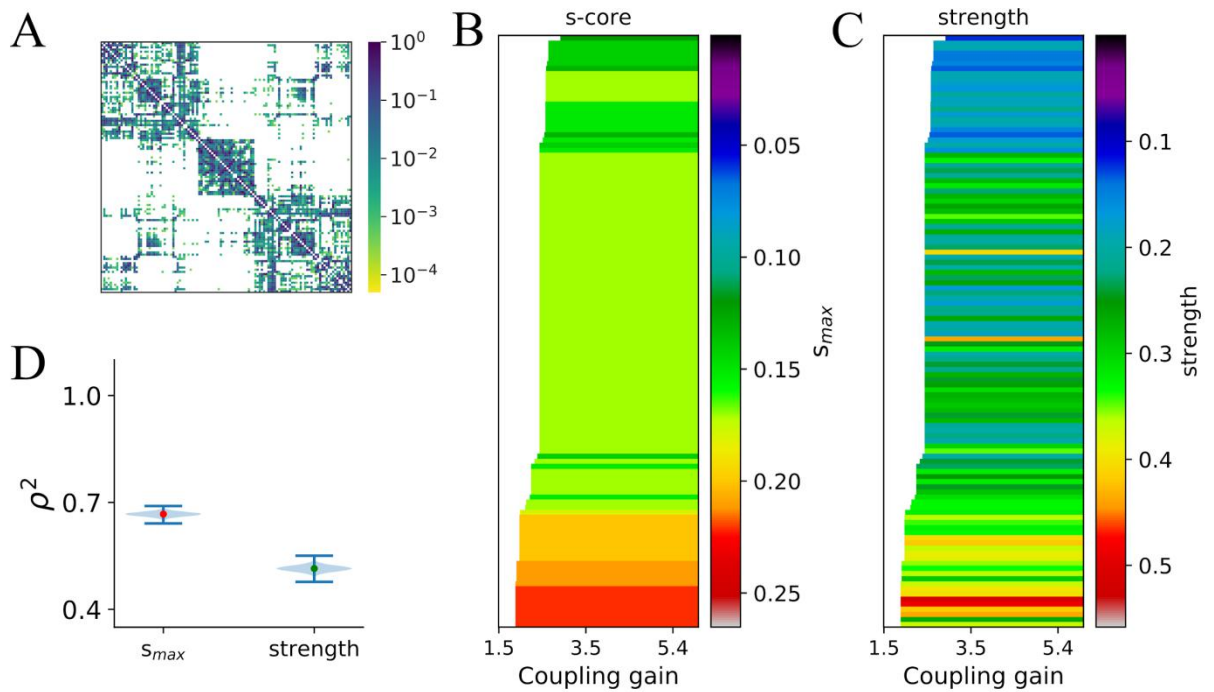


**Figure 41. The ignition,  $s$ -core, and, strength levels for each region in the Deco116 dataset.** (A) The Deco116 connectivity matrix was parcellated using the Automated Anatomical Labelling atlas (116 cortical + sub-cortical + cerebellum regions, and 4.056 connections). (B) The relationship between ignition and  $s_{max}$  of each region of the Deco116 connectome. Regions in the  $y$ -axis are sorted according to the coupling gain  $G$  ( $x$ -axis) value at which they first ignite. Colour code shows the  $s_{max}$  for each of the ignited regions. (C) Similarly, the relationship between ignition recruitment and the strength (color bar) of each region. (D) The explained variance of Spearman rank correlation ( $\rho^2$ ) between ignition recruitment and the  $s_{max}$  (**0.634**, percentile (2.5, 97.5) = (0.614, 0.654), *red dot*), and strength (**0.625**, percentile (2.5, 97.5) = (0.611, 0.638), *green dot*). The Deco116 connectome does not show a significant difference in the explained variance of the ignition recruitment between the strength and the  $s_{max}$ . The significance of  $\rho^2$  was evaluated using 10.000 replicas from bootstrap resampling (violin plots).

Figure 40D shows the Spearman rank correlation squared ( $\rho^2$ , explained variance) between ignition recruitment and either  $s_{max}$  (0.667) or strength (0.515). The  $\rho^2$  of ignition recruitment is statistically higher when the  $s_{max}$  is considered. Thus, the Deco90 dataset supports that the ignition recruitment is related to core organization, despite the differences in the neural elements and parcellation with the Hagmann connectome.

Next, the parcellation that considers cortical + subcortical + cerebellum regions was called the Deco116 dataset, which had 116 nodes and 4.056 connections (Figure 41A). The Deco116 dataset also has a higher network density (~30%) than the Hagmann one (~27%), and present the bistability range, in which the ignition point is  $G=1.875$ , and the flaring point is  $G_+ = 4.775$ .

Figure 41B shows the sorted coupling gain of the first ignition (*x-axis*) of each cortical area (*y-axis*). In color is shown the  $s_{\max}$  of each cortical area. Similarly, Figure 41C shows in color the strength of each cortical area. In the Deco116 dataset, the ignition starts in the  $s_{\max}$ -core nodes (8, 7%). However, one node that does not belong to the  $s_{\max}$ -core is ignited at  $G_-$ . The strength captures the ignited nodes at  $G_-$  worst than the  $s_{\max}$ -core.

Figure 41D shows the Spearman rank correlation squared ( $\rho^2$ , explained variance) between ignition recruitment and either  $s_{\max}$  (0.634) or strength (0.625). The  $\rho^2$  of ignition recruitment has not a significant difference between  $s_{\max}$  and strength. Thus, the Deco116 dataset supports that the ignition recruitment is related to the core organization of cortical, and not to the cerebellum regions.

Finally, Figure 42 resumes the Spearman rank correlation squared ( $\rho^2$ , explained variance) between ignition recruitment and either  $s_{\max}$  or strength of the human datasets. Figure 42A shows that the Hagman dataset is similar to the obtained with the other dataset, except for the Schirmer dataset. Figure 42B shows that the human connectomes that consider only cortical regions have a better fit between ignition recruitment and  $s_{\max}$ .

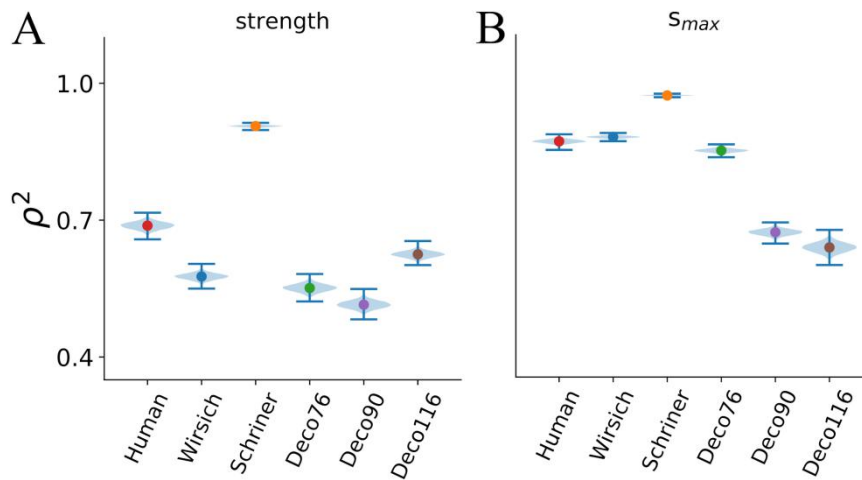


**Figure 42. The ignition recruitment comparative between  $s$ -core and strength of each node in all the human connectomes. (A)** The explained variance of Spearman rank correlation ( $\rho^2$ ) between ignition recruitment and the  $s_{max}$  of Human (**0.867**, percentile (2.5, 97.5) = (0.858, 0.874), *red dot*), Wirsich (*blue dot*), Schirner (*orange dot*), Deco76 (*green dot*), Deco90 (*purple dot*), and Deco116 (*brown dot*). **(B)** The  $\rho^2$  between ignition recruitment and the strength of Human (**0.687**, percentile (2.5, 97.5) = (0.672, 0.702)), Wirsich, Schirner, Deco76, Deco90, and Deco116. The significance of  $\rho^2$  was evaluated using 10.000 replicas from bootstrap resampling (violin plots).

## 2. The script of the dynamic simulation of the mean-field model

```

def run_sim32(pars, IC='handl', TofS='det', sd=1):
    """Input:
    -----
    pars : dict
        Parameters, see function default_pars()
    IC: str
        Initial conditions, 'rn': random, 'handl':high and low Initial
    Conditions, 'no_rn': initial conditions no random(0)
    TofS : str
        Tipe of Simulation, 'stc': stochastic, or
    'det':deterministic simulatio
    sd : int
        seed of random initial conditions
    Output:
    -----
    r(t) for vector t"""

    # Retrieve parameters
    C = pars['C']                #Network
    N = pars['N']                #Nodes
    w, G = pars['w'], pars['G']  #Local and Global
    connectivity parameters
    JN = pars['JN']              #Ex strenght
    tauS, gamma = pars['tauS'], pars['gamma'] #

    if TofS == 'stc':
        I0, tau0, sigma = pars['I0'], pars['tau0'], pars['sigma'] #
    elif TofS == 'det':
        I0 = pars['I0']
    if IC != 'rn':
        Sl, Sh = pars['Sl'], pars['Sh'] #
    range_t = pars['range_t']      #Range time vector points
    nt = range_t.size              #Total time
    dt = range_t[1] - range_t[0]  #delta time

    #Number of simulations
    nsim = G.shape[0]

    # Initialize
    S = np.zeros([nt, N, nsim],dtype=np.float32);
    #Initial State
    r = np.zeros([nt, N, nsim],dtype=np.float32);

    # Set random seed
    print( 'random number:' ,np.random.uniform(Sl, Sh))
    if IC == 'no_rn':
        S[0] = 0.0 * np.ones(size=(N,nsim))
    elif IC == 'handl':

```

```

        S[0] = np.random.uniform(Sl, Sh, (N, 1)) *
np.ones((1,nsim), dtype=np.float32) #Condiciones Iniciales
Semi-Aletoria
    elif IC == 'rn':
        S[0] = np.random.uniform(0, 1.0, (N, nsim) ) #Condiciones
Iniciales Semi-Aletorias
    elif IC == 'icvar':
        S[0] = ic_v

#Tipe of Simulation
if TofS == 'stc':
    Ieta = I0 + sigma*np.random.randn(N)
    noise = np.random.randn(N,nt) #White Noise
elif TofS == 'det':
    Ieta = I0 #White Noise

#Start to Running Simulation
t0 = time.time()
print( 'Running...')
for idx in range(1, nt):
    # Total synaptic input
    Isyn = w*JN*S[idx-1] + G*JN*(np.sum(C[:, :, None])*
S[idx-1][None, :, :], 1)) + Ieta
    r[idx-1] = F(Isyn)

#----- Dynamical equations
-----

    # Update Mean NMDA-mediated synaptic dynamics
    S[idx] = S[idx-1] + dt*(-S[idx-1]/tauS +
(1-S[idx-1])*gamma*r[idx-1])

    # Update Ornstein-Uhlenbeck process
    if TofS == 'stc':
        Ieta = Ieta + (dt/tau0)*(I0-Ieta) +
np.sqrt(dt/tau0)*sigma*noise[:,idx]
    elif TofS == 'det':
        Ieta = Ieta
r[-1] = r[-2]
print( 'done!, total time: ', time.time()-t0)
Results = {'r':r}
return Results

```





---

## Bibliography

---

1. Achard, S. *et al.* (2006) ‘A resilient, low-frequency, small-world human brain functional network with highly connected association cortical hubs’, *The Journal of neuroscience: the official journal of the Society for Neuroscience*, 26(1), pp. 63–72.
2. Alstott, J. *et al.* (2009) ‘Modeling the impact of lesions in the human brain’, *PLoS computational biology*, 5(6), p. e1000408.
3. Alstott, J. *et al.* (2014) ‘A unifying framework for measuring weighted rich clubs’, *Scientific reports*, 4, p. 7258.
4. Alvarez-hamelin, J. I., Luca Dall’Asta, Alain Barrat, and Alessandro Vespignani. 2006. “Large Scale Networks Fingerprinting and Visualization Using the K-Core Decomposition.” In *Advances in Neural Information Processing Systems 18*, edited by Y. Weiss, B. Schölkopf, and J. C. Platt, 41–50. MIT Press.
5. Aulet, L. S. *et al.* (2019) ‘Canine sense of quantity: evidence for numerical ratio-dependent activation in parietotemporal cortex’, *Biology letters*, 15(12), p. 20190666.
6. Baars, B. J. (30 de julio de 1993) *A Cognitive Theory of Consciousness*. Edición: New Ed. Cambridge University Press.
7. Bailey, A. Brock University, St. Catharines, Canada, Mario Ventresca University of Toronto, Toronto, Canada, and Beatrice Ombuki-Berman Brock University, St. Catharines, Canada. n.d. “Automatic Generation of Graph Models for Complex Networks by Genetic Programming | Proceedings of the 14th Annual Conference on Genetic and Evolutionary Computation.” Accessed February 14, 2020. <https://doi.org/10.1145/2330163.2330263>.
8. Bakker, R., Wachtler, T. and Diesmann, M. (2012) ‘CoCoMac 2.0 and the future of tract-tracing databases’, *Frontiers in neuroinformatics*, 6, p. 30.
9. Baria, A. T., Maniscalco, B. and He, B. J. (2017) ‘Initial-state-dependent, robust, transient neural dynamics encode conscious visual perception’, *PLoS computational biology*, 13(11), p. e1005806.
10. Barttfeld, P. *et al.* (2015) ‘Signature of consciousness in the dynamics of resting-state brain activity’, *Proceedings of the National Academy of Sciences of the United States of America*, 112(3), pp. 887–892.
11. Bassett, D. S. and Bullmore, E. T. (2017) ‘Small-World Brain Networks Revisited’, *The Neuroscientist: a review journal bringing neurobiology, neurology and psychiatry*, 23(5), pp. 499–516.
12. Battaglia, D. *et al.* (2012) ‘Dynamic effective connectivity of inter-areal brain circuits’, *PLoS computational biology*, 8(3), p. e1002438.
13. Battista, C. *et al.* (2018) ‘Mechanisms of interactive specialization and emergence of functional brain circuits supporting cognitive development in children’, *NPJ science of learning*, 3, p. 1.
14. Bayne, Tim, Jakob Hohwy, and Adrian M. Owen. 2016. “Are There Levels of Consciousness?” *Trends in Cognitive Sciences* 20 (6): 405–13.
15. Bedny, Marina, Alvaro Pascual-Leone, David Dodell-Feder, Evelina Fedorenko, and Rebecca Saxe. 2011. “Language Processing in the Occipital Cortex of Congenitally Blind Adults.” *Proceedings of the National Academy of Sciences of the United States of America* 108 (11): 4429–34.
16. Bergmann, Johanna, Erhan Genç, Axel Kohler, Wolf Singer, and Joel Pearson. 2016. “Neural Anatomy of Primary Visual Cortex Limits Visual Working Memory.” *Cerebral Cortex* 26 (1): 43–50.
17. Betzel, R. F. *et al.* (2019) ‘Distance-dependent consensus thresholds for generating

18. group-representative structural brain networks', *Network neuroscience (Cambridge, Mass.)*, 3(2), pp. 475–496.
19. Betzel, R. F., Medaglia, J. D. and Bassett, D. S. (2018) 'Diversity of meso-scale architecture in human and non-human connectomes', *Nature communications*, 9(1), p. 346.
20. Bota, Mihail, Hong-Wei Dong, and Larry W. Swanson. 2005. "Brain Architecture Management System." *Neuroinformatics* 3 (1): 15–48.
21. Bota, M., Sporns, O. and Swanson, L. W. (2015) 'Architecture of the cerebral cortical association connectome underlying cognition', *Proceedings of the National Academy of Sciences of the United States of America*, 112(16), pp. E2093–101.
22. Breakspear, M. (2017) 'Dynamic models of large-scale brain activity', *Nature neuroscience*, 20(3), pp. 340–352.
23. Bressler, S. L. and Menon, V. (2010) 'Large-scale brain networks in cognition: emerging methods and principles', *Trends in cognitive sciences*, 14(6), pp. 277–290.
24. Brink, Ruud L. van den, Sander Nieuwenhuis, and Tobias H. Donner. 2018. "Amplification and Suppression of Distinct Brainwide Activity Patterns by Catecholamines." *The Journal of Neuroscience: The Official Journal of the Society for Neuroscience* 38 (34): 7476–91.
25. Buckner, R. L. *et al.* (2009) 'Cortical hubs revealed by intrinsic functional connectivity: mapping, assessment of stability, and relation to Alzheimer's disease', *The Journal of neuroscience: the official journal of the Society for Neuroscience*, 29(6), pp. 1860–1873.
26. Butcher, J. C. 2016. *Numerical Methods for Ordinary Differential Equations*. John Wiley & Sons.
27. Buzsáki, G. (2006) *Rhythms of the Brain*. New York: Oxford University Press.
28. Caballero Gaudes, C. *et al.* (2013) 'Paradigm free mapping with sparse regression automatically detects single-trial functional magnetic resonance imaging blood oxygenation level dependent responses', *Human brain mapping*, 34(3), pp. 501–518.
29. Cabral, J. *et al.* (2017) 'Cognitive performance in healthy older adults relates to spontaneous switching between states of functional connectivity during rest', *Scientific reports*, 7(1), p. 5135.
30. Calhoun, V. D. *et al.* (2014) 'The chronnectome: time-varying connectivity networks as the next frontier in fMRI data discovery', *Neuron*, 84(2), pp. 262–274.
31. Camino-Pontes, Borja, Ibai Diez, Antonio Jimenez-Marin, Javier Rasero, Asier Erramuzpe, Paolo Bonifazi, Sebastiano Stramaglia, Stephan Swinnen, and Jesus M. Cortes. 2018. "Interaction Information Along Lifespan of the Resting Brain Dynamics Reveals a Major Redundant Role of the Default Mode Network." *Entropy* 20 (10): 742.
32. Cavanna, Andrea E. 2007. "The Precuneus and Consciousness." *CNS Spectrums* 12 (7): 545–52.
33. Chiang, A.-S. *et al.* (2011) 'Three-dimensional reconstruction of brain-wide wiring networks in *Drosophila* at single-cell resolution', *Current biology: CB*, 21(1), pp. 1–11.
34. Churchland, Mark M., Byron M. Yu, John P. Cunningham, Leo P. Sugrue, Marlene R. Cohen, Greg S. Corrado, William T. Newsome, *et al.* 2010. "Stimulus Onset Quenches Neural Variability: A Widespread Cortical Phenomenon." *Nature Neuroscience* 13 (3): 369–78.
35. Cole, M. W. *et al.* (2014) 'Intrinsic and task-evoked network architectures of the human brain', *Neuron*, 83(1), pp. 238–251.
36. Cole, M. W., Pathak, S. and Schneider, W. (2010) 'Identifying the brain's most globally connected regions', *NeuroImage*, 49(4), pp. 3132–3148.
37. Connor, D., and M. Shanahan. 2007. "A Simulated Global Neuronal Workspace with Stochastic Wiring." *AAAI Fall Symposium - Technical Report FS-07-01*: 43–48.
38. Coppen, Emma M., Jeroen van der Grond, Anne Hafkemeijer, Jurriaan J. H. Barkey Wolf, and Raymund A. C. Roos. 2018. "Structural and Functional Changes of the Visual Cortex in Early Huntington's Disease." *Human Brain Mapping* 39 (12): 4776–86.
39. Cossart, R., Aronov, D. and Yuste, R. (2003) 'Attractor dynamics of network UP states in the

- neocortex', *Nature*, 423(6937), pp. 283–288.
40. Coullon, Gaëlle S. L., Uzay E. Emir, Ione Fine, Kate E. Watkins, and Holly Bridge. 2015. "Neurochemical Changes in the Pericalcarine Cortex in Congenital Blindness Attributable to Bilateral Anophthalmia." *Journal of Neurophysiology* 114 (3): 1725–33.
  41. Deco, G. *et al.* (2013) 'Resting-state functional connectivity emerges from structurally and dynamically shaped slow linear fluctuations', *The Journal of neuroscience: the official journal of the Society for Neuroscience*, 33(27), pp. 11239–11252.
  42. Deco, G. *et al.* (2015) 'Rethinking segregation and integration: contributions of whole-brain modelling', *Nature reviews. Neuroscience*, 16(7), pp. 430–439.
  43. Deco, G. *et al.* (2017) 'Novel Intrinsic Ignition Method Measuring Local-Global Integration Characterizes Wakefulness and Deep Sleep', *eNeuro*, 4(5). doi: 10.1523/ENEURO.0106-17.2017.
  44. Deco, Gustavo, Morten L. Kringelbach, Viktor K. Jirsa, and Petra Ritter. 2017. "The Dynamics of Resting Fluctuations in the Brain: Metastability and Its Dynamical Cortical Core." *Scientific Reports* 7 (1): 3095.
  45. Deco, G. *et al.* (2018) 'Whole-Brain Multimodal Neuroimaging Model Using Serotonin Receptor Maps Explains Non-linear Functional Effects of LSD', *Current biology: CB*, 28(19), pp. 3065–3074.e6.
  46. Deco, G., Cruzat, J. and Kringelbach, M. L. (2019) 'Brain songs framework used for discovering the relevant timescale of the human brain', *Nature communications*, 10(1), p. 583.
  47. Deco, G. and Jirsa, V. K. (2012) 'Ongoing cortical activity at rest: criticality, multistability, and ghost attractors', *The Journal of neuroscience: the official journal of the Society for Neuroscience*, 32(10), pp. 3366–3375.
  48. Deco, G., Jirsa, V. K. and McIntosh, A. R. (2013) 'Resting brains never rest: computational insights into potential cognitive architectures', *Trends in neurosciences*, 36(5), pp. 268–274.
  49. Deco, G. and Kringelbach, M. L. (2017) 'Hierarchy of Information Processing in the Brain: A Novel "Intrinsic Ignition" Framework', *Neuron*, 94(5), pp. 961–968.
  50. Dehaene, S., Sergent, C. and Changeux, J.-P. (2003) 'A neuronal network model linking subjective reports and objective physiological data during conscious perception', *Proceedings of the National Academy of Sciences of the United States of America*, 100(14), pp. 8520–8525.
  51. Dehaene, Stanislas, and Jean-Pierre Changeux. 2011. "Experimental and Theoretical Approaches to Conscious Processing." *Neuron* 70 (2): 200–227.
  52. Del Cul, A., Baillet, S. and Dehaene, S. (2007) 'Brain dynamics underlying the nonlinear threshold for access to consciousness', *PLoS biology*, 5(10), p. e260.
  53. Desikan, R. S. *et al.* (2006) 'An automated labeling system for subdividing the human cerebral cortex on MRI scans into gyral based regions of interest', *NeuroImage*, 31(3), pp. 968–980.
  54. Destexhe, A. (2007) 'High-conductance state', *Scholarpedia journal*, 2(11), p. 1341.
  55. Dickstein, Steven G., Katie Bannon, F. Xavier Castellanos, and Michael P. Milham. 2006. "The Neural Correlates of Attention Deficit Hyperactivity Disorder: An ALE Meta-Analysis." *Journal of Child Psychology and Psychiatry, and Allied Disciplines* 47 (10): 1051–62.
  56. Finn, E. S. *et al.* (2019) 'Layer-dependent activity in human prefrontal cortex during working memory', *Nature neuroscience*, 22(10), pp. 1687–1695.
  57. Fischl, B. *et al.* (2004) 'Automatically parcellating the human cerebral cortex', *Cerebral cortex*, 14(1), pp. 11–22.
  58. Fornito, A., Zalesky, A. and Bullmore, E. T. (2016) *Fundamentals of Brain Network Analysis*. Academic Press.
  59. Fox, M. D. and Raichle, M. E. (2007) 'Spontaneous fluctuations in brain activity observed with functional magnetic resonance imaging', *Nature reviews. Neuroscience*, 8(9), pp. 700–711.
  60. Freyer, F. *et al.* (2012) 'A canonical model of multistability and scale-invariance in biological

- systems', *PLoS computational biology*, 8(8), p. e1002634.
61. Gămănuț, Răzvan, Henry Kennedy, Zoltán Toroczkai, Mária Ercsey-Ravasz, David C. Van Essen, Kenneth Knoblauch, and Andreas Burkhalter. 2018. "The Mouse Cortical Connectome, Characterized by an Ultra-Dense Cortical Graph, Maintains Specificity by Distinct Connectivity Profiles." *Neuron* 97 (3): 698–715.e10.
  62. Ghahremani, Maryam, R. Matthew Hutchison, Ravi S. Menon, and Stefan Everling. 2017. "Frontoparietal Functional Connectivity in the Common Marmoset." *Cerebral Cortex* 27 (8): 3890–3905.
  63. Glomb, K. *et al.* (2017) 'Resting state networks in empirical and simulated dynamic functional connectivity', *NeuroImage*, 159, pp. 388–402.
  64. Golan, T. *et al.* (2016) 'Human intracranial recordings link suppressed transients rather than "filling-in" to perceptual continuity across blinks', *eLife*, 5. doi: 10.7554/eLife.17243.
  65. Gollo, L. L. *et al.* (2015) 'Dwelling quietly in the rich club: brain network determinants of slow cortical fluctuations', *Philosophical transactions of the Royal Society of London. Series B, Biological sciences*, 370(1668). doi: 10.1098/rstb.2014.0165.
  66. Hagmann, Patric, Maciej Kurant, Xavier Gigandet, Patrick Thiran, Van J. Wedeen, Reto Meuli, and Jean-Philippe Thiran. 2007. "Mapping Human Whole-Brain Structural Networks with Diffusion MRI." *PloS One* 2 (7): e597.
  67. Hagmann, Patric, Leila Cammoun, Xavier Gigandet, Reto Meuli, Christopher J. Honey, Van J. Wedeen, and Olaf Sporns. 2008. "Mapping the Structural Core of Human Cerebral Cortex." *PLoS Biology* 6 (7): e159.
  68. Ham, Michael I., Luis M. Bettencourt, Floyd D. McDaniel, and Guenter W. Gross. 2008. "Spontaneous Coordinated Activity in Cultured Networks: Analysis of Multiple Ignition Sites, Primary Circuits, and Burst Phase Delay Distributions." *Journal of Computational Neuroscience* 24 (3): 346–57.
  69. Hansen, E. C. A. *et al.* (2015) 'Functional connectivity dynamics: modeling the switching behavior of the resting state', *NeuroImage*, 105, pp. 525–535.
  70. Harriger, L., van den Heuvel, M. P. and Sporns, O. (2012) 'Rich club organization of macaque cerebral cortex and its role in network communication', *PloS one*, 7(9), p. e46497.
  71. He, B. J. *et al.* (2008) 'Electrophysiological correlates of the brain's intrinsic large-scale functional architecture', *Proceedings of the National Academy of Sciences of the United States of America*, 105(41), pp. 16039–16044.
  72. Heuvel, Martijn P. van den, Edward T. Bullmore, and Olaf Sporns. 2016. "Comparative Connectomics." *Trends in Cognitive Sciences* 20 (5): 345–61.
  73. Hilgetag, C. C. and Kaiser, M. (2004) 'Clustered organization of cortical connectivity', *Neuroinformatics*, 2(3), pp. 353–360.
  74. Hlinka, Jaroslav, Milan Palus, Martin Vejmelka, Dante Mantini, and Maurizio Corbetta. 2011. "Functional Connectivity in Resting-State fMRI: Is Linear Correlation Sufficient?" *NeuroImage* 54 (3): 2218–25.
  75. Holcman, D. and Tsodyks, M. (2006) 'The emergence of Up and Down states in cortical networks', *PLoS computational biology*, 2(3), p. e23.
  76. Honey, C. J. *et al.* (2007) 'Network structure of cerebral cortex shapes functional connectivity on multiple time scales', *Proceedings of the National Academy of Sciences of the United States of America*. National Academy of Sciences, 104(24), pp. 10240–10245.
  77. Honey, C. J. *et al.* (2009) 'Predicting human resting-state functional connectivity from structural connectivity', *Proceedings of the National Academy of Sciences of the United States of America*, 106(6), pp. 2035–2040.
  78. Huk, A. C. and Shadlen, M. N. (2005) 'Neural activity in macaque parietal cortex reflects temporal integration of visual motion signals during perceptual decision making', *The Journal of*

- neuroscience: the official journal of the Society for Neuroscience*, 25(45), pp. 10420–10436.
79. Humphries, Mark D., and Kevin Gurney. 2008. “Network ‘Small-World-Ness’: A Quantitative Method for Determining Canonical Network Equivalence.” *PloS One* 3 (4): e0002051.
  80. Humphries, M. D., K. Gurney, and T. J. Prescott. 2006. “The Brainstem Reticular Formation Is a Small-World, Not Scale-Free, Network.” *Proceedings. Biological Sciences / The Royal Society* 273 (1585): 503–11.
  81. Hutchison, R. M. *et al.* (2013) ‘Dynamic functional connectivity: promise, issues, and interpretations’, *NeuroImage*, 80, pp. 360–378.
  82. Hütt, M.-T., Kaiser, M. and Hilgetag, C. C. (2014) ‘Perspective: network-guided pattern formation of neural dynamics’, *Philosophical transactions of the Royal Society of London. Series B, Biological sciences*, 369(1653). doi: 10.1098/rstb.2013.0522.
  83. Joglekar, M. R. *et al.* (2018) ‘Inter-areal Balanced Amplification Enhances Signal Propagation in a Large-Scale Circuit Model of the Primate Cortex’, *Neuron*, 98(1), pp. 222–234.e8.
  84. Kaiser, Marcus, and Claus C. Hilgetag. 2006. “Nonoptimal Component Placement, but Short Processing Paths, due to Long-Distance Projections in Neural Systems.” *PLoS Computational Biology* 2 (7): e95.
  85. Karahanoğlu, F. I. *et al.* (2013) ‘Total activation: fMRI deconvolution through spatio-temporal regularization’, *NeuroImage*, 73, pp. 121–134.
  86. Kenet, T. *et al.* (2003) ‘Spontaneously emerging cortical representations of visual attributes’, *Nature*, 425(6961), pp. 954–956.
  87. Kenny, Eva R., John T. O’Brien, David A. Cousins, Jonathan Richardson, Alan J. Thomas, Michael J. Firbank, and Andrew M. Blamire. 2010. “Functional Connectivity in Late-Life Depression Using Resting-State Functional Magnetic Resonance Imaging.” *The American Journal of Geriatric Psychiatry: Official Journal of the American Association for Geriatric Psychiatry* 18 (7): 643–51.
  88. Khundrakpam, Budhachandra S., Andrew Reid, Jens Brauer, Felix Carbonell, John Lewis, Stephanie Ameis, Sherif Karama, *et al.* 2013. “Developmental Changes in Organization of Structural Brain Networks.” *Cerebral Cortex* 23 (9): 2072–85.
  89. Kieliba, P. *et al.* (2019) ‘Large-scale intrinsic connectivity is consistent across varying task demands’, *PloS one*, 14(4), p. e0213861.
  90. Kirst, C., Timme, M. and Battaglia, D. (2016) ‘Dynamic information routing in complex networks’, *Nature communications*, 7, p. 11061.
  91. Kitsak, M. *et al.* (2010) ‘Identification of influential spreaders in complex networks’, *Nature physics*, 6(11), pp. 888–893.
  92. Kopell, N. J. *et al.* (2014) ‘Beyond the connectome: the dynome’, *Neuron*, 83(6), pp. 1319–1328.
  93. Kozlovskiy, Stanislav A., Sophie D. Shirenova, Anastasia K. Neklyudova, and Alexander V. Vartanov. 2017. “Brain Mechanisms of the Tip-of-the-Tongue State: An Electroencephalography-Based Source Localization Study.” *Psychology in Russia: State of the Art* 10 (3): 218–30.
  94. Lampl, I., Reichova, I. and Ferster, D. (1999) ‘Synchronous membrane potential fluctuations in neurons of the cat visual cortex’, *Neuron*, 22(2), pp. 361–374.
  95. Li, Mike, Yinuo Han, Matthew J. Aburn, Michael Breakspear, Russell A. Poldrack, James M. Shine, and Joseph T. Lizier. 2019. “Transitions in Information Processing Dynamics at the Whole-Brain Network Level Are Driven by Alterations in Neural Gain.” *PLoS Computational Biology* 15 (10): e1006957.
  96. Lombardo, Diego, Catherine Cassé-Perrot, Jean-Philippe Ranjeva, Arnaud Le Troter, Maxime Guye, Jonathan Wirsich, Pierre Payoux, *et al.* 2020. “Modular Slowing of Resting-State Dynamic Functional Connectivity as a Marker of Cognitive Dysfunction Induced by Sleep

- Deprivation.” *bioRxiv*. <https://doi.org/10.1101/2020.01.17.910810>.
97. Lynall, M.-E. *et al.* (2010) ‘Functional connectivity and brain networks in schizophrenia’, *The Journal of neuroscience: the official journal of the Society for Neuroscience*, 30(28), pp. 9477–9487.
  98. Lynn, C. W. and Bassett, D. S. (2019) ‘The physics of brain network structure, function and control’, *Nature Reviews Physics*, 1(5), pp. 318–332.
  99. Markov, Nikola T., Maria Ercsey-Ravasz, Camille Lamy, Ana Rita Ribeiro Gomes, Loïc Magrou, Pierre Misery, Pascale Giroud, *et al.* 2013. “The Role of Long-Range Connections on the Specificity of the Macaque Interareal Cortical Network.” *Proceedings of the National Academy of Sciences of the United States of America* 110 (13): 5187–92.
  100. Maslov, Sergei, and Kim Sneppen. 2002. “Specificity and Stability in Topology of Protein Networks.” *Science* 296 (5569): 910–13.
  101. Medel, Vicente, Joaquín Valdés, Samy Castro, Tomás Ossandón, and Gonzalo Boncompte. 2019. “Commentary: Amplification and Suppression of Distinct Brainwide Activity Patterns by Catecholamines.” *Frontiers in Behavioral Neuroscience*.
  102. Messé, A. *et al.* (2014) ‘Relating structure and function in the human brain: relative contributions of anatomy, stationary dynamics, and non-stationarities’, *PLoS computational biology*, 10(3), p. e1003530.
  103. Messé, A. *et al.* (2015) ‘A closer look at the apparent correlation of structural and functional connectivity in excitable neural networks’, *Scientific reports*, 5, p. 7870.
  104. Mišić, B. *et al.* (2015) ‘Cooperative and Competitive Spreading Dynamics on the Human Connectome’, *Neuron*, 86(6), pp. 1518–1529.
  105. Moutard, C., Dehaene, S. and Malach, R. (2015) ‘Spontaneous Fluctuations and Non-linear Ignitions: Two Dynamic Faces of Cortical Recurrent Loops’, *Neuron*, 88(1), pp. 194–206.
  106. Navarro-Lobato, I. and Genzel, L. (2019) ‘The up and down of sleep: From molecules to electrophysiology’, *Neurobiology of learning and memory*, 160, pp. 3–10.
  107. Nir, Y. *et al.* (2006) ‘Widespread functional connectivity and fMRI fluctuations in human visual cortex in the absence of visual stimulation’, *NeuroImage*, 30(4), pp. 1313–1324.
  108. Nir, Y. *et al.* (2008) ‘Interhemispheric correlations of slow spontaneous neuronal fluctuations revealed in human sensory cortex’, *Nature neuroscience*, 11(9), pp. 1100–1108.
  109. Noy, N. *et al.* (2015) ‘Ignition’s glow: Ultra-fast spread of global cortical activity accompanying local “ignitions” in visual cortex during conscious visual perception’, *Consciousness and cognition*, 35, pp. 206–224.
  110. Oh, Seung Wook, Julie A. Harris, Lydia Ng, Brent Winslow, Nicholas Cain, Stefan Mihalas, Quanxin Wang, *et al.* 2014. “A Mesoscale Connectome of the Mouse Brain.” *Nature* 508 (7495): 207–14.
  111. Opsahl, Tore, Vittoria Colizza, Pietro Panzarasa, and José J. Ramasco. 2008. “Prominence and Control: The Weighted Rich-Club Effect.” *Physical Review Letters* 101 (16): 168702.
  112. Orio, P. *et al.* (2018) ‘Chaos versus noise as drivers of multistability in neural networks’, *Chaos*, 28(10), p. 106321.
  113. Palmqvist, Sebastian, Michael Schöll, Olof Strandberg, Niklas Mattsson, Erik Stomrud, Henrik Zetterberg, Kaj Blennow, Susan Landau, William Jagust, and Oskar Hansson. 2017. “Earliest Accumulation of  $\beta$ -Amyloid Occurs within the Default-Mode Network and Concurrently Affects Brain Connectivity.” *Nature Communications* 8 (1): 1214.
  114. Papegaaij, S. *et al.* (2017) ‘Neural correlates of motor-cognitive dual-tasking in young and old adults’, *PloS one*, 12(12), p. e0189025.
  115. Parker, Jason G., Eric J. Zalusky, and Cemil Kirbas. 2014. “Functional MRI Mapping of Visual Function and Selective Attention for Performance Assessment and Presurgical Planning Using Conjunctive Visual Search.” *Brain and Behavior* 4 (2): 227–37.

116. de Pasquale, F. *et al.* (2010) ‘Temporal dynamics of spontaneous MEG activity in brain networks’, *Proceedings of the National Academy of Sciences of the United States of America*, 107(13), pp. 6040–6045.
117. de Pasquale, F. *et al.* (2013) ‘The connectivity of functional cores reveals different degrees of segregation and integration in the brain at rest’, *NeuroImage*, 69, pp. 51–61.
118. de Pasquale, F. *et al.* (2018) ‘Cortical cores in network dynamics’, *NeuroImage*, 180(Pt B), pp. 370–382.
119. Petridou, N. *et al.* (2013) ‘Periods of rest in fMRI contain individual spontaneous events which are related to slowly fluctuating spontaneous activity’, *Human brain mapping*, 34(6), pp. 1319–1329.
120. Pinto, Lucas, Michael J. Goard, Daniel Estandian, Min Xu, Alex C. Kwan, Seung-Hee Lee, Thomas C. Harrison, Guoping Feng, and Yang Dan. 2013. “Fast Modulation of Visual Perception by Basal Forebrain Cholinergic Neurons.” *Nature Neuroscience* 16 (12): 1857–63.
121. Rock, K. *et al.* (2014) ‘Dynamics of infectious diseases’, *Reports on Progress in Physics*, 77(2), p. 026602.
122. Roitman, J. D. and Shadlen, M. N. (2002) ‘Response of neurons in the lateral intraparietal area during a combined visual discrimination reaction time task’, *The Journal of neuroscience: the official journal of the Society for Neuroscience*, 22(21), pp. 9475–9489.
123. Rolls, E. T., Joliot, M. and Tzourio-Mazoyer, N. (2015) ‘Implementation of a new parcellation of the orbitofrontal cortex in the automated anatomical labeling atlas’, *NeuroImage*, 122, pp. 1–5.
124. Rosas, Fernando, Pedro A. M. Mediano, Michael Gastpar, and Henrik J. Jensen. 2019. “Quantifying High-Order Interdependencies via Multivariate Extensions of the Mutual Information.” *arXiv [cs.IT]*. arXiv. <http://arxiv.org/abs/1902.11239>.
125. Rubinov, M. *et al.* (2015) ‘Wiring cost and topological participation of the mouse brain connectome’, *Proceedings of the National Academy of Sciences of the United States of America*, 112(32), pp. 10032–10037.
126. Rubinov, M. and Sporns, O. (2010) ‘Complex network measures of brain connectivity: uses and interpretations’, *NeuroImage*, 52(3), pp. 1059–1069.
127. Sabbah, Norman, Nicolae Sanda, Colas N. Authié, Saddek Mohand-Saïd, José-Alain Sahel, Christophe Habas, Amir Amedi, and Avinoam B. Safran. 2017. “Reorganization of Early Visual Cortex Functional Connectivity Following Selective Peripheral and Central Visual Loss.” *Scientific Reports* 7 (February): 43223.
128. Salehi, M. *et al.* (2020) ‘There is no single functional atlas even for a single individual: Functional parcel definitions change with task’, *NeuroImage*, 208, p. 116366.
129. Salvador, R. *et al.* (2005) ‘Neurophysiological architecture of functional magnetic resonance images of human brain’, *Cerebral cortex*, 15(9), pp. 1332–1342.
130. Schirner, M. *et al.* (2015) ‘An automated pipeline for constructing personalized virtual brains from multimodal neuroimaging data’, *NeuroImage*, 117, pp. 343–357.
131. Schurger, A. *et al.* (2015) ‘Cortical activity is more stable when sensory stimuli are consciously perceived’, *Proceedings of the National Academy of Sciences of the United States of America*, 112(16), pp. E2083–92.
132. Seguin, C., Razi, A. and Zalesky, A. (2019) ‘Inferring neural signalling directionality from undirected structural connectomes’, *Nature communications*, 10(1), p. 4289.
133. Seth, A. (2007) ‘Models of consciousness’, *Scholarpedia journal*, 2(1), p. 1328.
134. Shih, C.-T. *et al.* (2015) ‘Connectomics-based analysis of information flow in the Drosophila brain’, *Current biology: CB*, 25(10), pp. 1249–1258.
135. Shine, James M., Matthew J. Aburn, Michael Breakpear, and Russell A. Poldrack. 2018. “The Modulation of Neural Gain Facilitates a Transition between Functional Segregation and

- Integration in the Brain.” *eLife* 7 (January). <https://doi.org/10.7554/eLife.31130>.
136. Shine, James M., Michael Breakspear, Peter T. Bell, Kaylena A. Ehgoetz Martens, Richard Shine, Oluwasanmi Koyejo, Olaf Sporns, and Russell A. Poldrack. 2019. “Human Cognition Involves the Dynamic Integration of Neural Activity and Neuromodulatory Systems.” *Nature Neuroscience* 22 (2): 289–96.
  137. Smit, D. J. A. *et al.* (2008) ‘Heritability of “small-world” networks in the brain: a graph theoretical analysis of resting-state EEG functional connectivity’, *Human brain mapping*, 29(12), pp. 1368–1378.
  138. Spiegler, Andreas, Thomas R. Knösche, Karin Schwab, Jens Haueisen, and Fatihcan M. Atay. 2011. “Modeling Brain Resonance Phenomena Using a Neural Mass Model.” *PLoS Computational Biology* 7 (12): e1002298.
  139. Sporns, O. (2016) *Networks of the Brain*. MIT Press.
  140. Sporns, O., Tononi, G. and Kötter, R. (2005) ‘The human connectome: A structural description of the human brain’, *PLoS computational biology*, 1(4), p. e42.
  141. Stam, C. J. (2004) ‘Functional connectivity patterns of human magnetoencephalographic recordings: a “small-world” network?’, *Neuroscience letters*, 355(1-2), pp. 25–28.
  142. Stefanescu, Roxana A., and Viktor K. Jirsa. 2008. “A Low Dimensional Description of Globally Coupled Heterogeneous Neural Networks of Excitatory and Inhibitory Neurons.” *PLoS Computational Biology* 4 (11): e1000219.
  143. Swanson, L. W., Hahn, J. D. and Sporns, O. (2017) ‘Organizing principles for the cerebral cortex network of commissural and association connections’, *Proceedings of the National Academy of Sciences of the United States of America*, 114(45), pp. E9692–E9701.
  144. Tagliazucchi, E. *et al.* (2012) ‘Criticality in large-scale brain fMRI dynamics unveiled by a novel point process analysis’, *Frontiers in physiology*, 3, p. 15.
  145. Teeuw, Jalmar, Rachel M. Brouwer, João P. O. F. T. Guimarães, Philip Brandner, Marinka M. G. Koenis, Suzanne C. Swagerman, Maxime Verwoert, Dorret I. Boomsma, and Hilleke E. Hulshoff Pol. 2019. “Genetic and Environmental Influences on Functional Connectivity within and between Canonical Cortical Resting-State Networks throughout Adolescent Development in Boys and Girls.” *NeuroImage* 202 (November): 116073.
  146. Telesford, Qawi K., Karen E. Joyce, Satoru Hayasaka, Jonathan H. Burdette, and Paul J. Laurienti. 2011. “The Ubiquity of Small-World Networks.” *Brain Connectivity* 1 (5): 367–75.
  147. Theodoni, P. *et al.* (2020) ‘Structural attributes and principles of the neocortical connectome in the marmoset monkey’, *bioRxiv*. doi: 10.1101/2020.02.28.969824.
  148. Tomasi, D. and Volkow, N. D. (2010) ‘Functional connectivity density mapping’, *Proceedings of the National Academy of Sciences of the United States of America*, 107(21), pp. 9885–9890.
  149. Tomasi, D. and Volkow, N. D. (2011) ‘Functional connectivity hubs in the human brain’, *NeuroImage*, 57(3), pp. 908–917.
  150. Tzourio-Mazoyer, N. *et al.* (2002) ‘Automated anatomical labeling of activations in SPM using a macroscopic anatomical parcellation of the MNI MRI single-subject brain’, *NeuroImage*, 15(1), pp. 273–289.
  151. Utevsky, Amanda V., David V. Smith, and Scott A. Huettel. 2014. “Precuneus Is a Functional Core of the Default-Mode Network.” *The Journal of Neuroscience: The Official Journal of the Society for Neuroscience* 34 (3): 932–40.
  152. Vaessen, M. J. *et al.* (2010) ‘The effect and reproducibility of different clinical DTI gradient sets on small world brain connectivity measures’, *NeuroImage*, 51(3), pp. 1106–1116.
  153. Valencia, M. *et al.* (2008) ‘Dynamic small-world behavior in functional brain networks unveiled by an event-related networks approach’, *Physical review. E, Statistical, nonlinear, and soft matter physics*, 77(5 Pt 1), p. 050905.

154. Vanni, S., T. Tanskanen, M. Seppä, K. Uutela, and R. Hari. 2001. "Coinciding Early Activation of the Human Primary Visual Cortex and Anteromedial Cuneus." *Proceedings of the National Academy of Sciences of the United States of America* 98 (5): 2776–80.
155. Varela, F. *et al.* (2001) 'The brainweb: phase synchronization and large-scale integration', *Nature reviews. Neuroscience*, 2(4), pp. 229–239.
156. Vertes, R. P., W. B. Hoover, and J. J. Rodriguez. 2012. "Projections of the Central Medial Nucleus of the Thalamus in the Rat: Node in Cortical, Striatal and Limbic Forebrain Circuitry." *Neuroscience* 219 (September): 120–36.
157. van Vugt, B. *et al.* (2018) 'The threshold for conscious report: Signal loss and response bias in visual and frontal cortex', *Science*, 360(6388), pp. 537–542.
158. Wallace, R. (14 de abril de 2005) *Consciousness: A Mathematical Treatment of the Global Neuronal Workspace Model*. Edición: 2005. Springer.
159. Wang, X.-J. (2002) 'Probabilistic decision making by slow reverberation in cortical circuits', *Neuron*, 36(5), pp. 955–968.
160. Watts, D. J. and Strogatz, S. H. (1998) 'Collective dynamics of "small-world" networks', *Nature*, pp. 440–442. doi: 10.1038/30918.
161. Widjaja, E., M. Zamyadi, C. Raybaud, O. C. Snead, and M. L. Smith. 2013. "Abnormal Functional Network Connectivity among Resting-State Networks in Children with Frontal Lobe Epilepsy." *AJNR. American Journal of Neuroradiology* 34 (12): 2386–92.
162. Wilson, C. (2008) 'Up and down states', *Scholarpedia journal*, 3(6), p. 1410.
163. Windey, Bert, and Axel Cleeremans. 2015. "Consciousness as a Graded and an All-or-None Phenomenon: A Conceptual Analysis." *Consciousness and Cognition* 35 (September): 185–91.
164. Wirsich, J. *et al.* (2018) 'Brain Networks are Independently Modulated by Donepezil, Sleep, and Sleep Deprivation', *Brain topography*, 31(3), pp. 380–391.
165. Wong, K.-F. and Wang, X.-J. (2006) 'A recurrent network mechanism of time integration in perceptual decisions', *The Journal of neuroscience: the official journal of the Society for Neuroscience*, 26(4), pp. 1314–1328.
166. Xiao, Min, Haitao Ge, Budhachandra S. Khundrakpam, Junhai Xu, Gleb Bezgin, Yuan Leng, Lu Zhao, et al. 2016. "Attention Performance Measured by Attention Network Test Is Correlated with Global and Regional Efficiency of Structural Brain Networks." *Frontiers in Behavioral Neuroscience* 10 (October): 194.
167. Zhang, Sheng, Shang-Jui Tsai, Sien Hu, Jiansong Xu, Herta H. Chao, Vince D. Calhoun, and Chiang-Shan R. Li. 2015. "Independent Component Analysis of Functional Networks for Response Inhibition: Inter-Subject Variation in Stop Signal Reaction Time." *Human Brain Mapping* 36 (9): 3289–3302.
168. Zuo, X.-N. *et al.* (2012) 'Network centrality in the human functional connectome', *Cerebral cortex*, 22(8), pp. 1862–1875.